Università degli Studi di Cagliari

DOTTORATO DI RICERCA

PROGETTAZIONE MECCANICA

Ciclo **XXV**

TITOLO TESI

SIMULATION OF LOW-VELOCITY IMPACT DAMAGE IN SANDWICH COMPOSITES

Settore/i scientifico disciplinari di afferenza

ING-IND/14

Presentata da: **Dianshi Feng**

Coordinatore Dottorato: **Prof. Natalino Mandas**

Tutor/Relatore: **Prof. Francesco Aymerich**

Esame finale anno accademico 2012 – 2013

SIMULATION OF LOW-VELOCITY IMPACT DAMAGE IN SANDWICH COMPOSITES

Università di Cagliari

DIANSHI FENG

SUPERVISOR:
PROF. FRANCESCO AYMERICH

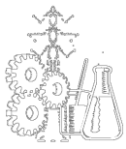

Universitá degli Studi di Cagliari
Dottorato di Ricerca in Progettazione Meccanica
XXV Ciclo

ABSTRACT

Composite materials have been increasingly used in many wind energy and transport applications due to their high strength, stiffness and excellent corrosion resistance. One of the main limitations of composites is their high susceptibility to impact-induced damage, which may result in significant strength reduction or even structural collapse. A detailed understanding of the extent and nature of impact damage is thus greatly needed for damage tolerance based structural design and a reliable estimation of the residual strength of a damaged structure.

In this thesis, fracture mechanics based progressive damage models, cohesive interface elements and crushable foam models were used to predict the structural response and internal failure mechanisms of sandwich composites subjected to low-velocity impact; various failure modes typically observed in composites including delaminations, fibre fracture and matrix cracking were simulated and implemented into ABAQUS/Explicit through user-defined subroutines VUMAT.

Numerical simulations were assessed and validated by a series of experimental analyses carried out through low-velocity impact tests (using drop-weight testing machine) and damage calibration tests (using X-radiography, Ultrasonics and optical microscopy of polished cross-sections). Good agreements were obtained between experiments and predictions not only in terms of structural responses as well as regarding the shape and size of internal damage under various investigated cases.

ACKNOWLEDGMENTS

The present work is the achievement of my research activities as a PhD student at University of Cagliari and an Early Stage Researcher under EU-Marie Curie Project-SYSWIND. This dissertation has been possible to be completed thanks to the support and help of many people I would like to acknowledge:

First and foremost, I wish to express my deeply gratitude to my supervisor, Prof. Francesco Aymerich, for his tutelage, advice and guidance with his depth of knowledge and enthusiasm all through my PhD thesis. His dedication and generosity with his time in helping me are greatly appreciated.

I would like to take a chance to thank my colleague, Dr. A. Cerioni, who has offered a lot of help over the years. Special thanks to Ing. Pier Francesco Orru', Daniela Zedda, Andrea Vincis and many other friends who have encouraged me throughout the research work and provided me the chance to enjoy numerous charming landscapes of Sardinia, a wonderful island offering me so many beautiful memories!

The financial support of SYSWIND is gratefully recognized.

Finally I wish to express particular gratitude to my family for their love and support in my life.

Cagliari, March 2014

Dianshi Feng

TABLE OF CONTENTS

LIST OF FIGURES

LIST OF TABLES

CHAPTER 1

INTRODUCTION

1.1 Motivation

Increasing energy demands and environmental concerns have led in recent years to a rapid expansion of the wind energy sector, with a corresponding steady increase not only in total installed power size and capacity of wind farms, but also in size of individual wind turbines (EWEA 2012) (IEA 2013).

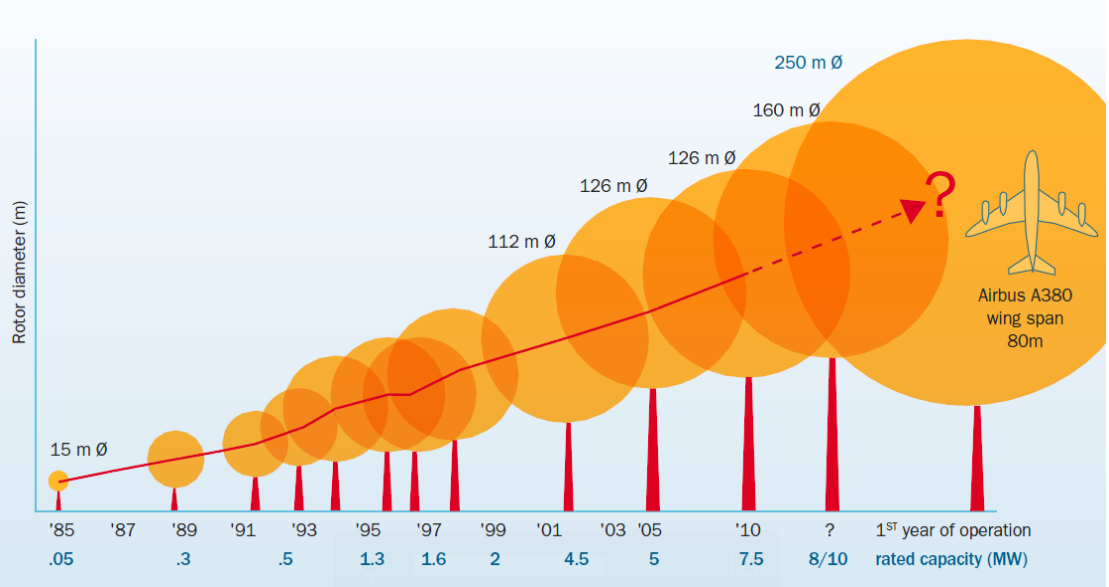

Figure 1-1: Diagram detailing the increase of turbine size since 1985. (UpWind 2011)

Driven by the desire to improve the cost effectiveness of electricity production, increasingly larger wind turbines have been developed in the last decades to enhance

energy capture and increase the energy output per unit of swept rotor area. Turbines with rotor diameters larger than 120 m and total height approaching 200 m are currently in service, and systems with power outputs of 10 MW and blade lengths close to 90 m are expected to be built and installed within the next few years (Thomsen 2009) (IEA 2013).

Large turbines typically require large and heavy rotor blades, which, as a consequence of the high gravity loads, inevitably induce severe stresses in the blade materials and transmit high loads to the rotor shaft as well as to the tower of the wind turbine. **Figure 1-2** illustrates the development of rotorblade weight as a function of rotorblade length. A key role in the design of wind turbine rotor blades is therefore played by the choice of appropriate materials, and advanced lightweight materials have been used to a growing extent in the construction of modern wind turbine blades.

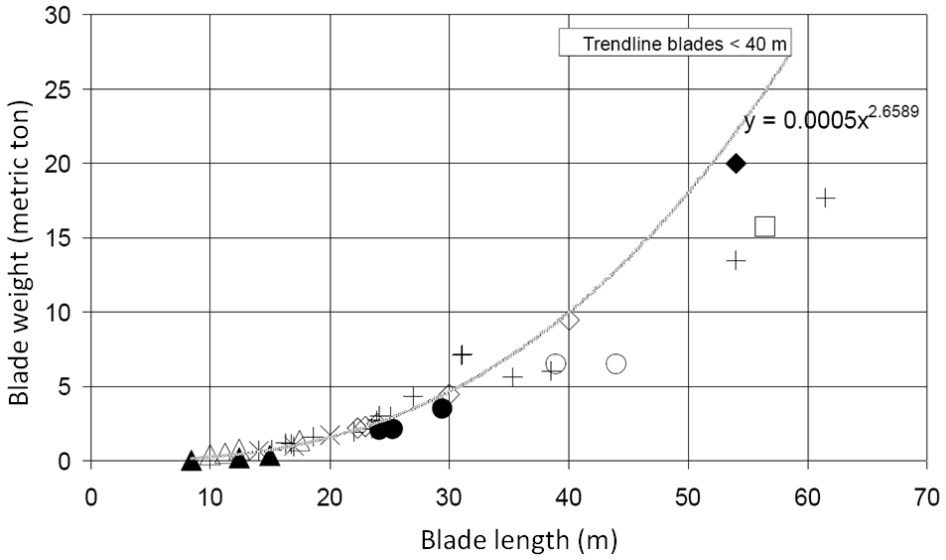

Figure 1-2: Development in rotorblade weight versus length. Symbols indicate different manufacturers and processing technologies. (Brøndsted, Lilholt and Lystrup 2005)

A number of primary requirements, which pose serious challenges to the optimization of materials and of structural configurations adopted in large turbine blades,

must be satisfied to ensure that the blades will meet the expected service life (Burton, et al. 2011) (Brøndsted, Lilholt and Lystrup 2005) (Thomsen 2009):

- low blade weight is required to reduce gravity loads;
- high material stiffness is required to avoid instability of structural components under compression loads and to prevent collision with the tower;
- high static strength is required to resist the extreme loads during the life of the structure;
- high fatigue strength is required to resist the time-varying loads and reduce material degradation;

Low weight, high stiffness and buckling properties (both at a local and at a global level), as well as good static and fatigue performances are thus the major design factors guiding the optimal selection of materials. The mechanical design of a rotorblade corresponds nominally to a beam, and the merit index is for this case (Ashby 1992):

$$M_b = E^{1/2}/\rho \qquad \textbf{Eq. 1-1}$$

where E is the material stiffness and ρ is the material density. **Figure 1-3** shows the diagram of stiffness versus density of commonly used materials. Lines of constant M_b are superimposed on the diagram, and materials that fulfill the relative stiffness criterion (partially or completely) are on the line and to the upper-left of the line.

In terms of materials strength, i.e., resistance against long-time fatigue loads, and extra high loads, it is also important to consider materials fracture toughness. The toughness in relation to density is collected in a similar diagram, which can be found in Reference (Ashby 1992). The combined materials performance criteria identify woods and composites as the best candidates for rotorblades.

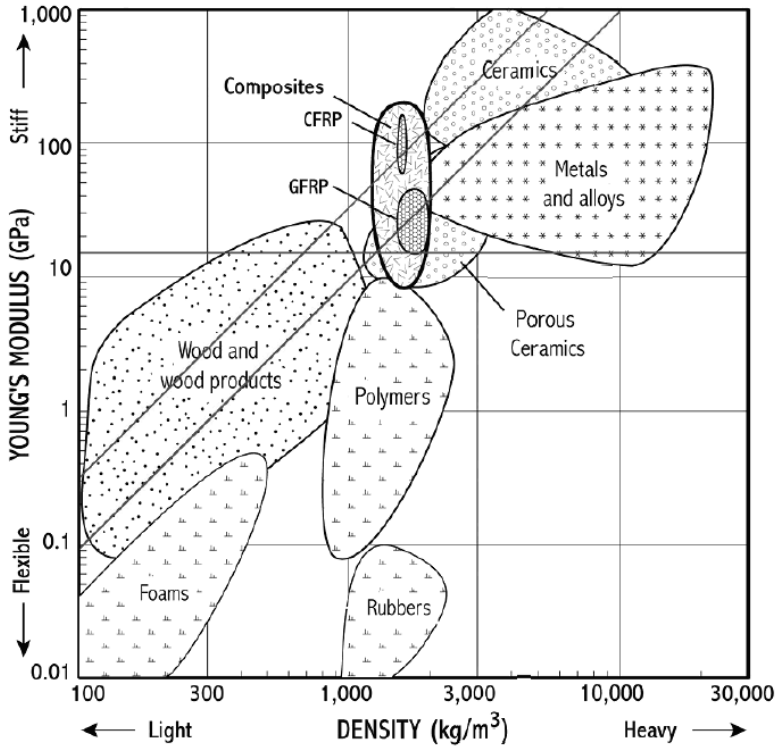

Figure 1-3: Diagram showing stiffness versus density for various materials. The merit index for a beam $M_b = E^{1/2}/\rho$ is represented by sloping lines with M_b equal to 0.003 (lower line) and 0.006 (upper line). The criterion for absolute stiffness E = 15 GPa is indicated by the horizontal line. (Lovatt and Shercliff 2002)

Woods are potentially interesting because of their low density, but their rather low stiffness makes it difficult to limit the (elastic) deflections for very large rotorblades; at the same time it's difficult to obtain woods in reproducible high quality, which is a requirement for stable and economical manufacturing of rotorblades and thus economically attractive wind energy. As a result, modern blades are typically made from composite materials, such as glass or carbon fibre reinforced polymers, used in a combination of monolithic (single skin laminates) and sandwich configurations (Brøndsted, Lilholt and Lystrup 2005) (Hayman, Wedel-Heinen and Brøndsted 2008) (Thomsen 2009).

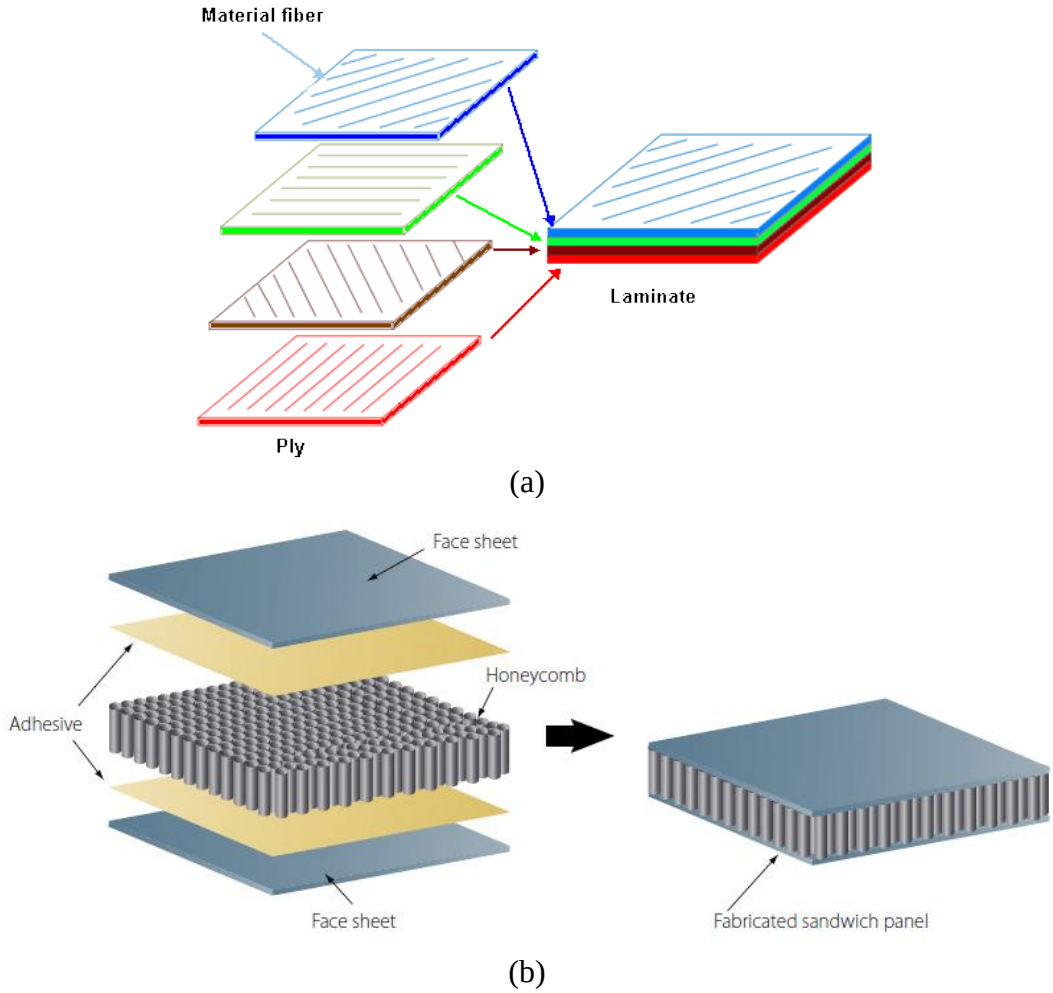

Figure 1-4: Diagram of laminate (a) and sandwich (b) configurations.

Composite sandwich structures consisting of two thin fibre-reinforced composite skins (also called facesheets or facings) separated by a thick core material of low density (typically a polymeric foam, balsa wood, or aluminium honeycomb) are widely used as lightweight structural components in wind turbine blades because of their high bending stiffness, superior buckling resistance and good static and fatigue strength properties (Thomsen 2009).

Composite sandwich construction is currently used in many portions of the blades, including the leading and trailing edges of the wing shells, the webs of the main spar or the internal stiffeners, to increase the compressive or shear buckling resistance of the structure (**Figure 1-5**). Most recently, with the development of large wind turbine blades, characterized by the presence of large unstiffened panels that are prone to failure in local buckling, sandwich configurations are being also considered, as an alternative to single skin designs, for potential use in other primary structural elements of the blade, such as the load carrying flange of the main spar or the spar-caps of the wing shells (Berggreen, et al. 2007) (Thomsen 2009).

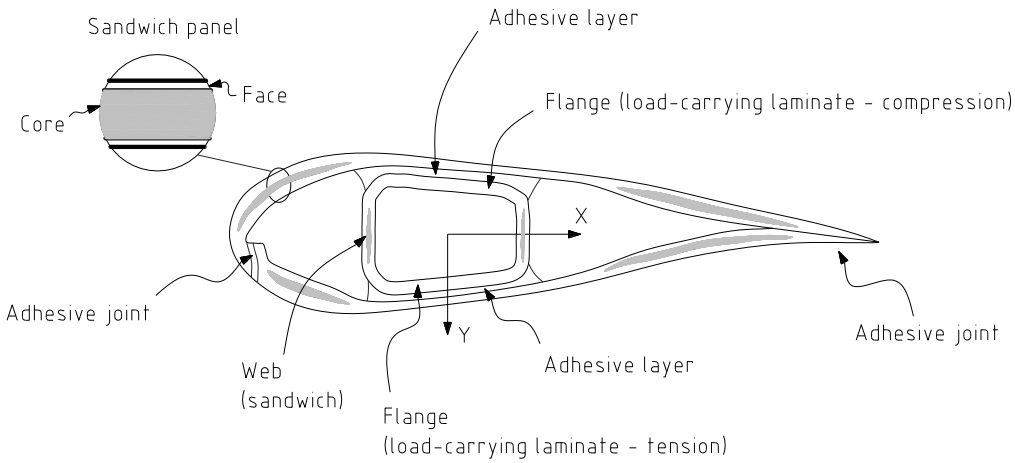

Figure 1-5: Design details of typical wind turbine blade. (Thomsen 2009)

One of the main limitations of sandwich composites is the high susceptibility to localized damage caused by foreign object impact events (Abrate 1997). Typical impact damage occurring in sandwich composites involves the superposition of different failure mechanisms, such as delaminations, matrix cracking, fibre fracture, face-core debonding and core crushing, which may be difficult – if not impossible- to detect by visual

inspection (this internal damage is known in aerospace applications as Barely Visible Impact Damage - BVID). Damage induced by impact, notably delaminations, may induce significant reductions in stiffness and strength of the composite blade and result in a local, or even global, collapse of the structure.

During their service life, wind turbine blades are subjected to loading conditions consisting of complex combinations of aerodynamic, gravitational and inertial loads, as well as of loads generated by the actions of the control systems (Burton, et al. 2011). Further load cases associated to operational conditions likely to occur during the entire lifespan of the blade must also be considered, including those experienced by the blade during the manufacturing, transportation, installation and maintenance phases (DNV. 2002). In particular, loads arising from impact with hail and foreign objects during operation, or from accidental impacts that inevitably occur during manufacturing, assembly, transport, assembly and construction, assume a special importance in view of the high vulnerability of composite materials to impact damage.

As an example, the Offshore Standard (DNV 2006) suggests as a guideline that "Accidental impact should lead to visible damage if it is critical for the strength of the blade. Otherwise the blade shall be designed for a maximum impact determined based on the packaging, transport and installation procedures". Furthermore, "it has to be shown that impact damage that can be realistically expected from manufacturing, transport, installation, and operation will not reduce the design resistance strength below the design load". Currently adopted design methodologies account for the presence of impact damage by the use of very conservative safety or knock-down factors (DNV. 2002) (DNV 2006); more advanced damage tolerance concepts (Hayman 2007) are however

being gradually introduced in the design process of critical elements of composite blades, so as to take full advantage of the weight-saving potentiality offered by sandwich materials. Design schemes based on a damage tolerance approach (Sierakowski 2000) (Zenkert, et al. 2005) accept the presence of pre-existing damage (such as that introduced during manufacturing or induced by accidental loads) and verify that the structure retain the required residual properties in the presence of the assumed damage. Reliable design procedures for composite blades should therefore include a reasonably accurate estimation of the internal damage locally induced by possible impacts, and make sure that the existing damage does not immediately lower the load carrying capability of the component below the design level, and will not grow to critical sizes under service loads, thus reducing the long term performance of the structure.

A detailed knowledge of the nature and extent of damage induced by impact events in composite sandwich elements is thus required for a safe estimation of residual strength and expected life of the damaged structure, and will play a critical role for the successful development and design of next generation wind turbine blades. A number of impact test procedures and destructive or non-destructive damage assessment techniques are available to characterize the impact damage resistance of laminated and sandwich composites; experimental testing is however extremely expensive and time-consuming, or even impracticable, at early stages of development, because of the wide range of possible structural configurations and loading conditions to be characterized. Accordingly, in order to reduce testing requirements and enable faster design procedures, there is a great need for numerical models and simulation tools capable of predicting the structural

and damage response of sandwich composites to impacts that can reasonably occur during the whole life of wind turbine blades.

It should be observed that damage developing in laminated and sandwich composites subjected to impact exhibits a very complicated pattern, involving the presence of a number of different interacting failure modes. The complexity of the damage mechanisms taking place in impacted composite structures necessitates the adoption of more sophisticated simulations than those used for conventional metallic materials, thus restricting the applicability of analytical models to basic structural configurations and simplified loading conditions.

In contrast, numerical finite element (FE) tools based on appropriate fracture models may provide an efficient alternative, at least at a preliminary or intermediate design phase, to costly experimental tests for prediction of the impact response of complex composite sandwich components and structures.

1.2 Objective

This research work is aimed at the development and application of a reliable finite element tool for damage prediction in composites for possible use in damage-tolerant optimized designs of composite sandwich configurations. The main objectives of this study include:

- To develop and implement fracture mechanics based models to simulate the damage and fracture mechanisms typically observed in impacted composite structures;
- To apply the developed models to investigate the performance of sandwich composites subjected to transverse low-velocity impacts;

- To assess the capability and reliability of the FE tool by comparing numerical predictions with the observations carried out during experimental tests.

1.3 Approach

The research activities were carried out in two parallel and collaborative approaches: experimental investigations and numerical analyses, as shown in **Figure 1-6**.

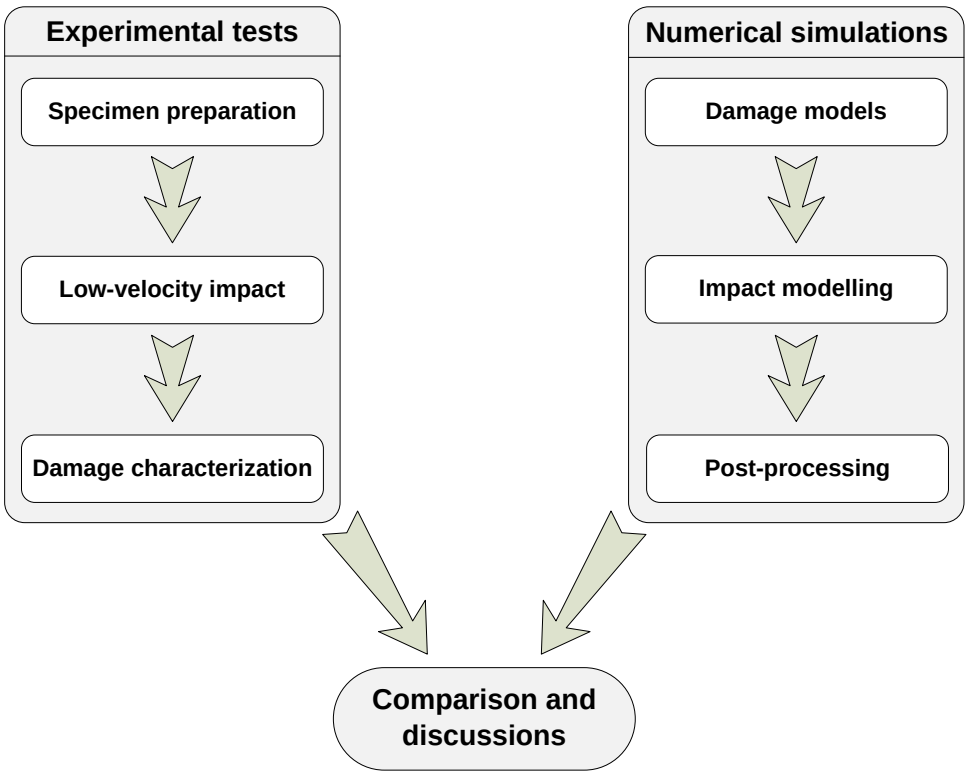

.

Figure 1-6: Diagram of research approach.

Experimental tests were conducted in the Composite Materials Lab at University of Cagliari. Sandwich panels with various configurations were prepared and impacted through a Drop-Weight Testing system; impact-induced damage was assessed by various characterization techniques including conventional and stereoscopic penetrant-enhanced X-Radiography, Ultrasonic C-Scans and Microscopic Observations of polished sections.

As to the numerical analyses, damage models based on Fracture Mechanics were developed to simulate the failure mechanisms typically occurring in impacted composite structures (delaminations between layers with different fibre orientations, fibre fracture, matrix cracking, face/core debonding and core crushing); the failure models were implemented in the FE package ABAQUS/Explicit via user material subroutines VUMAT and applied to investigate transverse low-velocity impacts on sandwich panels; all FE analyses were performed on a distributed-memory CLUSTER system of Linux Workstations using the MPI-based parallel solver available in ABAQUS/Explicit.

Numerical predictions were compared with experimental findings and the assessment on the developed numerical tool and further discussions were carried out.

1.4 Overview

Chapter 2 gives a brief introduction on impact damage in composites. Experimental techniques for conducting impact test and damage assessment are briefly presented. Experimental findings on impact-induced failures (from initiation of damage, final failure, to post-impact performance) and the importance of considering impact damage in structural design are summarized. Chapter 3 makes a quick literature review on modelling impact-induced damage in laminated and sandwich composites.

Chapter 4 presents the experimental tests that were carried out in this study to investigate impact-induced damage. The whole investigation process, including specimen preparation, drop-weight testing and damage characterization, as well as the various calibration tests on material properties is described.

Chapter 5 introduces in detail the numerical tool developed to simulate impact damage in composites. Derivation, implementation of failure models specific to each

failure mechanism, and preliminary tests conducted using a single-element model or simple FE models are also illustrated.

Chapter 6 shows the finite element models constructed in ABAQUS/Explicit for carrying out numerical analyses.

Chapter 7 and Chapter 8 illustrate and discuss the results through comparisons between numerical simulations and experimental results, based on 10 mm-thick PVC foam core sandwich panels with either cross-ply laminate skins (lamination sequence: $[0/90_3/0]$, in Chapter 7) or multidirectional laminate facesheets (lamination sequence: $[0_3/+45/-45]_S$, in Chapter 8).

Chapter 9 further assesses the predicting capability of the developed numerical tool through analyses of different configurations: impacts on sandwich panels with different core thickness, different panel size and boundary condition. Simulation of impacts on laminates and the importance of modelling in-ply damage modes for accurate simulation of impact events are finally discussed in Chapter 10.

In Chapter 11, a conclusion of the research work is made.

1.5 Sponsorship

This work has been supported by the EU funded FP7-ITN-Marie Curie project SYSWIND (Grant No. FP7-PEOPLE-ITN 238325).

CHAPTER 2

IMPACT DAMAGE IN COMPOSITES

2.1 Introduction

Composite structures are much more susceptible to impact damage than similar metallic structures. Impacts caused by foreign objects can be expected to occur during the whole life span of a structure including manufacturing, transportation, service, and maintenance operations (Abrate 1998). Such impact events can range from the most ordinary low-velocity impact of a tool dropped on a product to the hypervelocity impact of space debris on a spacecraft.

Unlike impact cases in metals where damage is easily detected as it starts at the impacted surface, impact-induced damage in composites often begins on the non-impacted surface or in the form of an internal delamination; the internal damage, even though usually undetected or underestimated by visual inspection, may however cause substantial losses in stiffness and residual strength of the composite structures.

In metal structures, due to the ductile nature of the material, large amounts of energy may be absorbed during impacts, so impact damage is generally not considered to be a threat. At yield stress the material may flow for very large strains (up to 20%) at constant stress before entering the hardening stage. In contrast, composite materials may fail in a wide variety of modes and contain barely visible impact damage (BVID) which

nevertheless severely reduces the structural integrity of the component. Most composites are brittle and so can only absorb energy in elastic deformation and through damage mechanisms, and not plastic deformation (Richardson and Wisheart 1996).

Obviously, most impacts on composite structures are in the transverse direction, but because of the lack of through-thickness reinforcement, transverse damage resistance is extremely poor. Interlaminar damage is often the first failure mode to take place due to the correspondingly low interlaminar strengths. As a result, very low design strains were generally adopted to guard against impact failure; that greatly limits the advantage of the excellent in-plane strength and stiffness properties provided by composite materials.

2.2 Low-velocity Impact

Extensive experimental and numerical studies show that impact velocity is an important factor in assessment of impact response. High-velocity impact usually brings about larger transverse deflection, more damage, and even perforation. Hence, the type of impact response is generally categorized into either low or high velocity (sometimes hyper velocity), but the transition between the two categories has been unclear for quite long time and various criteria were proposed by different researchers to distinguish a low-velocity impact from a high-velocity one.

Sjöblom et al. (Sjöblom, Hartness and Cordell 1988) and Shivakumar et al. (Shivakumar, Elber and Illg 1985) define low-velocity impacts as events which can be treated as quasi-static, the upper velocity limit of which can vary from one to tens of ms^{-1} depending on the target stiffness, material properties and the impactor's mass and stiffness. High-velocity impact response is dominated by stress wave propagation through

the material, in which the structure does not have time to respond, leading to highly localized damage. Boundary condition effects can be ignored because the impact event is over before the stress waves have reached the edge of the structure. In low-velocity impact, the dynamic structural response of the target is of utmost importance as the contact duration is long enough for the entire structure to respond to the impact and as a result more energy is absorbed elastically.

Cantwell and Morton (Cantwell and Morton 1991) conveniently classified low velocity as up to 10 ms^{-1}, by considering the test techniques which are generally employed in simulating the impact event (instrumented drop weight testing). While Abrate (Abrate 1991) in his review of impact on laminated composites stated that low-velocity impacts occurs for impact speeds of less than 100 ms^{-1}.

Liu and Malven (Liu and Malvern 1987) and Joshi and Sun (Joshi and Sun 1987) suggest that the type of impact can be classified based on induced damage, especially if damage is the prime concern. High velocity is thus characterized by delamination and matrix cracking.

Robinson and Davies (Robinson and Davies 1992) define a low-velocity impact as being one in which the through-thickness stress wave plays no significant part in the stress distribution and suggest a simple model to give the transition to high velocity. A cylindrical zone under the impactor is considered to undergo a uniform strain as the stress wave propagates through the plate, giving the compressive strain as:

$$\varepsilon_c = \frac{v_{impact}}{v_{sound\ in\ material}}$$

For failure strains between 0.5 and 1%, this gives the transition to stress wave dominated events at 10-20 ms^{-1} for epoxy composites.

In the book of Abrate (Abrate 1998), the expression “low-velocity impacts” refer to those where the ratio between impact velocity and the velocity of compressive waves propagating through the thickness is smaller than the maximum strain to failure in that direction.

Stronge (Stronge 2000) suggested that the amount of plastic deformation (or damage) nearing the impact zone governed the difference between low- and high-velocity impacts. Under low-velocity impact, the plastic deformation is localized around the contact area. In contrast, high-velocity impact leads to a larger area of deformation or damage around the area of contact. It should be noted that, for some cases, these two criteria gave the same impact response.

Literature reviews by Bland and Michelle (Bland and Michelle 2005) and by Chai and Zhu (Chai and Zhu 2011) show that impact mass should be taken into account jointly with the impact velocity. The impact response and damage may be quite different for impact of the same velocity and different impact masses (Abrate 1997) (Abrate 1998) (Zhou and Stronge 2006). Besides impact velocity and impact mass, impact duration is also a key parameter that distinguishes a low-velocity impact response from a high-velocity impact one (Richardson and Wisheart 1996) (Olsson 2000).

2.3 Experimental Technologies for Investigation of Impact Damage

2.3.1 Impact Test

To simulate actual impact by a foreign object, a number of test procedures have been suggested (Abrate 1998). Although many details of the specific experimental test apparatus may differ, two types of impact tests are basically used by most investigators to

replicate actual situations under controlled conditions. For example, during aircraft take-off and landing, debris flying from the runway can cause damage; this situation, with small high-velocity projectiles, is best simulated using a gas gun. Another concern is the impact of a composite structure by a larger projectile at low velocity, which occurs when tools are accidentally dropped on a structure. This situation is best simulated through striking a flat plate with a falling weight.

A significant progress was made on low-velocity impact tests throughout the 1980s and 1990s, and corresponding test equipment was developed (Adams and Adams 1989) (Abrate 1998). This typically consisted of an instrumented impact drop tower and associated data-reduction equipment, and today it remains as the impact test method of choice for composite materials (ASTM-D7136-07 2007). Typically, a plate on the order of 150 mm is simply supported around its four sides and then is impacted at its center. The impacting tup is typically hemispherical and is of the order of 15 mm in diameter. The delivered level of impact energy is selectable. Therefore, test technicians have the option to ensure full penetration, in which case the results of interest are the maximum force and the energy absorbed to maximum force, and total energy absorbed during the full penetration process. Alternatively, the test panel may be subjected to a prescribed level of impact energy, selected to induce local damage without penetration.

2.3.2 Damage Assessment

The damage induced by low energy impact events may often not be evident by visual inspection of a structure; surface damage may be barely visible. It is generally accepted that an accurate description of the impact-induced damage state, not only the

surface damage but also the position and spatial geometry of internal damage, is desired before a reliable assessment of residual mechanical properties can be conducted. The significant importance of accurate damage assessment in composites has lead to the development of experimental techniques that can be classified into destructive and non-destructive means (J. Kim 2000).

The destructive techniques include de-ply technique and cross-sectional fractography. The non-destructive methods involve visual inspection, X-radiography (de-ply radiography, stereo radiography, X-ray computed tomography and X-ray tomographic microscopy), as well as ultrasonic techniques (acoustic backscattering and volume visualization scanning acoustic microscopy).

- Visual inspection

Visual inspection is by far the most common nondestructive examination (NDE) technique (Allgaier and Ness 1993). It is possible to obtain useful information about the internal quality of quite thick optically transparent composite components by examining them visually against a brightly light background. The visual inspection is particularly useful for moving components made from composites and sandwich structures, such as helicopter rotor blades, turbine compressor buckets and water impellers. Careful visual inspection can also help identify the regions to be inspected by more sophisticated non-destructive methods.

It was shown that visual inspection of glass fibre-thermoset matrix composites could reveal internal defects and damage (Hirai, Hamada and Kim 1998). The reduction in transmission of light by delaminations can be accurately quantified using a solid state camera, whose image can be stored in a PC for the construction of digitised images.

■ X-radiography

X-radiography is one of the most useful forms of NDE because it can be used effectively on very complicated structures. X-ray techniques have long proved complementary to other techniques in finding volumetric defects in composite materials. The X-ray image is recorded as darker and lighter tones according to the intensity of the X-rays that pass through the different parts of material (**Figure 2-1**).

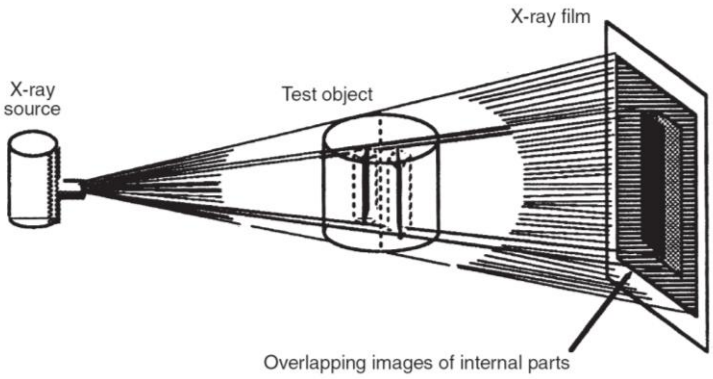

Figure 2-1: Schematic diagram of X-radiography. (J. Kim 2000)

However, internal damage, such as delaminations, in polymer matrix composite (PMC) laminates poses some difficulties in detection because delaminations tend to lie between plies and present a very small apparent thickness change. In addition, there is only little difference between absorption by the polymer matrix, fibres and air gaps. This requires a liquid having a high X-ray absorption coefficient, e.g. zinc iodide, to penetrate into the damaged area to be examined, most often by means of destructive procedures such as drilling a hole at the damage centre. The penetrant does not always reach small damage areas and delaminations, particularly those emanating from embedded and isolated internal structures.

Significant progress has been made in recent years in developing X-ray imaging techniques achieving state-of-the-art methods, such as computed tomography (CT) and its variations (J. Kim 2000).

- Ultrasonics

Ultrasonic measurements are most commonly used to detect damage in composite structures. The principle behind ultrasonic testing is that it sends an ultrasonic pulse into the material; if a defect is present below the surface, the echo of the pulse will be stronger and arrive earlier than if no defect was present. (**Figure 2-2**)

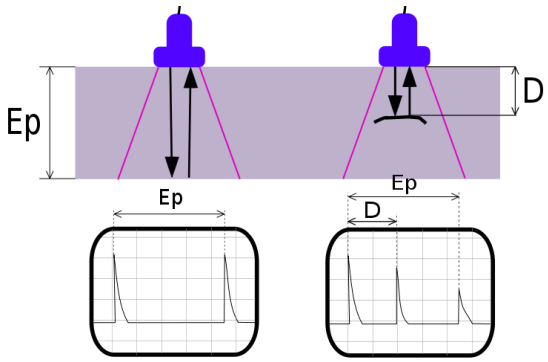

Figure 2-2: Principle of flaw detection with ultrasonics. (Romary 2006)

The ultrasonic map of defects can be presented in three different modes, namely A-scan, B-scan and C-scan. In the A-scan mode, the attenuated signals are displayed as a series of peaks against the time scale on an oscilloscope. The position of the signal's echo along the time axis allows the location of the defect in the thickness direction to be determined. In the B-scan mode, cross-sectional measurement can be made along any vertical plane, eliminating the need for destructive cross-sectioning of specimen. In the C-scan analysis, the transducer is moved in a plane parallel to the specimen surface in a rectilinear raster pattern to provide a planar view of the defect in a 'one shot' image.

- De-ply technique

In the de-ply technique, after being immersed in a solution of gold chloride, individual laminae are separated with a sharp blade, and are examined under an optical microscope. Due to its ease and simplicity of use, the de-ply technique has been widely employed to characterize impact damage in composites; furthermore, due to the high accuracy and reliability, the results of the de-ply technique can be used to calibrate the sensitivity of other nondestructive techniques. However, this technique is rather time-consuming and destructive; and it's not suitable for thermoplastic matrix composites due to the difficulties involved in partial pyrolysis of the matrix material.

2.4 Failure Mechanisms of Impact Damage

As revealed by experimental investigations, damage occurring in laminated composites subjected to impact consists of a combination of different intralaminar and interlaminar (delamination) damage modes, which combine to produce a quite complex three-dimensional damage pattern (Cantwell and Morton 1991) (Richardson and Wisheart 1996) (Abrate 1998) (Aymerich and Meili 2000).

Intralaminar damage modes include matrix cracking, where matrix damage occur parallel to the fibre direction, as a result of tensile, compressive and shear stresses, and fibre fracture, which involves collapse of reinforcing fibres by breakage in tension or by buckling in compression.

Interlaminar damage is the fracture of the thin resin rich interface between adjacent layers, which results in separation of the layers (delamination). Delaminations

are of particular concern in primary structures, since they may result in dramatic reductions of the compressive performance of the material.

The initiation and growth of impact damage are affected by many parameters. Material properties affect the overall stiffness of the structure and the contact stiffness and therefore will have a significant effect on the dynamic response of the structure. The thickness of the laminate, the density of the core, the size of the panel, and the boundary conditions are all factors that influence the impact dynamics, since they control the stiffness of the target. The characteristics of the projectile - including its density, elastic properties, shape, initial velocity, and incidence angle - are another set of parameters to be considered.

Experimental evidence (Richardson and Wisheart 1996) (Schoeppner and Abrate 2000) shows that no damage occurs in impacted laminates below an energy or load threshold; above this threshold, matrix cracks, in the form of shear cracking and tensile cracking (see **Figure 2-3**) generated by shear or normal stresses respectively, initiate and propagate in the vicinity of the impact region area, mainly in the intermediate and back face layers of the laminate. Matrix cracks are then followed by the onset of delaminations (Choi and Chang 1992), which initiate at the tips of pre-existing matrix cracks, as shown in **Figure 2-3**; delaminations always occur at the interfaces between plies with different fibre orientations and mainly extend along the fibre direction of the lowermost layer at that interface (see **Figure 2-4**). Impact delaminations grow to generate a characteristic three-dimensional spiral staircase (Srinivasan, et al. 1992) (Chester and Clark 1992) (Aymerich and Meili 2000) (Feng and Aymerich 2013), with the largest delaminations

usually occurring at the interfaces between layers with the highest orientation mismatch. As the impact energy is further increased, superficial fiber fractures (see **Figure 2-5**) initiate either at the tensile or at the compressive side of the impacted sample; when fibres fail the internal loads must redistribute to other areas of the structure, and may trigger other damage modes; finally, for very high impact energies, fibre fractures propagate through the remaining layers.

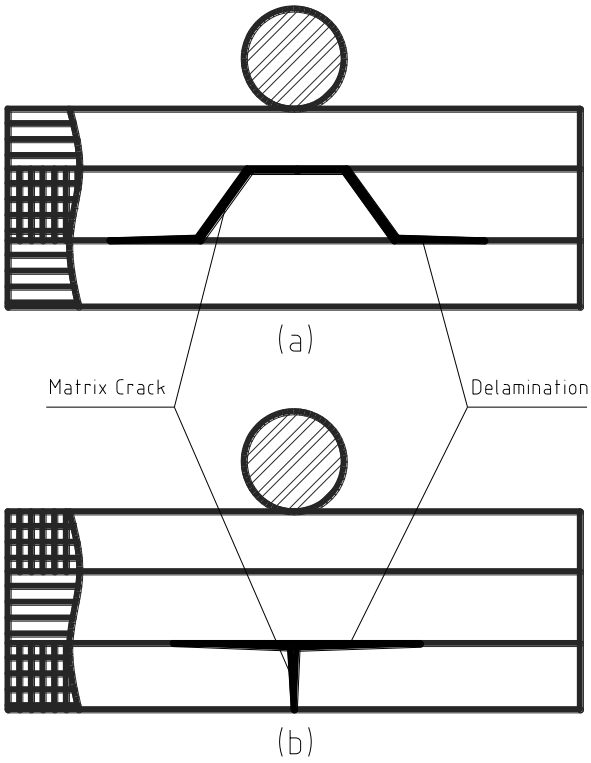

Figure 2-3: Impact damage mechanisms: (a) delamination induced by inner shear cracks, (b) delamination induced by surface bending crack. (Abrate 1998)

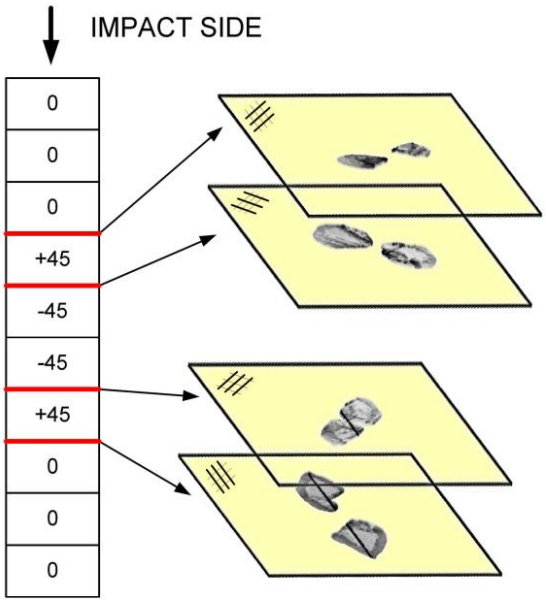

Figure 2-4: Consistency in orientation of delamination and fibre direction of lowermost layer at each interface. (Feng and Aymerich 2013)

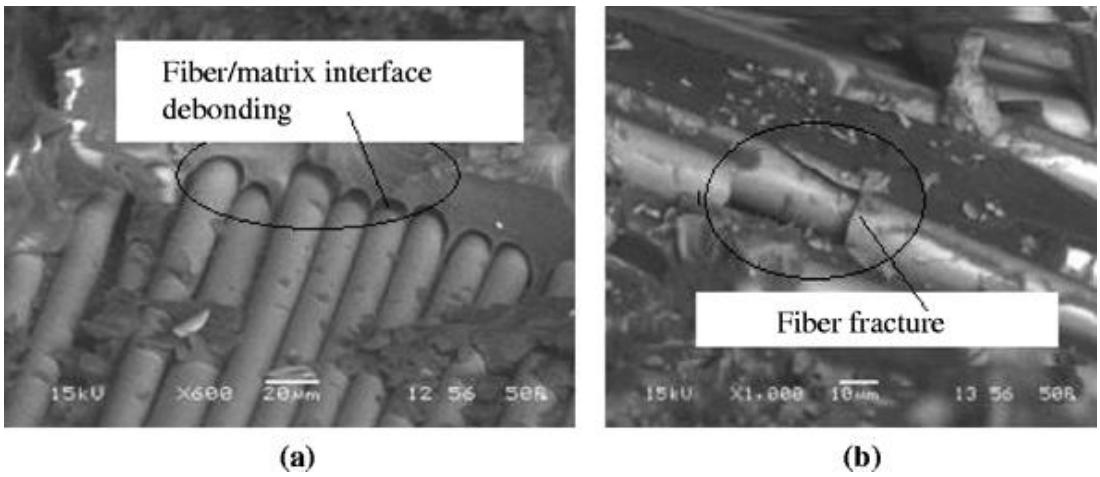

Figure 2-5: Illustration of fibre failure: (a) fibre/matrix debonding and (b) fibre breakage. (Sethi and Ray 2011)

The dominant damage modes likely to occur in impacted sandwich composites include damage in the laminated skins and in the core material, together debonding at the

interface between core and skin. Even though the type of damage occurring in the laminated skins is not dissimilar to that observed in impacted monolithic composites, the structural response and the damage resistance of sandwich structures are strongly dependent on the deformation of the core material and on the fracture characteristics of the skin/core interface (Abrate 1997). In particular, the response of the impacted skin is greatly affected by the mechanical behaviour of the core material (Daniel 2010), whose properties, which are often strongly nonlinear (as in the case of polymeric closed cell foams), must be characterized and modelled in detail in order to predict with reasonable accuracy the localized degradation induced by impact on the material. Under impact, the core-facing interface may debond in a region surrounding the point of impact, and the core experiences permanent deformations (Abrate 1998), as illustrated in **Figure 2-6**.

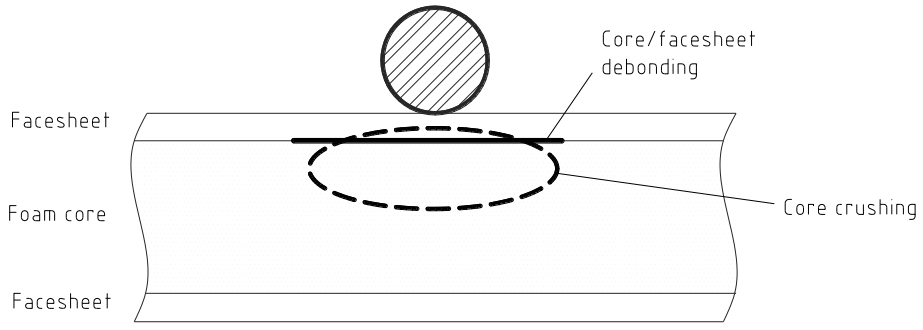

Figure 2-6: Diagram of core/facesheet debonding and core crushing.

2.5 Effect of Impact Damage on Residual Properties

In order to make sure that a damaged structure will not catastrophically collapse during service life and will retain sufficient structural efficiency, it is necessary to carry

out damage tolerance studies, assessing the residual mechanical properties of the structure after impact (MIL-HDBK-17-3E 1997).

"Damage tolerance" refers to a systems capability to perform after-impact. Even BVID can lead to strength reductions of up to 50% relative to an undamaged structure (Cvitkovich and Jackson 1999). Residual strengths in tension, compression, bending and fatigue will be reduced to varying degrees depending on the dominant failure mode.

2.5.1 Residual Tensile Strength

Residual tensile strength (Abrate 1991) normally follows a curve as shown in **Figure 2-7**. In region I, no damage occurs as the impact energy is below the threshold value for damage initiation. Once the threshold has been reached, the residual tensile strength reduces quickly to a minimum in region II as the extent of damage increases. Region III sees a constant value of residual strength because the impact velocity has reached a point where clean perforation occurs, leaving a net hole. As the fibres carry the majority of tensile load in the longitudinal direction, fibre damage is the critical damage mode.

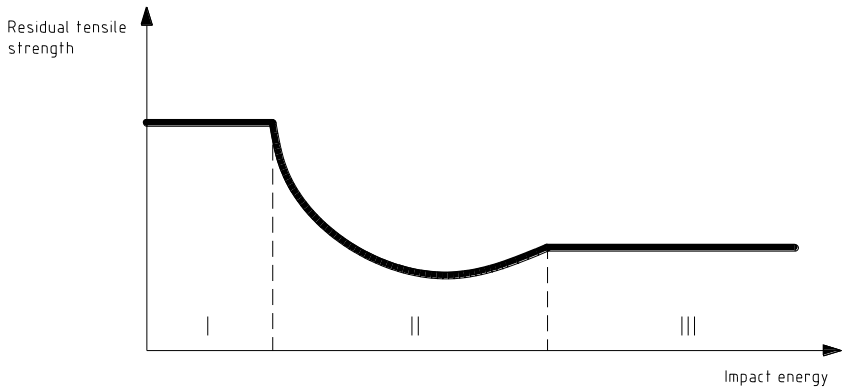

Figure 2-7: Residual tensile strength versus impact energy. (Abrate 1991)

2.5.2 Residual Compressive Strength

Poor post-impact compressive strength (PICS) is the greatest weakness of composite materials in terms of residual properties. This is mainly due to local instability resulting from delamination causing large reductions in compressive strength. As delamination can be produced by low-energy impacts, large strength reductions in compression can occur for BVID. Delamination divides the laminate into sub-laminates which have a lower bending stiffness than the original laminate and are less resistant to buckling loads. Under a compressive load, a delamination can cause buckling in one of three modes (Abrate 1998): global buckling, local buckling, or a combination of them, as illustrated in **Figure 2-8**. The mode of failure generally changes from global, to local, to mixed mode as the delamination length increases.

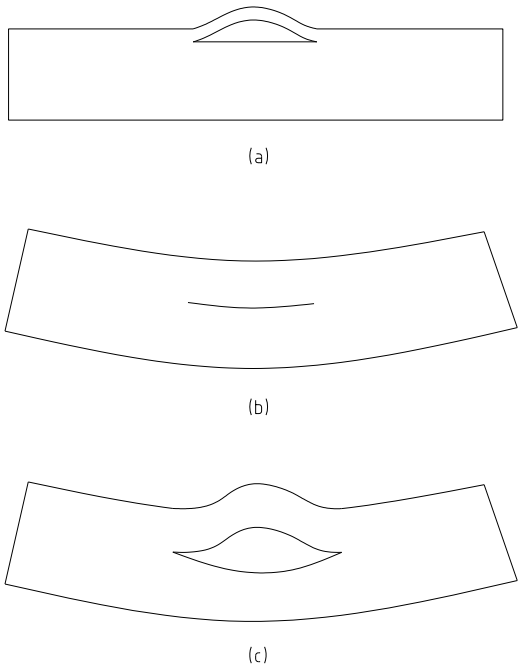

Figure 2-8: Local, global and local-global buckling modes. (Abrate 1998)

To determine compressive strength degradation of the impacted panel, a compression after impact (CAI) test is generally used. This is the basis of ASTM D7137 (ASTM-D7137-07 2007), which uses a 100 mm by 150 mm drop-weight impacted specimen subjected to a uniform in-plane compressive force along its 100 mm long edges. The specimen is simply supported along all four edges to inhibit buckling.

2.5.3 Residual Flexural Strength

Less work has been done in this area, but it has been reported that both flexural modulus and strength decreased with increasing low-velocity impact energy for ductile specimens (glass/epoxy) whilst brittle graphite/epoxy exhibited no losses until complete failure occurred (Abrate 1991).

2.5.4 Residual Fatigue Life

Generally, the degradation of composite materials under cyclic loading occurs by growth of cracks through the matrix or at the fiber-matrix interface (Challenger 1986). With fiber-dominated, carbon-epoxy matrix material, the fatigue SN curve is almost flat (Demuts 1990), and it is usually considered that impact damage has more effect on static strength than fatigue life.

2.6 Consideration of Impact Damage in Structural Design

Since impact damage may cause significant strength degradation, in the design of a structural component it is important to obtain a sufficiently low failure probability. This probability must of course be balanced with other primary needs such as functionality, weight, accessibility etc. The failure probability depends both on the strength of the

component and on the severity of the loads. Both the strength and the loads show statistical variation.

Applying safety factors is the traditional way of considering the variations and uncertainties. The larger the variation and the uncertainties the larger safety factors are normally required. The somewhat simplified case in **Figure 2-9** (The area under both curves represents failure conditions) exemplifies that when the product design produces higher strength levels, failure probability decreases; in other words, to ensure a specific failure probability, it is necessary to introduce an extra strength margin.

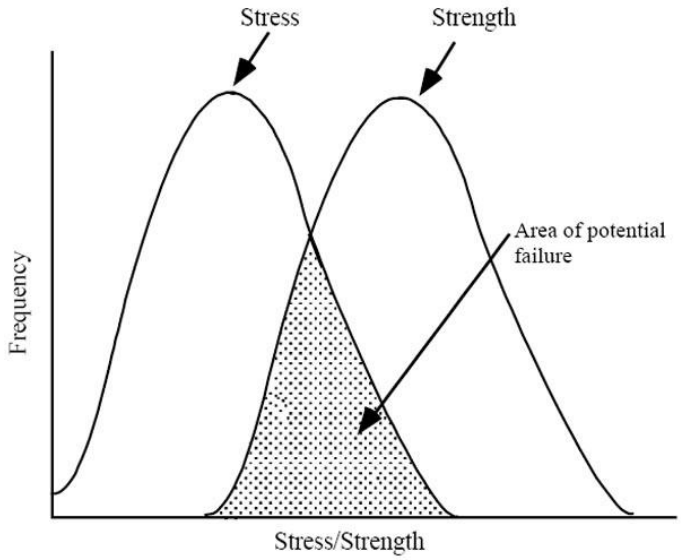

Figure 2-9: Failure probability between stress and strength. (RIAC n.d.)

The potential to prevent damages is strongly linked to the design requirements and how these requirements are in practice implemented. The needs for in service damage preventing measures are to a large extent determined by the design. The design of the component should provide margins against the damage mechanisms, thus providing sufficient robustness for the component in service. Otherwise increased

sensitivity may be the case, where deviations from the expected conditions may reduce margins so that failure occurs.

In wind turbine industry, as an example, more advanced damage tolerance concepts (Hayman 2007) are being gradually incorporated in the design process of critical elements of composite blades, so as to take full advantage of the weight-saving potentiality offered by sandwich materials. Design schemes based on a damage tolerance approach (Sierakowski 2000) (Zenkert, et al. 2005) accept the presence of pre-existing damage (such as that introduced during manufacturing or induced by accidental loads) and verify that the structure retain the required residual properties in the presence of the assumed damage. Reliable design procedures for composite blades should therefore include a reasonably accurate estimation of the internal damage locally induced by possible impacts, and ensure that the existing damage does not immediately lower the load carrying capability of the component below the design level, and will not grow to critical sizes under service loads, thus reducing the long term performance of the structure.

2.7 Concluding Remarks

Composite structures are extremely susceptible to damage caused by foreign object impacts which may be expected to occur during the whole life span of a structure. A number of experimental test procedures and technologies have been suggested to study impact damage. Experimental investigations show that impact-induced damage consists of a complex combination of different failure modes and may cause a substantial degradation of residual mechanical properties of composite structures. Damage tolerance concepts are being gradually incorporated in design of composite structures.

CHAPTER 3

MODELLING OF IMPACT DAMAGE IN COMPOSITES

3.1 Impact Damage in Laminated Composites

A number of modelling approaches and procedures have been proposed in the literature to predict the extent of interlaminar and intralaminar damage resulting from impact in monolithic laminates (Elder, et al. 2004).

Progressive damage models have been extensively used in recent years to incorporate onset and growth of failure mechanisms and nonlinear material behaviour in FE-based simulations of the impact response of laminated composites (Iannucci, Dechaene, et al. 2001) (Iannucci 2006) (Aoki, Suemasu and Ishikawa 2007) (Donadon, et al. 2008) (Aymerich, Dore and Priolo 2008) (Lopes, et al. 2009) (Faggiani and Falzon 2010). In progressive damage procedures, failure criteria are first used to evaluate the onset of damage, and material degradation rules are then introduced in the constitutive model to simulate the reduction of elastic properties due to material degradation (Garnich and Akula 2009).

In particular, energy-based stiffness degradation schemes developed in the framework of continuum damage mechanics (CDM) and based on the assumption that the fracture energy is distributed over the element volume (smeared crack approach) are

being increasingly considered to simulate the initiation and growth of intralaminar damage mechanisms such as matrix cracking and fibre fracture.

Even though continuum damage mechanics has also been adopted in the past for the simulation of interlaminar damage (Tay, et al. 2008), this approach is not particularly suited to model discrete failure modes such as delaminations, which are characterized by highly localized stress fields and invariably occur at the thin interface between contiguous layers (Wisnom 2010); for this reason, modelling methods based on fracture mechanics, such as the Virtual Crack Closure method (VCC) or a range of cohesive interface models (Elder, et al. 2004) (Wisnom 2010), are now more widely adopted to study the growth of interlaminar damage by FE analyses. The VCC technique is a well established method that provides the strain energy needed for delamination propagation by evaluating the amount of work required to close the crack. However, the VCC technique requires the definition of a pre-existing crack and is very sensitive to both the geometry of the mesh and the size of the elements at the crack tip, thus entailing the implementation of elaborate adaptive re-meshing techniques in order to conform the mesh to the moving boundaries of the delaminated area.

In cohesive interface models, a process zone delimited by cohesive surfaces that are held together by cohesive tractions is assumed to develop ahead of the delamination front. The cohesive tractions are related to the relative displacements of the cohesive surfaces by special constitutive laws that describe the accumulation of damage through progressive decohesion of the interface. Cohesive zone models overcome the main limitations of VCC methods, since the initiation of damage is explicitly incorporated in

the cohesive model and requirements on mesh geometry and mesh density are not as strict as those posed by VCC analyses (Turon, et al. 2007).

Cohesive elements placed at the interfaces between layers were for example successfully used in various studies to model delaminations induced by low-velocity impact in cross-ply composite laminates (Aymerich, Dore and Priolo 2009) (Amaro, Santos and Cirne 2011). The combined effect of intralaminar and interlaminar damage was investigated in further analyses, where cohesive (De Moura and Gonçalves 2004) (Aoki, Suemasu and Ishikawa 2007) (Aymerich, Dore and Priolo 2008) (Zhang, Zhu and Lai 2006) or special spring elements (Bouvet, et al. 2009) were used for modelling both delaminations at the interfaces between layers and major matrix cracks (such as bending cracks on the bottom layer and shear matrix cracks in the middle layers) developing in impacted laminates.

However, while cohesive elements are especially suitable for modelling cracks that are constrained to propagate along well defined fracture surfaces (such as delaminations at the interfaces between layers), their use may be problematic for simulation of intralaminar matrix cracking in cases where the site of crack initiation is not known in advance, such as for damage generated by transverse impact loads. Even when placing cohesive interface elements along all interelement boundaries (which would likely result in extremely long computation costs), the geometry of the FE mesh would restrict the direction of crack propagation to the orientations of the element sides, and the presence of the cohesive surfaces would inevitably introduce a spurious artificial compliance to the undamaged structure (de Borst, Remmers and Needleman 2006).

Simulation schemes based on the combined use of continuum damage mechanics (CDM) models and cohesive surface elements have been recently proposed to simulate interlaminar and distributed intralaminar damage in laminates subjected to impact.

In-plane CDM damage models controlled by energy dissipation and taking into account the nonlinear behaviour of the layers under shear loading were for example implemented by Iannucci and Willows (Iannucci and Willows 2006) (Iannucci and Willows 2007) into an explicit dynamic code for predicting, in association with interface cohesive elements, the impact damage resistance of woven composite laminates.

The response to impact of multidirectional laminates was simulated in (Lopes, et al. 2009) (González, et al. 2012) using continuum damage mechanics models for simulation of in-ply damage (matrix cracking and fiber breakage damage mechanisms) and cohesive interface models for prediction of delamination growth under mixed-mode loading conditions. Delaminations predicted at the various interfaces were compared with experimental observations carried out by fluorescent penetrant inspection (Lopes, et al. 2009); good agreement between numerical simulations and experimental results was obtained in terms of damage features, even though shapes and absolute sizes of individual delaminations were not properly captured for some laminate layups.

Cohesive interface elements in association with in-ply damage models were also used in (Faggiani and Falzon 2010) (Shi, Swait and Soutis 2012) to simulate the structural and damage response to impact of quasi-isotropic or cross-ply laminated panels. Numerical predictions of planar damage extent were in good agreement with experimental observations; no comparisons were however provided to assess the accuracy of predictions for individual delaminations on an interface-by-interface basis.

3.2 Impact Damage in Sandwich Composites

As opposed to monolithic laminates, the investigation on the behaviour of sandwich composites under impact has been the focus of a rather limited number of studies. The analysis of the impact performance of sandwich composites is significantly more complex than that of monolithic laminates, because of the need to introduce in the model the interaction between the laminated skins and the core material which generally exhibits strongly nonlinear mechanical properties (Daniel 2010).

Shell elements implementing only in-plane damage modes have been generally used to simulate the damage induced by impact in the laminated skins of sandwich composites. Besant and coworkers (Besant, Davies and Hitchings 2001) utilized for example 8-noded shell elements for the skins and brick elements for the core to investigate the impact behaviour of sandwich panels with carbon-epoxy skins and aluminium honeycomb core. The honeycomb core was modelled as an anisotropic elasto-plastic material, while in-plane fibre and matrix damage of the laminated skins was simulated using the Chang-Chang failure models, and applying a ply-level degradation of the stiffness properties of the damaged material. Shell elements together with the Chang-Chang damage models were also used in (Meo, Vignjevic and Marengo 2005) (Nguyen, Jacombs and Thomson 2005) (Klaus, Reimerdes and Gupta 2012) to simulate in-plane matrix and fibre damage modes occurring in the impacted skins of sandwich panels with carbon/epoxy facings and honeycomb or folded cores. A tiebreak contact formulation based on a cohesive approach and connecting shell elements representing sublaminates was used in (Klaus, Reimerdes and Gupta 2012) to model delaminations between layers.

A multilayer element was developed and applied in (Icardi and Ferrero 2009) to simulate low-velocity impacts on sandwich panels with carbon-epoxy skins and Nomex honeycomb core. Specialized stress-based failure criteria were used to predict the onset of interlaminar and intralaminar damage in the composite facings, while the stiffness degradation induced by damage accumulation was introduced by a ply-discount method.

Very few investigations have been carried out up to now to model impact damage in sandwich composites with the use of solid elements (Ivanez, Santiuste and Sanchez-Saez 2010) (Brooks, et al. 2010) (Feng and Aymerich 2013). Stress-based failure criteria were employed by Ivañez et al. (Ivanez, Santiuste and Sanchez-Saez 2010) to predict initiation of interlaminar and intralaminar damage in the glass/polyester facings of impacted sandwich beams with PVC foam core; the degradation of properties induced by damage was introduced through a simplified stiffness reduction scheme, where the stresses at damaged elements are reduced to near-zero values when the relevant failure criterion is met.

Similarly, a progressive damage model based on a continuum damage mechanics approach accounting for in-plane fibre and matrix damage, fibre crushing and delamination between layers, was used by Brooks et al. (Brooks, et al. 2010) to estimate impact damage in glass/polypropylene fabric facings of sandwich beams and plates with polypropylene foam core.

3.3 Damage Modelling in this Study

Under the framework of the thesis, a FE tool implementing energy-based CDM models and cohesive interface elements was developed and applied to predict the structural and damage response of foam-based sandwich composites subject to foreign

object impacts; and this work has been partly published in a few journals (Feng and Aymerich 2013) (Feng and Aymerich 2014). The model accounts for the initiation and propagation of the typical damage modes occurring in the composite skins (fibre fracture, matrix cracking and delaminations) by means of progressive failure models for intralaminar damage and interfacial cohesive laws for interlaminar damage, and describes the nonlinear behaviour of the foam core by a crushable foam plasticity model.

An extensive series of experimental analyses was designed and carried out to validate the developed FE model. Experimental data acquired during impact tests and subsequent damage evaluation analyses on sandwich panels consisting of carbon/epoxy facesheets bonded to PVC foam were compared with numerical results with the aim of assessing the capabilities of the proposed simulation tool for damage prediction in impacted composite sandwich structures.

3.4 Concluding Remarks

This chapter briefly reviewed the literature on modelling of impact damage in composite laminates and sandwiches. Cohesive zone model, fracture mechanics based approaches and crushable plasticity models are the state of art for numerical modelling of impact damage in composites and were adopted in this study.

CHAPTER 4

EXPERIMENTAL TESTS

4.1 Overview

Various configurations of sandwich panels were examined during the study to verify and validate the predictive capabilities of the damage models that will be described in the following chapter (CHAPTER 5).

The composite skins were made with unidirectional carbon/epoxy prepreg layers stacked to achieve the desired laminate layup. The prepreg materials are Texipreg® HS300/ET223, supplied by Seal, suitable for vacuum-bag-only processing at curing temperatures ranging between 85°C and 125°C (RDS01001 2004) with a fibre volume ratio of 0.62 and a nominal thickness of 0.32 mm.

The core material was closed cell PVC foam (DIAB Divinycell HP). Divinycell HP is an elevated temperature foam core grade, specifically developed for compatibility with low-medium temperature prepreg systems (DIAB 2006).

Sandwich panels with two different lamination sequences (a 5 layer cross-ply $[0/90_3/0]$ layup and a 10 layer $[0_3/+45/-45]_S$ layup) and three foam core densities (HP60, HP100 and HP160, with densities of 65, 100 and 160 kg/m^3, respectively) were manufactured for the experimental analyses. Sandwich panels with two dimensions (250

x 250 mm^2 and 350 x 350 mm^2) and with core thicknesses ranging from 10 mm to 40 mm were manufactured and examined in the study.

4.2 Specimen Preparation

Figure 4-1 illustrates the whole process of specimen preparation. The laminate facesheets were fabricated using prepreg lay-up method (Jang 1994); the raw prepreg tapes were profiled and cut to specified dimensions and shapes, then laid up ply-by-ply to form the desired lamination sequence of facesheets. Sandwich configuration was constructed by bonding the two stacked laminate facesheets to the core without the use of additional adhesive material.

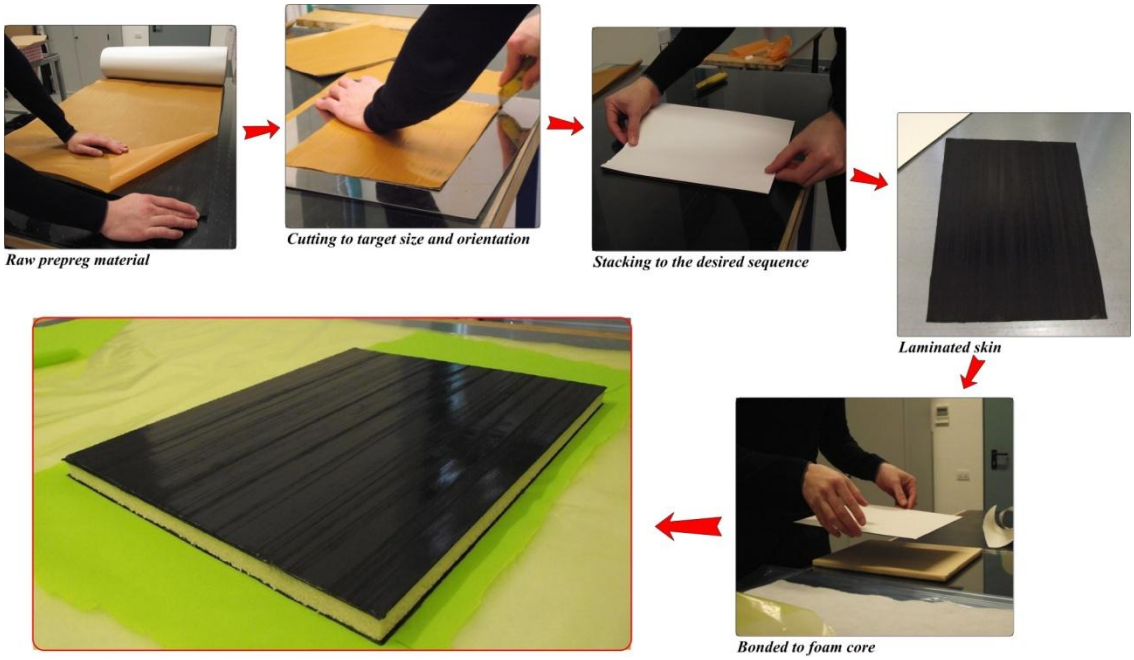

Figure 4-1: Preparation of sandwich panel.

To cure the sandwich specimens, vacuum bagging and autoclaving are required. **Figure 4-2** shows the vacuum bag configuration. The mold surface is covered with a non-sticking separator (Teflon film) on which the specimens are laid up. A porous release

cloth and a few layers of bleeder material are placed on top of the specimens. The bleeder layer absorbs the excess resin flowing out during the molding procedure. The whole stack is then covered with another sheet of separator, a caul plate, a breather and a thin hear resistant vacuum bag (a nylon film). The assembled vacuum bag, as shown in **Figure 4-3**, is then placed inside an autoclave (**Figure 4-4**) where a combination of heat and vacuum consolidates and cures the specimens.

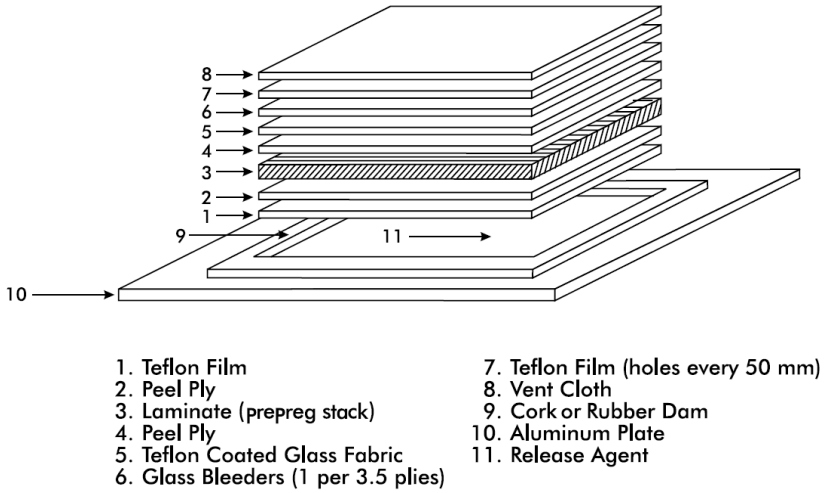

Figure 4-2: Vacuum bag configuration. (Carlsson, Adams and Byron 2003)

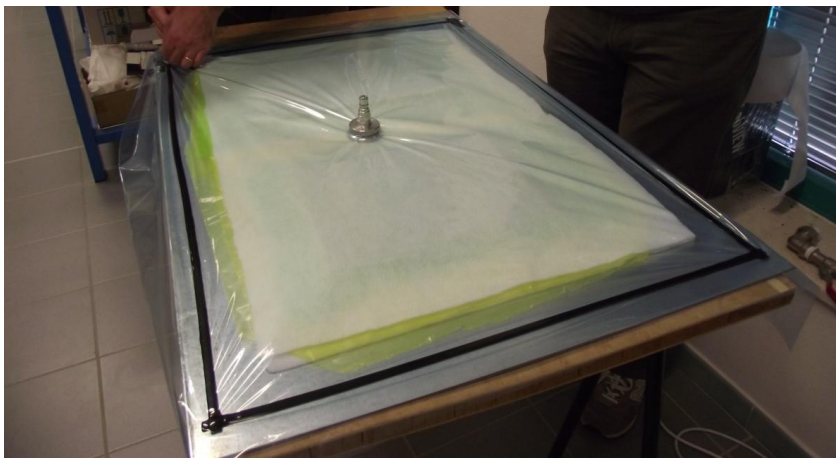

Figure 4-3: Vacuum bag assembly for autoclave cure.

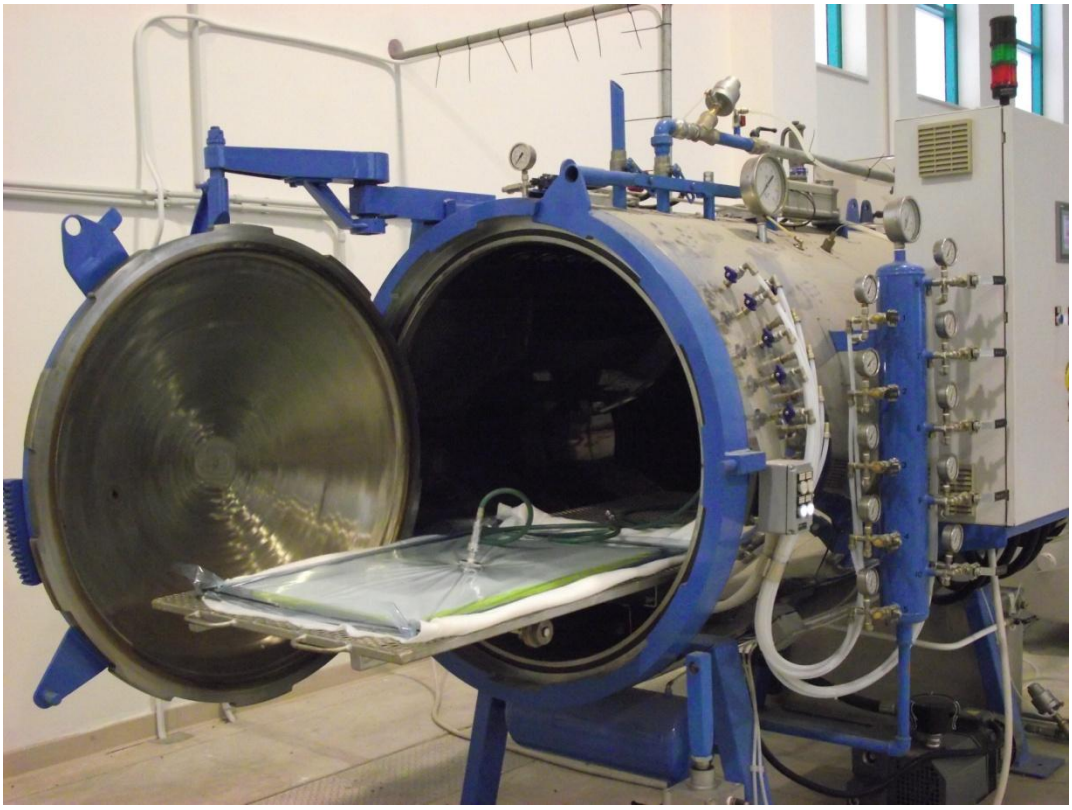

Figure 4-4: Vacuum bag sequence and tool plate placed in an autoclave.

Figure 4-5 illustrates the curing cycle: a 3°C/min heating stage, followed by a 6 h dwell at 100°C and a cooling stage to room temperature maintaining vacuum.

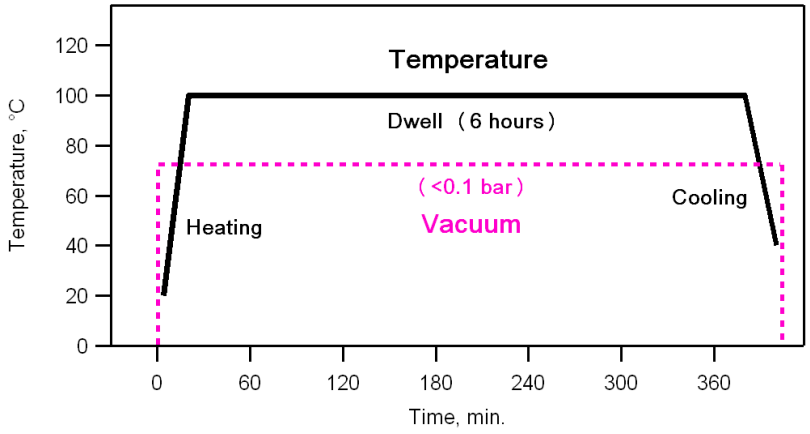

Figure 4-5: Cure cycle for composite specimen.

Figure 4-6 shows the specimens after curing process. They were firstly examined by ultrasonic C-scans to exclude the presence of significant manufacturing defects and then subjected to low-velocity impacts.

Figure 4-6: Samples of specimens after curing process.

4.3 Drop-Weight Test

Low-velocity impact tests were performed by an instrumented drop-weight testing machine, shown in **Figure 4-7**, using a 2.34 kg impactor with a hemispherical indentor of 12.5 mm diameter. The panels were subjected to impact with energies ranging between approximately 1 J and 9 J, obtained by varying the drop height of the impactor. It is worth remarking that energies up to about 8 J are suggested by the DNV design guidelines to characterize the impact damage resistance in wind turbine blades (DNV 2006). During impact, the 250 x 250 mm^2 sandwich panels were simply supported on a steel plate with a rectangular opening 45 mm x 67.5 mm in size. A number of impact tests were also conducted on the larger 350 x 350 mm^2 panels, which were simply supported along two opposite sides (with an inner span of 300 mm) and free over the other two edges.

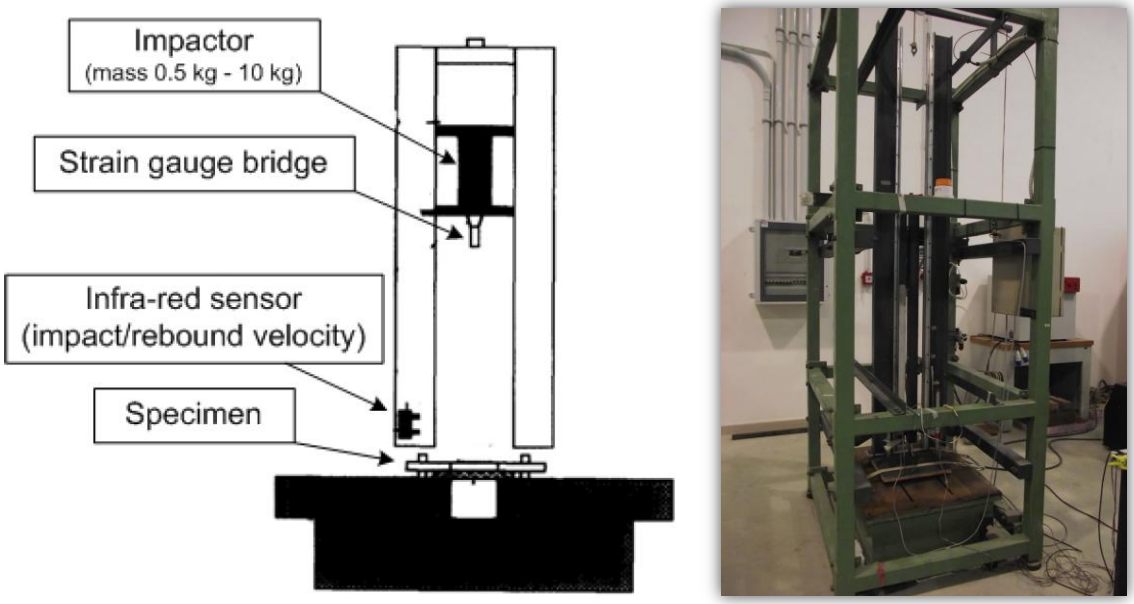

Figure 4-7: Drop-weight testing system.

The force–time history and the impactor velocity just before the impact, as respectively measured by a strain-gauge bridge bonded to the impactor tup and by an infra-red sensor, were recorded by a data acquisition unit. The absorbed energy and the history of indentor displacement were calculated by numerical integration of the force-time trace.

4.4 Damage Assessment

After impact tests, the sizes and shapes of damage areas were assessed by penetrant-enhanced X-radiography for all specimens. In a limited number of selected samples, the through-thickness distribution of impact-inflicted delaminations was further assessed by stereoscopic X-radiography (Palazotto, Maddux and Horban 1989) and validated by ultrasonic C-scans or optical microscopy of polished cross-sections.

Figure 4-8 and **Figure 4-9** show the X-radiography system and the ultrasonic scanning system, respectively. **Figure 4-10** shows an example of typical impact damage in facesheet of HP60 $[0_3/+45/-45]_S$ sandwich panel under a 6 J impact as obtained by X-radiography and stereoscopic X-radiography analyses.

Figure 4-8: X-radiography inspection system.

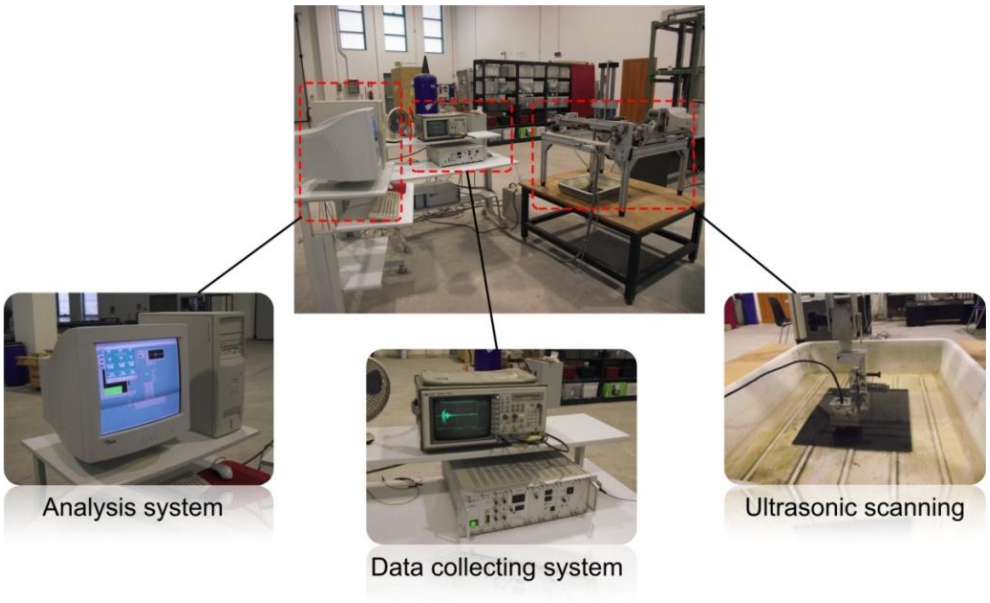

Figure 4-9: Ultrasonic scanning system.

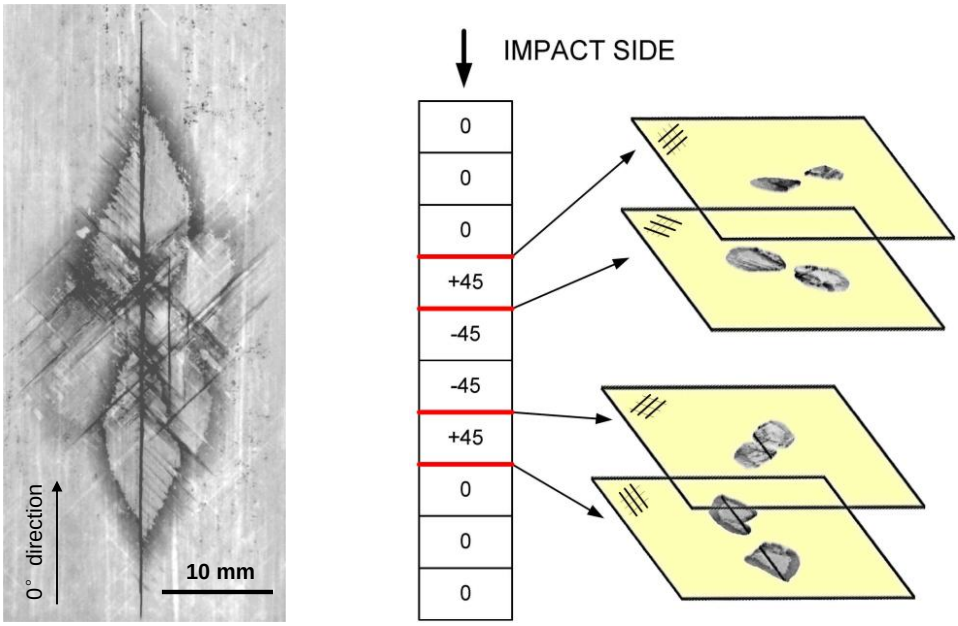

Figure 4-10: Typical damage picture obtained by X-radiography (left) and through-thickness distribution of delaminations constructed by stereoscopic X-ray (right): in facesheet of HP60 $[0_3/+45/-45]_S$ sandwich panel under an impact energy of 6J.

4.5 Characterization of Material Properties

The elastic and fracture properties used in the FE model were obtained by a series of experimental tests or provided by the material manufacturers. In particular, constitutive and strength properties of the unidirectional prepreg material were obtained by static tests on unidirectional and angle-ply laminates. Tensile tests were conducted on $[0]_4$, $[90]_4$ and $[+45/-45]_S$ coupon specimens according to the indications provided by the ASTM standard D3039/D3039M-08 (ASTM-D3039/D3039M-08 2008). Compressive tests were carried out on $[0]_{10}$ and $[90]_{10}$ samples with a gauge length of 10 mm (ASTM-D3410/D3410M-03 2008).

Fracture energies for matrix failure modes were determined by DCB, ENF and MMB tests on unidirectional laminates (Carlsson, Adams and Byron 2003). The tests

were performed on $[0]_{10}$ samples (120 mm long, 20 mm wide and 3.2 mm thick) containing an initial precrack obtained by placing a thin fluoroethylene polymer film at the laminate midplane. The pre-cracked specimens were loaded under pure mode I (DCB; $G_{II}/G_{tot} = 0$), pure mode II (ENF; $G_{II}/G_{tot} = 1$), and mixed-mode (MMB; $G_{II}/G_{tot} = 0.5$ and 0.8) loading using a 5 kN servo-electric testing machine operated at a crosshead speed of 1 mm/min. Both the force and displacement signals were recorded during the tests, while an optical microscope connected to a CCD camera was used to identify the initiation of crack propagation. The experimental compliance calibration methods (Berry 1963) (Carlsson, Gillespie and Trethewey 1986) were finally used to evaluate the fracture energy at the onset of delamination propagation; the cohesive interface strengths S and N were selected by fitting the results of numerical simulations to the experimental curves of DCB and ENF tests.

Fibre fracture energy values evaluated for a different carbon/epoxy system (Faggiani and Falzon 2010) were used as input to the model owing to the lack of experimental data for the HS300/ET223 prepreg system.

Flatwise transverse compression tests were performed on the HP60, HP100 and HP160 PVC foams at a nominal strain rate of 0.1/s using a screw-driven test machine. The compressive load was measured by the load cell of the test machine, while the compressive strain was deduced from the relative displacement of the compression platens.

4.6 Concluding Remarks

The whole process of experimental tests to investigate impact-induced damage including specimen preparation, impact test and damage characterization was illustrated; Various experimental tests aiming at obtaining the mechanical properties of the material, which would be used in the numerical simulations, were also presented in this chapter.

CHAPTER 5

PROGRESSIVE DAMAGE MODELS

5.1 Fracture Mechanics

The failure models developed in this study are based on fracture mechanics. Fracture mechanics is the field of mechanics concerned with the study of the propagation of cracks in materials. It uses methods of analytical solid mechanics to calculate the driving force on a crack and those of experimental solid mechanics to characterize the material's resistance to fracture.

In modern materials science, fracture mechanics is an important tool in improving the mechanical performance of mechanical components. It applies the physics of stress and strain, in particular the theories of elasticity and plasticity, to the microscopic/ macroscopic defects found in real composites in order to predict the mechanical failure of bodies. Fractography is widely used with fracture mechanics to understand the causes of failures and also verify the theoretical failure predictions with real life failures. The prediction of crack growth is at the heart of the damage tolerance discipline. **Figure 5-1** illustrates the three ways of applying a force to enable a crack to propagate:

- *Mode I fracture* - Opening mode (a tensile stress normal to the plane of crack),
- *Mode II fracture* - Sliding mode (a shear stress acting parallel to the plane of crack and perpendicular to the crack front),

and

- *Mode III fracture* - Tearing mode (a shear stress acting parallel to the plane of crack and parallel to the crack front).

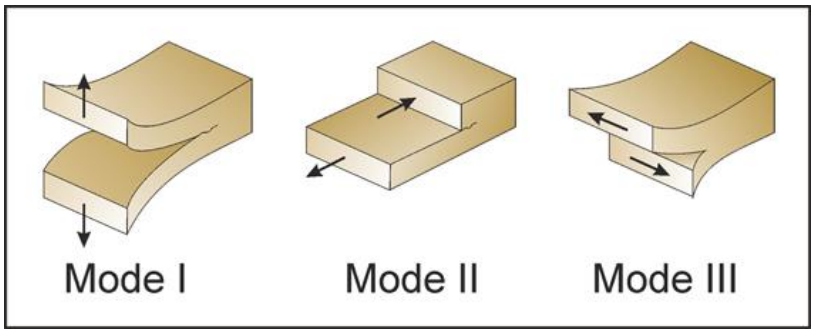

Figure 5-1: The three fracture modes. (Philipp, Afsar and Gudmundsson 2013)

5.2 Interlaminar Failure Models

5.2.1 Modelling Approaches

A large number of predictive methods have been proposed in the literature to simulate initiation and growth of interlaminar delamination in impacted composite structures (Elder, et al. 2004).

Although stress-based continuum damage mechanics has been used in the past to study delamination in composites (Allix, Ladeveze and Corigliano 1995) (Tay, et al. 2008), this approach is not particularly suited to model discrete failure phenomena characterized by highly localized stresses at geometrical or material discontinuities (Wisnom 2010), and fracture mechanics is now more widely adopted to analyze the progression of interlaminar cracks by means of FE-based procedures such as the Virtual Crack Closure technique (VCC) or cohesive zone models (Elder, et al. 2004) (Wisnom

2010) (T. Tay 2003) (Camanho, Davila and De Moura 2003). The VCC approach is however very sensitive to mesh geometry and density, and requires both the assumption of a pre-existing crack and the application of adaptive re-meshing techniques in order to adjust the mesh to changes in the shape of the delamination front (T. Tay 2003). The use of cohesive zone models, which combine strength-based criteria to predict damage initiation with fracture mechanics energy criteria to simulate damage propagation and subsequent fracture, allows to overcome the main limitations of VCC analyses and cohesive interface elements have gained special interest in various studies for the simulation of discrete failure modes in impacted composites (Cui and Wisnom 1993) (Mi, et al. 1998) (Camanho, Davila and De Moura 2003) (Borg, Nilsson and Simonsson 2004) (Wisnom 2010).

5.2.2 Cohesive Zone Model

In contrast to continuum elements where stress-strain relations are used, relations between tractions and relative displacements of the interface surfaces govern the behavior of cohesive elements. Cohesive elements do not represent any physical component, but describe the traction forces to resist surfaces being pulled apart. The Fracture of cohesive elements is regarded as a gradual phenomenon in which separation occurs across an extended crack tip, or cohesive process zone (see **Figure 5-2**) when cohesive tractions (Ortiz and Pandol 1999) between upper and lower surfaces reach a prescribed criterion.

Various cohesive traction-displacement constitutive equations have been proposed in the literature to represent the initiation and evolution of an interface model (Shet and Chandra 2002). Many studies indicate however that the numerical results show

little sensitivity to the shape of the cohesive law (Williams and Hadavinia 2002) (Alfano 2006); a bilinear constitutive law, as shown in **Figure 5-3**, which is possibly the most widely adopted cohesive curve, was thus used in this study to model each specific failure mode because of its implementation simplicity.

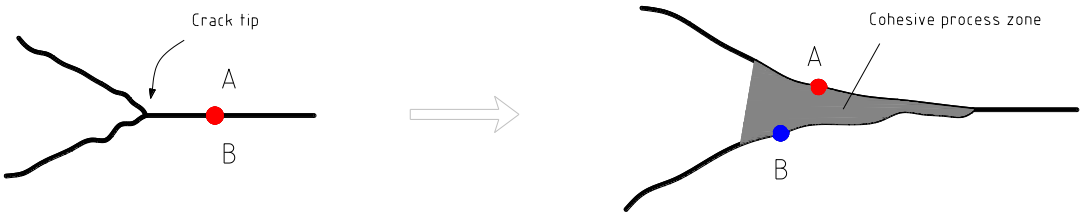

Figure 5-2: Diagram of cohesive zone model.

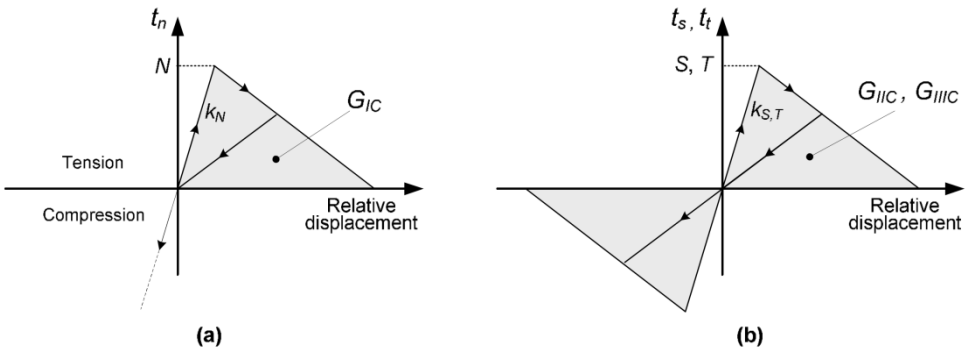

Figure 5-3: Cohesive model behaviour for mode I (a) and mode II/III (b) loading.

The implementation of constitutive law consists of three ingredients: a damage initiation criterion, a damage evolution law, and a choice of element removal upon reaching a completely damaged state. Damage initiation refers to the beginning of degradation of the response of a material point and is predicted using strength-based failure criteria. Damage evolution law describes the rate at which the material stiffness is degraded once the corresponding initiation criterion is reached; the evolution of damage

is defined using fracture mechanics criteria and monitored by a damage indicator d, ranging from the value of 0.0 for the undamaged interface to the value of 1.0 corresponding to complete decohesion of the interface. The cohesive elements would remain in the model even after having completely degraded ($d = 1.0$) to resist interpenetration of the surrounding components.

Since delamination failure is driven by a combination of shear and normal stresses, the mixed mode behavior of interface elements needs to be taken into account. The choice of an appropriate criterion for prediction of damage initiation and propagation under mixed-mode loadings is still a subject of much debate, since many unsolved issues, such as the apparent increase of shear strength under compressive loading, in situ effects, the influence of material non-linearity, the adoption of a characteristic length, etc., remain to be clarified (Hinton, Kaddour and Soden 2002) (Orifici, Herszberg and Thomson 2008).

In particular, it is indicated by the literature (Li, et al. 2006) (Christensen and Deteresa 2004) (Deteresa, Freeman and Groves 2004) (Hart-Smith 1993) that through-thickness compression can have an enhancing effect on both the shear strength and mode II fracture toughness. Some researchers such as Deteresa et al. (Deteresa, Freeman and Groves 2004) (Christensen and Deteresa 2004) take this strengthening effect of compression on shear strength into account by modifying the stress interaction criterion as below:

$$\frac{\sigma_{33}}{Z_f} + \frac{\sigma_{13}^2 + \sigma_{23}^2}{S_{shear}^2} \leq 1 \qquad \textbf{Eq. 5-1}$$

where Z_f is the normal strength in through-thickness direction and S_{shear} is the shear strength. Other investigations such as those by Hart-Smith (Hart-Smith 1993) (Hart-Smith 1998), Sun and Tao (Sun and Tao 1998) and Rotem (Rotem 1998) suggest it is the result of in situ effects in laminates. Work by Cui et al. (Cui, Wisnom and Jones 1994) reveals that the through-thickness compression can suppress delamination in terms of increasing the critical mode II fracture energy (G_{IIC}) which was expressed as a linear function of average through-thickness normal stress. Li et al. (Li, Hallett and Wisnom 2008) carried out a further investigation and suggests that the increase of G_{IIC} is actually a corresponding result of the increased shear strength, and that the normal compression can significantly suppress delamination by increasing both the shear strength and fracture energy.

In this study, cohesive zone model with the criterion proposed in (Li, Hallett and Wisnom 2008), which includes the strengthening effect of through-thickness compression on the shear strength of the interface was adopted for the prediction of interlaminar delamination at interfaces between laminar layers.

5.2.3 Failure Criteria

The implemented failure mechanism is based on the Wisnom Criterion (Li, Hallett and Wisnom 2008):

$$\begin{cases} \left(\frac{t_n}{N}\right)^2 + \left(\frac{t_s}{S}\right)^2 + \left(\frac{t_t}{T}\right)^2 = 1 \\ \left(\frac{G_I}{G_{IC}}\right) + \left(\frac{G_{II}}{G_{IIC}}\right) + \left(\frac{G_{III}}{G_{IIIC}}\right) = 1 \end{cases} \quad \text{for} \quad t_n \geq 0 \qquad \textbf{Eq. 5-2}$$

$$\begin{cases} \left(\frac{t_s}{S^*}\right)^2 + \left(\frac{t_t}{T^*}\right)^2 = 1 \\ \left(\frac{G_{II}}{G_{IIC}}\right) + \left(\frac{G_{III}}{G_{IIIC}}\right) = 1 \end{cases} \quad \text{for} \quad t_n < 0 \qquad \textbf{Eq. 5-3}$$

Under through-thickness compressive loading, it's supposed that the through-thickness compressive stress does not influence the elastic modulus but increases the shear strength and the final failure displacement (**Figure 5-4**). After initial failure, the slope of the softening part of the curve is the same as that of the un-enhanced model. (It is thus needed to define a parameter η_f, which is analogous to an internal friction enhancement factor.)

$$\begin{cases} S^* = S - \eta_f \sigma_{33} \\ \sigma_S^{0*} = S^*/K_S = (S^*/S)\sigma_S^0 \\ \sigma_S^{f*} = (S^*/S)\delta_S^f \\ G_S^* = G_S(1 - \eta_f \sigma_{33}/S)^2 \end{cases} \qquad \textbf{Eq. 5-4}$$

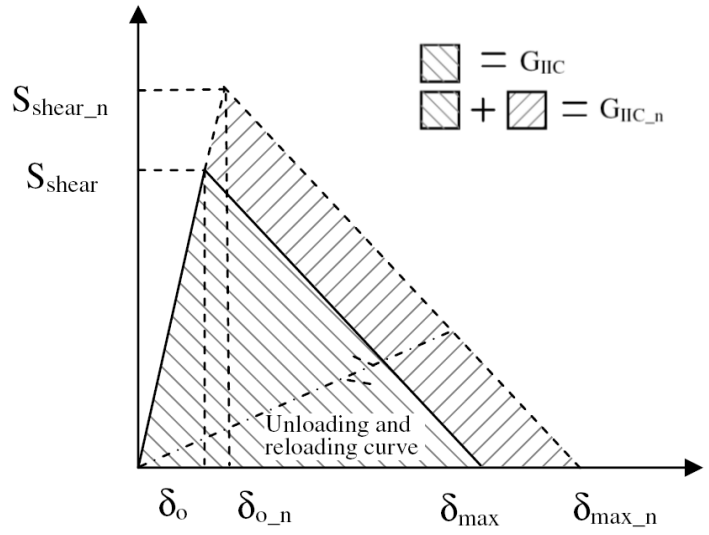

Figure 5-4: Mode II damage evolution law under through-thickness compressive stress. (Li, Hallett and Wisnom 2008)

The derivation of key parameters δ_m^0 and δ_m^f are as follows:

If $\delta_3 \geq 0$

From equation **Eq. 5-2**, we can express the components in terms of trigonometric functions:

$$\begin{cases} \frac{\sigma_3^0}{\mathrm{N}} = \frac{K_3\delta_3^0}{K_3\delta_3^{0*}} = \frac{\delta_3^0}{\delta_3^{0*}} = cos\theta \\ \frac{\tau_2^0}{\mathrm{S}} = \frac{K_2\delta_2^0}{K_2\delta_2^{0*}} = \frac{\delta_2^0}{\delta_2^{0*}} = sin\theta cos\varphi \\ \frac{\tau_1^0}{\mathrm{T}} = \frac{K_1\delta_1^0}{K_1\delta_1^{0*}} = \frac{\delta_1^0}{\delta_1^{0*}} = sin\theta sin\varphi \end{cases} \quad \textbf{Eq. 5-5}$$

Here, $\mathrm{K}_3, \mathrm{K}_2, \mathrm{K}_1$ denote the penalty stiffness in normal and shear direction respectively; $\delta_3^0, \delta_2^0, \delta_1^0, \sigma_3^0, \tau_2^0, \tau_1^0$ denote the normal and shear displacements and stresses corresponding to the damage initiation under mixed-mode; while $\delta_3^{0*}, \delta_2^{0*}, \delta_1^{0*}, \mathrm{N}, \mathrm{S}, \mathrm{T}$ denote normal and shear displacement thresholds (damage initiation) and corresponding strengths under pure mode I, II or III. For any loading state, a relationship exists between the current displacements δ_3 , δ_2 , δ_1 and the displacements $\delta_3^0, \delta_2^0, \delta_1^0$ corresponding to damage initiation under this specific mode ratio:

$$\frac{\delta_3}{\delta_3^0} = \frac{\delta_2}{\delta_2^0} = \frac{\delta_1}{\delta_1^0} = \mathrm{k}$$

Then, we define parameters:

$$\begin{cases} \beta_3 = \frac{\delta_3}{\delta_3} = \frac{\delta_3^0}{\delta_3^0} = 1 \\ \beta_2 = \frac{\delta_2}{\delta_3} = \frac{\delta_2^0}{\delta_3^0} \\ \beta_1 = \frac{\delta_1}{\delta_3} = \frac{\delta_1^0}{\delta_3^0} \end{cases} \quad \textbf{Eq. 5-6}$$

By combining **Eq. 5-5** and **Eq. 5-6**, we can get:

$$\tan\varphi = \frac{\beta_1\delta_2^{0*}}{\beta_2\delta_1^{0*}};\quad \tan\theta = \sqrt{\frac{\left(\frac{\delta_2^0}{\delta_2^{0*}}\right)^2+\left(\frac{\delta_1^0}{\delta_1^{0*}}\right)^2}{\left(\frac{\delta_3^0}{\delta_3^{0*}}\right)^2}} = \sqrt{\frac{\left(\beta_2\delta_1^{0*}\delta_3^{0*}\right)^2+\left(\beta_1\delta_2^{0*}\delta_3^{0*}\right)^2}{\left(\delta_2^{0*}\delta_1^{0*}\right)^2}}$$

$$\sin^2\varphi = \frac{\left(\beta_1\delta_2^{0*}\right)^2}{\left(\beta_2\delta_1^{0*}\right)^2+\left(\beta_1\delta_2^{0*}\right)^2};\ \cos^2\varphi = \frac{\left(\beta_2\delta_1^{0*}\right)^2}{\left(\beta_2\delta_1^{0*}\right)^2+\left(\beta_1\delta_2^{0*}\right)^2}$$

$$\sin^2\theta = \frac{(\beta_2\delta_1^{0*}\delta_3^{0*})^2+(\beta_1\delta_2^{0*}\delta_3^{0*})^2}{(\delta_2^{0*}\delta_1^{0*})^2+(\beta_2\delta_1^{0*}\delta_3^{0*})^2+(\beta_1\delta_2^{0*}\delta_3^{0*})^2}$$

$$\cos^2\theta = \frac{(\delta_2^{0*}\delta_1^{0*})^2}{(\delta_2^{0*}\delta_1^{0*})^2+(\beta_2\delta_1^{0*}\delta_3^{0*})^2+(\beta_1\delta_2^{0*}\delta_3^{0*})^2}$$

So, the key displacement parameters corresponding to damage initiation δ_{m}^{0} and total failure $\delta_{\mathrm{m}}^{\mathrm{f}}$ can be expressed as:

$$\delta_m^0 = \sqrt{(\delta_3^0)^2+(\delta_2^0)^2+(\delta_1^0)^2} = \sqrt{(\delta_3^{0*}\cos\theta)^2+(\delta_2^{0*}\sin\theta\cos\varphi)^2+(\delta_1^{0*}\sin\theta\sin\varphi)^2}$$

$$= \sqrt{\frac{(\delta_3^{0*}\delta_2^{0*}\delta_1^{0*})^2+(\beta_2\delta_1^{0*}\delta_2^{0*}\delta_3^{0*})^2+(\beta_1\delta_1^{0*}\delta_2^{0*}\delta_3^{0*})^2}{(\delta_2^{0*}\delta_1^{0*})^2+(\beta_2\delta_1^{0*}\delta_3^{0*})^2+(\beta_1\delta_2^{0*}\delta_3^{0*})^2}}$$

$$= \delta_3^{0*}\delta_2^{0*}\delta_1^{0*}\sqrt{\frac{1+\beta_2^2+\beta_1^2}{(\delta_2^{0*}\delta_1^{0*})^2+(\beta_2\delta_1^{0*}\delta_3^{0*})^2+(\beta_1\delta_2^{0*}\delta_3^{0*})^2}} \qquad \textbf{Eq. 5-7}$$

$$= \delta_3^{0*}\delta_2^{0*}\delta_1^{0*}\sqrt{\frac{\delta_3^2+\delta_2^2+\delta_1^2}{(\delta_3\delta_2^{0*}\delta_1^{0*})^2+(\delta_2\delta_1^{0*}\delta_3^{0*})^2+(\delta_1\delta_2^{0*}\delta_3^{0*})^2}}$$

$$= \sigma_{33_{\max}}\tau_{23_{\max}}\tau_{13_{\max}}\sqrt{\frac{\delta_3^2+\delta_2^2+\delta_1^2}{\left(\delta_3\mathrm{K}_3\tau_{23\_\max}\tau_{13\_\max}\right)^2+\left(\delta_2\mathrm{K}_2\sigma_{33\_\max}\tau_{13\_\max}\right)^2+\left(\delta_1\mathrm{K}_1\sigma_{33\_\max}\tau_{23\_\max}\right)^2}}$$

$$\delta_m^f = 2\mathrm{G}_3^{\mathrm{C}}\mathrm{G}_2^{\mathrm{C}}\mathrm{G}_1^{\mathrm{C}}\frac{\delta_3^2+\delta_2^2+\delta_1^2}{\delta_m^0\left[\left(\delta_3^2\mathrm{K}_3\mathrm{G}_2^{\mathrm{C}}\mathrm{G}_1^{\mathrm{C}}\right)^{\alpha}+\left(\delta_2^2\mathrm{K}_2\mathrm{G}_3^{\mathrm{C}}\mathrm{G}_1^{\mathrm{C}}\right)^{\alpha}+\left(\delta_1^2\mathrm{K}_1\mathrm{G}_3^{\mathrm{C}}\mathrm{G}_2^{\mathrm{C}}\right)^{\alpha}\right]^{\frac{1}{\alpha}}} \qquad \textbf{Eq. 5-8}$$

If $\delta_3 < 0$, from **Eq. 5-3**, the key parameters can be easily obtained:

$$\delta_m^0 = \delta_{shear}^0\left(1-\frac{\eta_{\mathrm{f}}\sigma_{33}}{\tau_{\mathrm{shear}}}\right) = \frac{\tau_{23\_\max}}{\mathrm{K}_2}\left(1-\frac{\eta_{\mathrm{f}}\mathrm{K}_3\delta_3}{\tau_{23\_\max}}\right) = \frac{\tau_{13\_\max}}{\mathrm{K}_1}\left(1-\frac{\eta_{\mathrm{f}}\mathrm{K}_3\delta_3}{\tau_{13\_\max}}\right) \qquad \textbf{Eq. 5-9}$$

$$\delta_m^f = \frac{2\mathrm{G}_{\mathrm{IIC}}}{\tau_{23\_\max}}\left(1-\frac{\eta_{\mathrm{f}}\mathrm{K}_3\delta_3}{\tau_{23\_\max}}\right) = \frac{2\mathrm{G}_{\mathrm{IIIC}}}{\tau_{13\_\max}}\left(1-\frac{\eta_{\mathrm{f}}\mathrm{K}_3\delta_3}{\tau_{13\_\max}}\right) \qquad \textbf{Eq. 5-10}$$

5.2.4 Implementation

The failure model was implemented in ABAQUS/Explicit through a User Subroutine VUMAT, the whole flowchart is plotted in **Figure 5-4**.

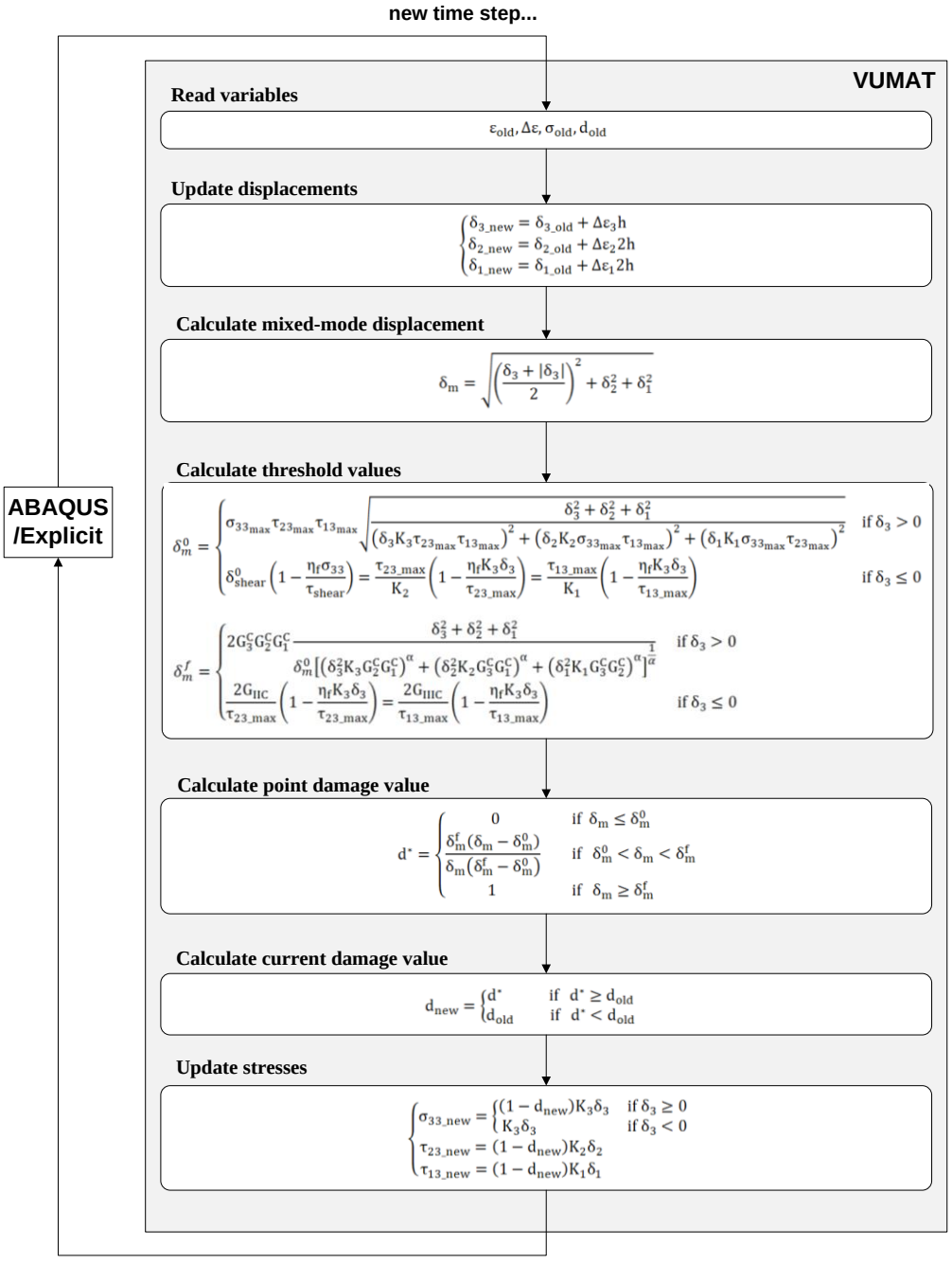

Figure 5-5: Flow diagram of VUMAT subroutine for interlaminar failure model.

5.2.5 Model Testing

The developed interlaminar failure model was tested with a single element model before being applied to numerical simulation; a single cohesive element model with size of 0.0005m × 0.0005m × 0.00002m, the same mesh size as that used for the numerical simulation of impact events (Chapter 7-10), was constructed.

The four nodes on the bottom face were fixed; the load was defined on the four nodes of the top face by imposing displacements U1 and U3, as shown in **Figure 5-6**, for shear loading and compressive loading, respectively. Both loading types were imposed in the way of smooth loading.

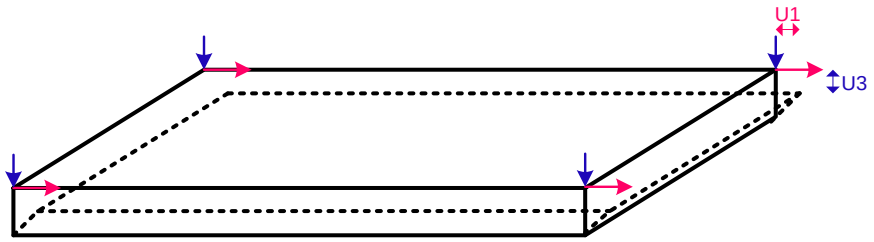

Figure 5-6: Single element model for testing the VUMAT.

The material properties used in the testing are the same with those used for the simulation of impacts in the following chapters and can be found in **Table 6-1**.

Firstly, the FE model was loaded without through-thickness compression (U3=0), which is actually pure mode II loading. The damage-load curve predicted by the model is shown in **Figure 5-7**. We can also easily calculate the theoretical solution:

$$\delta^0 = \frac{\mathrm{S\_shear}}{\mathrm{E_{shear}/h}} = \frac{60\mathrm{E6}}{857\mathrm{E6}/0.00002} = 1.40023\mathrm{E}-6\ \mathrm{m}$$

$$\delta^f = \frac{2G_{II}}{\mathrm{S\_shear}} = \frac{2 \times 900}{60\mathrm{E6}} = 3\mathrm{E}-5\ \mathrm{m}$$

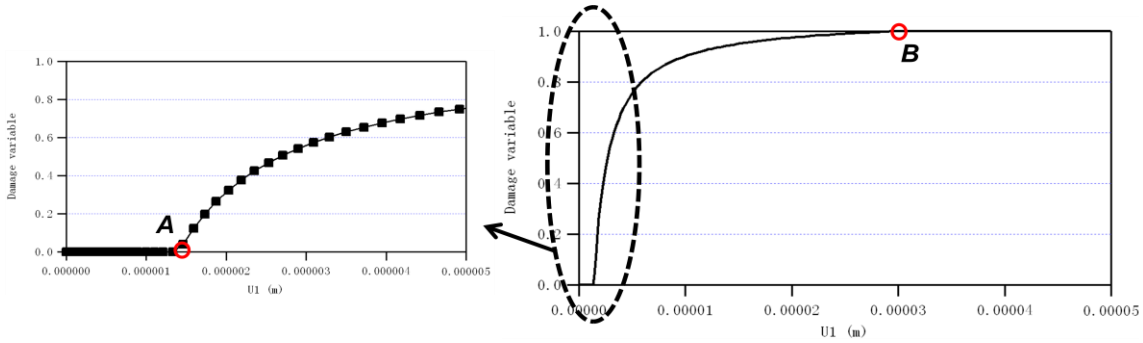

Figure 5-7: Damage-loading displacement curve predicted by the model.

If we plot the values on **Figure 5-7** as point A which represents the initiation of damage and point B representing the total damage, it is clearly shown that the numerical results correspond well with theoretical solutions.

Then, the model was loaded by shear together with different extents of through-thickness compression. The results are shown in **Figure 5-8**. Under the same shear loading condition, the damage initiates later and the damage variable reduces with the increase of through-thickness compression.

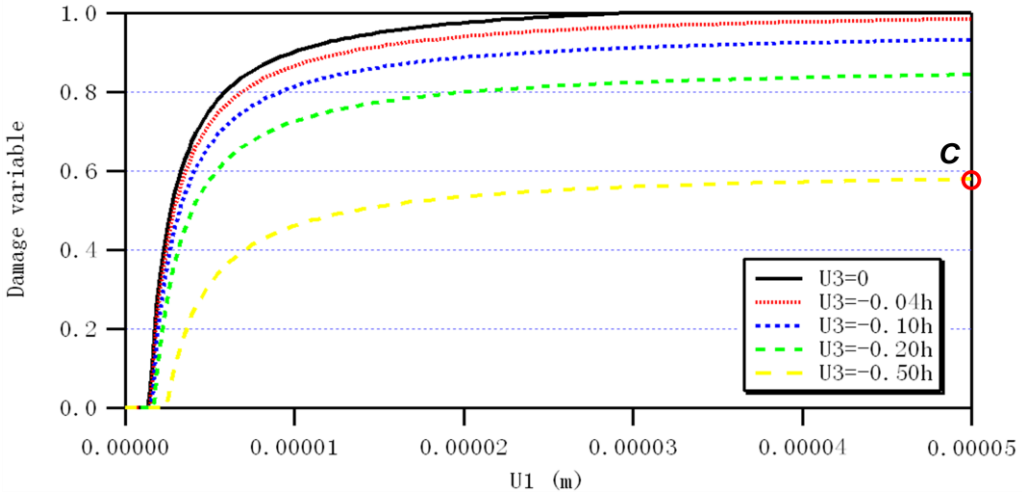

Figure 5-8: Damage-loading displacement curves for different through-thickness compression (h is the thickness of the cohesive element; $\eta_f = 0.75$).

Take the case U3=0.50h as an example, the theoretical solution is:

$$\delta_m^0 = \delta_{shear}^0 \cdot (1-\eta_f \cdot \sigma_{33}/\tau_{23\_max}) = \frac{\tau_{23\_max}}{K_2} \cdot \left(1-\frac{\eta_f \cdot K_3 \delta_3}{\tau_{23\_max}}\right)$$

$$= \frac{60E6}{857E6/(20E-6)} \cdot \left(1-\frac{0.75\times 2400E6\times(-0.5)}{60E6}\right) = 0.0000224 \text{ m}$$

$$\delta_m^f = \frac{2G_{IIC}}{\tau_{23\_max}} \cdot \left(1-\frac{\eta_f \cdot K_3 \delta_3}{\tau_{23\_max}}\right) = \frac{2*900}{60E6} \cdot \left(1-\frac{0.75\times 2400E6\times(-0.5)}{60E6}\right) = 0.00048 \text{ m}$$

$$d = \frac{\delta_m^f(\delta_m - \delta_m^0)}{\delta_m(\delta_m^f - \delta_m^0)} = \frac{0.00048\times(0.00005-0.0000224)}{0.00005\times(0.00048-0.0000224)} = 0.579021$$

Again, the numerical and theoretical solutions agree well with each other, as shown in **Figure 5-8** (point C).

As the final testing case, **Figure 5-9** illustrates the effect of parameter η_f. Larger η_f value means higher through-thickness compression, thus leading to a postponed and less development of delamination.

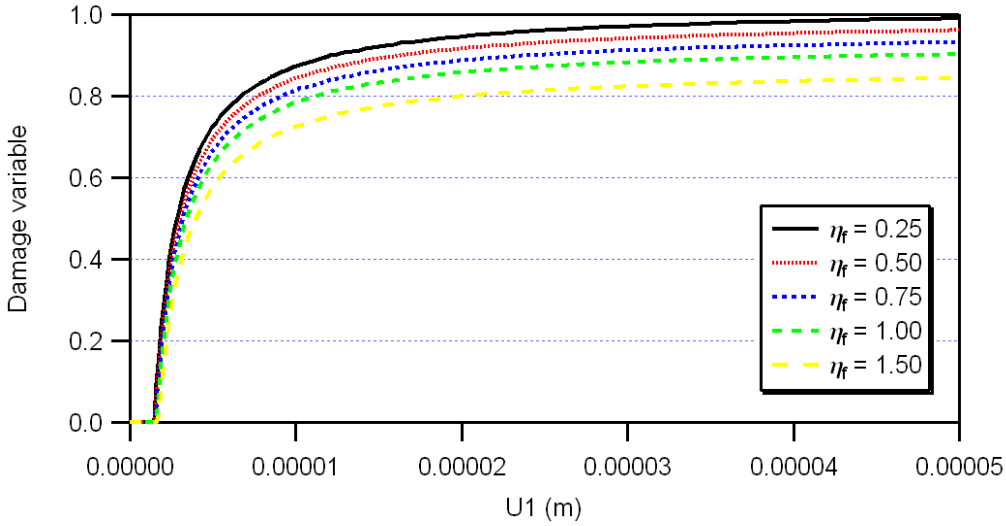

Figure 5-9: Damage-loading displacement curves obtained with different values of parameter η_f.

5.3 Intralaminar Failure Models

5.3.1 Modelling Approaches

Various models and criteria have been proposed in the last decades to describe the intralaminar failures in composite materials subjected to low-velocity impacts.

A large number of strength-based failure criteria have been proposed to relate stresses and experimental measures of material strength for prediction of intralaminar failure in composite materials (Soden, Hinton and Kaddour 1998) (Da´vila, Camanho and Rose 2005) (Pinho, et al. 2005). Failure criteria predict the onset of the different damage mechanisms occurring in composites and, depending on the material, the geometry and the loading conditions, may also predict final structural collapse.

For composite structures that can accumulate damage before final collapse, the use of strength-based failure criteria is not sufficient to predict ultimate failure (Maimí, Camanho, et al. 2007). Simplified models, such as the ply discount method, can be used to predict ultimate failure, but they cannot represent with satisfactory accuracy the quasi-brittle failure of laminates that results from the accumulation of various failure mechanisms. The study of the non-linear response due to the accumulation of damage is very important because the rate and direction of damage propagation define the damage tolerance of a structure and its eventual collapse.

Various strategies for progressive damage modelling based on a smeared crack approach, which considers the fracture energy distributed over the element width, have been developed and extensively used in the last decade to simulate intralaminar damage in composites (Iannucci 2006) (Donadon, et al. 2008) (Maimí, Mayugo and Camanho 2008) (Falzon and Apruzzese 2011). Typical progressive damage models integrate the

use of failure criteria with the application of material degradation procedures, to simulate, respectively, the initiation of damage and the reduction of elastic properties due to the degradation of the material (Garnich and Akula 2009).

Continuum damage mechanics (CDM), originally proposed by Kachanov (Kachanov 1987) and further developed by Lemaitre and Chaboche (Lemaitre and Chaboche 1990), has been increasingly used in recent years to deal with modelling of impact damage in composite laminates. Iannucci et al. (Iannucci, Dechaene, et al. 2001) developed and implemented a two-dimensional CDM model into the explicit FE package LS-DYNA to predict matrix cracks and fibre fracture in composite laminates subjected to elevated strain rates The model was later improved and extended to a full 3D formulation (Donadon, et al. 2008) (Faggiani and Falzon 2010). Donadon et al. (Donadon, et al. 2008) developed a 3D failure model which enables the control of the energy dissipations associated with individual failure modes and includes shear non-linearities and shear damage using a coupled semi-empirical elasto-damageable-plastic material law. Analogous damage models were recently used by Faggiani and Falzon (Faggiani and Falzon 2010) to simulate, in association with cohesive interface elements introduced for capturing interlaminar damage, the response of a stiffened composite panel under low-velocity impact.

In this study, progressive failure models based on continuum damage mechanics are used to model intralaminar failure mechanisms of laminate skins.

5.3.2 Constitutive Law

The intralaminar damage models implemented in this study follow the approach illustrated and discussed in (Donadon, et al. 2008) (Falzon and Apruzzese 2011) (Falzon and Apruzzese 2011) and are based on the following assumptions: 1) the damage process is smeared over the finite element dimension; 2) internal damage variables d_{ij}, assembled in a damage matrix D, are introduced to quantify damage extent and stiffness degradation associated to specific fibre or matrix damage modes; 3) stress/strain based initiation criteria and fracture energy based evolution laws are defined for each specific failure mode.

Each of the damage parameters d_{ij} affects a different component of the fictitious undamaged stress tensor $\bar{\sigma}$ (effective stress tensor), which can be related to the true stress tensor σ through the damage matrix D as:

$$\sigma = D\bar{\sigma} = DE\varepsilon \qquad \textbf{Eq. 5-11}$$

where E denotes the undamaged material stiffness matrix and can be expressed as follows:

$$E = \frac{1}{\Omega}\begin{bmatrix} E_{11}(1-\nu_{23}\nu_{32}) & E_{22}(\nu_{12}-\nu_{32}\nu_{13}) & E_{33}(\nu_{13}-\nu_{12}\nu_{23}) & 0 & 0 & 0 \\ E_{11}(\nu_{21}-\nu_{31}\nu_{23}) & E_{22}(1-\nu_{13}\nu_{31}) & E_{33}(\nu_{23}-\nu_{21}\nu_{13}) & 0 & 0 & 0 \\ E_{11}(\nu_{31}-\nu_{21}\nu_{32}) & E_{22}(\nu_{32}-\nu_{12}\nu_{31}) & E_{33}(1-\nu_{12}\nu_{21}) & 0 & 0 & 0 \\ 0 & 0 & 0 & \Omega G_{23} & 0 & 0 \\ 0 & 0 & 0 & 0 & \Omega G_{13} & 0 \\ 0 & 0 & 0 & 0 & 0 & \Omega G_{12} \end{bmatrix}$$

$$\Omega = 1-\nu_{12}\nu_{21}-\nu_{23}\nu_{32}-\nu_{31}\nu_{13}-2\nu_{21}\nu_{32}\nu_{13}$$

The expression of the damage matrix D is:

$$D = \begin{bmatrix} (1-d_{11}) & 0 & 0 & 0 & 0 & 0 \\ 0 & (1-d_{22}^{t}) & 0 & 0 & 0 & 0 \\ 0 & 0 & 1 & 0 & 0 & 0 \\ 0 & 0 & 0 & (1-d_{23}) & 0 & 0 \\ 0 & 0 & 0 & 0 & (1-d_{13}) & 0 \\ 0 & 0 & 0 & 0 & 0 & (1-d_{12}) \end{bmatrix}$$

The equations pertaining to the constitutive matrix can be derived based on a total strain formulation or an incremental strain formulation.

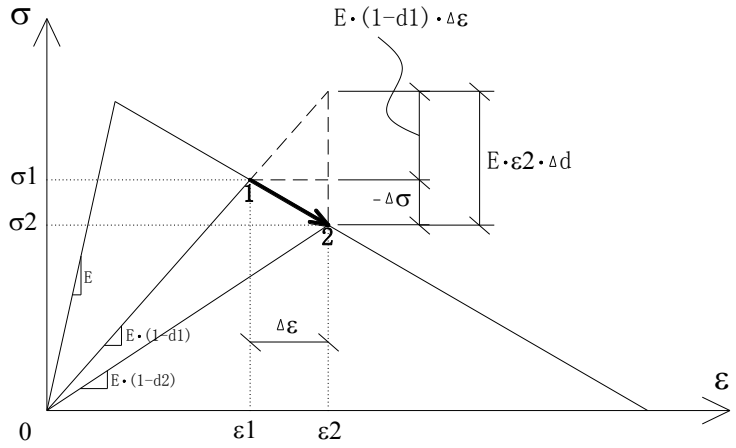

Figure 5-10: Explicit incremental strain formulation. (the item 1 means beginning of the time step, while the item 2 means end of the time step)

Based on the hypotheses of strain equivalence and after elastic-plastic strain decomposition into elastic and inelastic components, the explicit incremental stress-strain equation can be expressed as (illustrated in **Figure 5-10**):

$$\Delta\sigma = E[D\{\Delta\varepsilon - \Delta\varepsilon^{in}\} - \Delta D\{\varepsilon - \varepsilon^{in}\}] \qquad \textbf{Eq. 5-12}$$

where $\Delta\sigma$ is the incremental stress vector, $\Delta\varepsilon$ is the incremental strain vector, which can be decomposed into elastic ($\Delta\varepsilon^{el}$) and inelastic ($\Delta\varepsilon^{in}$) components, and ΔD is the incremental damage matrix; or in form of:

$$\begin{bmatrix}\Delta\sigma_{11}\\ \Delta\sigma_{22}\\ \Delta\sigma_{33}\\ \Delta\sigma_{23}\\ \Delta\sigma_{13}\\ \Delta\sigma_{12}\end{bmatrix} = \begin{bmatrix} C_{11} & C_{12} & C_{13} & 0 & 0 & 0\\ C_{21} & C_{22} & C_{23} & 0 & 0 & 0\\ C_{31} & C_{32} & C_{33} & 0 & 0 & 0\\ 0 & 0 & 0 & G_{23} & 0 & 0\\ 0 & 0 & 0 & 0 & G_{13} & 0\\ 0 & 0 & 0 & 0 & 0 & G_{12}\end{bmatrix} \left\{ \begin{bmatrix} 1-d1_{11} & 0 & 0 & 0 & 0 & 0\\ 0 & 1-d1_{22}^{t} & 0 & 0 & 0 & 0\\ 0 & 0 & 1 & 0 & 0 & 0\\ 0 & 0 & 0 & 1-d1_{23} & 0 & 0\\ 0 & 0 & 0 & 0 & 1-d1_{13} & 0\\ 0 & 0 & 0 & 0 & 0 & 1-d1_{12}\end{bmatrix} \begin{bmatrix}\Delta\varepsilon_{11}\\ \Delta\varepsilon_{22}\\ \Delta\varepsilon_{33}\\ \Delta\varepsilon_{23}\\ \Delta\varepsilon_{13}\\ \Delta\varepsilon_{12}\end{bmatrix} - \begin{bmatrix} \Delta d_{11} & 0 & 0 & 0 & 0 & 0\\ 0 & \Delta d_{22}^{t} & 0 & 0 & 0 & 0\\ 0 & 0 & 0 & 0 & 0 & 0\\ 0 & 0 & 0 & \Delta d_{23} & 0 & 0\\ 0 & 0 & 0 & 0 & \Delta d_{13} & 0\\ 0 & 0 & 0 & 0 & 0 & \Delta d_{12}\end{bmatrix} \begin{bmatrix}\varepsilon 2_{11}\\ \varepsilon 2_{22}\\ \varepsilon 2_{33}\\ \varepsilon 2_{23}\\ \varepsilon 2_{13}\\ \varepsilon 2_{12}\end{bmatrix} \right\}$$

$$= \begin{bmatrix} C_{11}[(1-d1_{11})\Delta\varepsilon_{11} - \Delta d_{11}\varepsilon 2_{11}] + C_{12}[(1-d1_{22}^{t})\Delta\varepsilon_{22} - \Delta d_{22}^{t}\varepsilon 2_{22}] + C_{13}\Delta\varepsilon_{33}\\ C_{21}[(1-d1_{11})\Delta\varepsilon_{11} - \Delta d_{11}\varepsilon 2_{11}] + C_{22}[(1-d1_{22}^{t})\Delta\varepsilon_{22} - \Delta d_{22}^{t}\varepsilon 2_{22}] + C_{23}\Delta\varepsilon_{33}\\ C_{31}[(1-d1_{11})\Delta\varepsilon_{11} - \Delta d_{11}\varepsilon 2_{11}] + C_{32}[(1-d1_{22}^{t})\Delta\varepsilon_{22} - \Delta d_{22}^{t}\varepsilon 2_{22}] + C_{33}\Delta\varepsilon_{33}\\ G_{23}[(1-d1_{23})\Delta\varepsilon_{23} - \Delta d_{23}\varepsilon 2_{23}]\\ G_{13}[(1-d1_{13})\Delta\varepsilon_{13} - \Delta d_{13}\varepsilon 2_{13}]\\ G_{12}[(1-d1_{12})\Delta\varepsilon_{12} - \Delta d_{12}\varepsilon 2_{12}]\end{bmatrix}$$

where

$$C_{11} = \frac{1}{\Omega}E_{11}(1-\nu_{23}\nu_{32}) = \frac{1}{\Omega}E_{11}[1-\nu_{23}^{0}\nu_{32}^{0}(1-d_{22}^{t})]$$

$$C_{22} = \frac{1}{\Omega}E_{22}(1-\nu_{13}\nu_{31}) = \frac{1}{\Omega}E_{22}[1-\nu_{13}^{0}\nu_{31}^{0}(1-d_{11})]$$

$$C_{33} = \frac{1}{\Omega}E_{33}(1-\nu_{12}\nu_{21}) = \frac{1}{\Omega}E_{33}[1-\nu_{12}^{0}\nu_{21}^{0}(1-d_{11})(1-d_{22}^{t})]$$

$$C_{12} = \frac{1}{\Omega}E_{22}(\nu_{12}-\nu_{32}\nu_{13}) = \frac{1}{\Omega}E_{22}(1-d_{11})[\nu_{12}^{0}-\nu_{32}^{0}\nu_{13}^{0}]$$

$$C_{13} = \frac{1}{\Omega}E_{33}(\nu_{13}-\nu_{12}\nu_{23}) = \frac{1}{\Omega}E_{33}(1-d_{11})[\nu_{13}^{0}-\nu_{12}^{0}\nu_{23}^{0}(1-d_{22}^{t})]$$

$$C_{21} = \frac{1}{\Omega}E_{11}(\nu_{21}-\nu_{31}\nu_{23}) = \frac{1}{\Omega}E_{11}(1-d_{22}^{t})[\nu_{21}^{0}-\nu_{31}^{0}\nu_{23}^{0}]$$

$$C_{23} = \frac{1}{\Omega}E_{33}(\nu_{23}-\nu_{21}\nu_{13}) = \frac{1}{\Omega}E_{33}(1-d_{22}^{t})[\nu_{23}^{0}-\nu_{21}^{0}\nu_{13}^{0}(1-d_{11})]$$

$$C_{31} = \frac{1}{\Omega}E_{11}(\nu_{31}-\nu_{21}\nu_{32}) = \frac{1}{\Omega}E_{11}[\nu_{31}^{0}-\nu_{21}^{0}\nu_{32}^{0}(1-d_{22}^{t})]$$

$$C_{32} = \frac{1}{\Omega}E_{22}(\nu_{32}-\nu_{12}\nu_{31}) = \frac{1}{\Omega}E_{22}[\nu_{32}^{0}-\nu_{12}^{0}\nu_{31}^{0}(1-d_{11})]$$

The stress-strain equation in total strain formulation (illustrated in **Figure 5-11**) can be expressed as:

$$\sigma = ED\varepsilon \qquad \textbf{Eq. 5-13}$$

or in form of:

$$\begin{bmatrix}\sigma_{11}\\ \sigma_{22}\\ \sigma_{33}\\ \sigma_{23}\\ \sigma_{13}\\ \sigma_{12}\end{bmatrix} = \begin{bmatrix} C_{11} & C_{12} & C_{13} & 0 & 0 & 0\\ C_{21} & C_{22} & C_{23} & 0 & 0 & 0\\ C_{31} & C_{32} & C_{33} & 0 & 0 & 0\\ 0 & 0 & 0 & G_{23} & 0 & 0\\ 0 & 0 & 0 & 0 & G_{13} & 0\\ 0 & 0 & 0 & 0 & 0 & G_{12}\end{bmatrix}\begin{bmatrix} 1-d_{11} & 0 & 0 & 0 & 0 & 0\\ 0 & 1-d_{22}^{t} & 0 & 0 & 0 & 0\\ 0 & 0 & 1 & 0 & 0 & 0\\ 0 & 0 & 0 & 1-d_{23} & 0 & 0\\ 0 & 0 & 0 & 0 & 1-d_{13} & 0\\ 0 & 0 & 0 & 0 & 0 & 1-d_{12}\end{bmatrix}\begin{bmatrix}\varepsilon_{11}\\ \varepsilon_{22}\\ \varepsilon_{33}\\ \varepsilon_{23}\\ \varepsilon_{13}\\ \varepsilon_{12}\end{bmatrix}$$

$$= \begin{bmatrix} C_{11}(1-d_{11})\varepsilon_{11} + C_{12}(1-d_{22}^{t})\varepsilon_{22} + C_{13}\varepsilon_{33}\\ C_{21}(1-d_{11})\varepsilon_{11} + C_{22}(1-d_{22}^{t})\varepsilon_{22} + C_{23}\varepsilon_{33}\\ C_{31}(1-d_{11})\varepsilon_{11} + C_{32}(1-d_{22}^{t})\varepsilon_{22} + C_{33}\varepsilon_{33}\\ G_{23}(1-d_{23})\varepsilon_{23}\\ G_{13}(1-d_{13})\varepsilon_{13}\\ G_{12}(1-d_{12})\varepsilon_{12}\end{bmatrix}$$

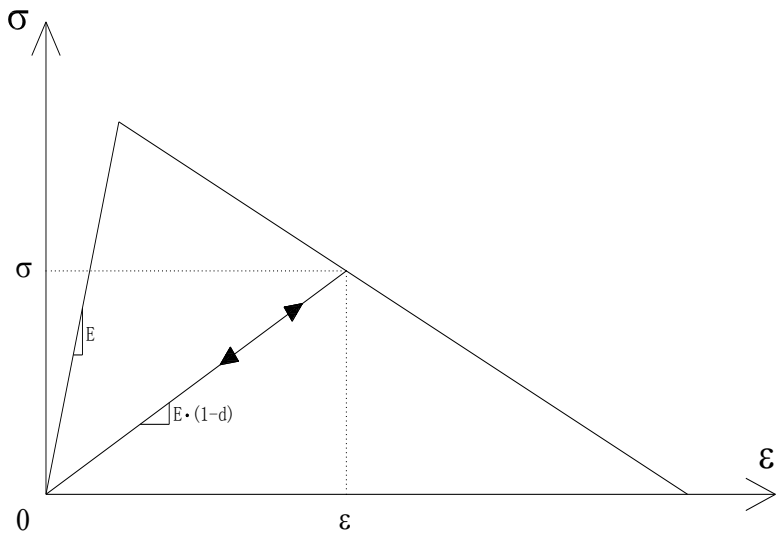

Figure 5-11: Explicit total strain formulation.

Generally speaking, the total strain formulation is intended for history-independent problems, where the current state of the problem depends only on the total strains. The incremental formulation is intended for history-dependent problems, where the current state of the problem depends on the state at the beginning of the increment and the incremental strains.

To maintain a positive definite constitutive law, the Poisson's ratio is reduced in a similar manner to the Young's modulus:

$$\frac{\nu_{ij}(1-d_{ii})}{E_{ii}(1-d_{ii})} = \frac{\nu_{ji}(1-d_{jj})}{E_{jj}(1-d_{jj})} \qquad \textbf{Eq. 5-14}$$

5.3.3 Failure Criteria

In the developed damage model, five intralaminar failure modes are taken into account: tensile fibre failure, compressive fibre failure, tensile matrix failure, compressive matrix failure and nonlinear shear failure.

- Tensile Fibre Failure

The criteria used for simulating the damage initiation and evolution of tensile fibre failure are:

$$F_{11}^{t}(\varepsilon_{11}) = (\frac{\varepsilon_{11}}{\varepsilon_{11}^{0t}})^2 - 1 \geq 0 \qquad \textbf{Eq. 5-15}$$

$$d_{11}^{t}(\varepsilon_{11}) = \frac{\varepsilon_{11}^{ft}(\varepsilon_{11} - \varepsilon_{11}^{0t})}{\varepsilon_{11}(\varepsilon_{11}^{ft} - \varepsilon_{11}^{0t})} \qquad \textbf{Eq. 5-16}$$

- Compressive Fibre Failure

The criteria used for simulating the damage initiation and evolution of compressive fibre failure are:

$$F_{11}^{c}(\varepsilon_{11}) = (\frac{\varepsilon_{11}}{\varepsilon_{11}^{0c}})^2 - 1 \geq 0 \qquad \textbf{Eq. 5-17}$$

$$d_{11}^{c}(\varepsilon_{11}) = \frac{\varepsilon_{11}^{fc}(\varepsilon_{11} - \varepsilon_{11}^{0c})}{\varepsilon_{11}(\varepsilon_{11}^{fc} - \varepsilon_{11}^{0c})} \qquad \textbf{Eq. 5-18}$$

In order to introduce the effect of fragment interaction under compression within the damaged region, a minimum residual value, assumed equal to the matrix compressive strength as shown in **Figure 5-12**, was considered for the normal compressive stress along the fibre direction (Donadon, et al. 2008).

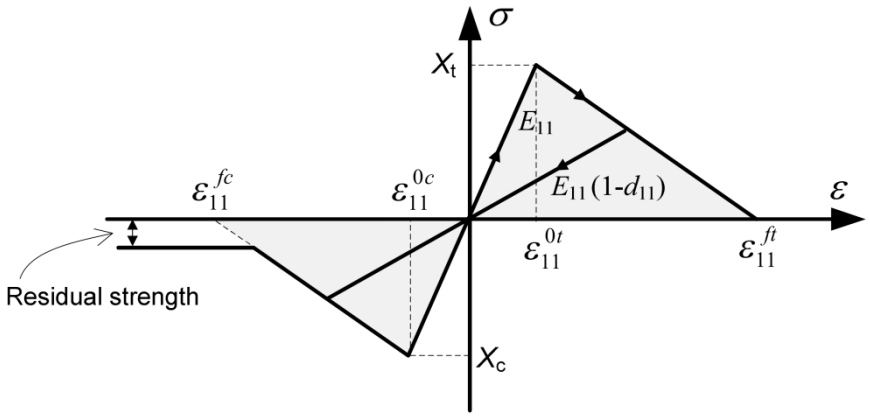

Figure 5-12: Model behavior for fibre failure.

- Tensile Matrix Failure

Damage initiation and evolution for tensile matrix cracking were defined using the following failure criteria:

$$F_{22}^{t}(\varepsilon_{22}) = (\frac{\varepsilon_{22}}{\varepsilon_{22}^{0t}})^2 - 1 \geq 0$$

$$d_{22}^{t}(\varepsilon_{22}) = \frac{\varepsilon_{22}^{ft}(\varepsilon_{22} - \varepsilon_{22}^{0t})}{\varepsilon_{22}(\varepsilon_{22}^{ft} - \varepsilon_{22}^{0t})} \qquad \textbf{Eq. 5-19}$$

- Compressive Matrix Failure

Experiments show that unidirectional laminates under transverse compressive loads fail by shear (Puck and Schürmann 1998) (Puck and Schürmann 2002), with a fracture plane oriented at $\theta_f = 53° \pm 2°$ from the laminate plane (Donadon, et al. 2008). To correctly describe this phenomenon, the candidate criteria should thus evaluate the stress/strain state in the angled fracture plane instead of the nominal coordinate plane with the angle of $\theta_f = 0°$.

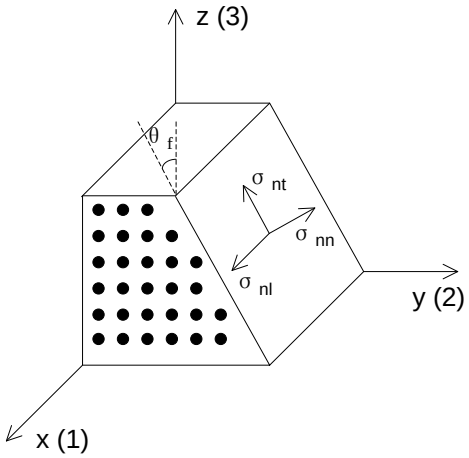

Figure 5-13: Compressive matrix failure and fracture plane. (Donadon, et al. 2008)

For a general fracture plane l-n-t with fracture angle θ_f, as shown in **Figure 5-13**, the stresses can be obtained through transformation from laminae coordinate system 1-2-3 or x-y-z:

$$\begin{cases} \sigma_{nn} = \sigma_y \cos^2\theta_f + \sigma_z \sin^2\theta_f + 2\tau_{yz}\cos\theta_f \sin\theta_f \\ \tau_{nl} = \tau_{xy}\cos\theta_f + \tau_{zx}\sin\theta_f \\ \tau_{nt} = (\sigma_z - \sigma_y)\cos\theta_f \sin\theta_f + \tau_{yz}(\cos^2\theta_f - \sin^2\theta_f) \end{cases} \quad \textbf{Eq. 5-20}$$

The damage model for simulating transverse failure under compression follows the criterion proposed by Puck and Schurmann (1998) (2002), who extended the failure

criterion originally proposed by Hashin with two main modifications: 1) to judge the failure occurrence, the tractions at the fracture plane $\sigma_{nn}, \sigma_{nl}, \sigma_{nt}$ should not be compared with the nominal measured strengths from conventional mechanical tests, but with strengths corresponding to the fracture plane; 2) the normal compressive stress at the fracture plane does not induce the failure directly, while contributing to the increase of shear strength. To do so, the criterion based on the Mohr–Coulomb theory, which is schematically shown in **Figure 5-14**, is used to define the damage initiation:

$$F_{22}^{C}(\sigma_{nn}, \sigma_{nl}, \sigma_{nt}) = \left(\frac{\tau_{nt}}{S_{23}^{A} - \mu_{nt}\sigma_{nn}}\right)^2 + \left(\frac{\tau_{nl}}{S_{12} - \mu_{nl}\sigma_{nn}}\right)^2 \geq 1 \qquad \textbf{Eq. 5-21}$$

where S_{12} is the longitudinal shear strength; S_{23}^{A} is the transverse shear strength in the potential fracture plane; μ_{nt} and μ_{nl} are friction coefficients in the transverse and longitudinal directions. These parameters are related to the fracture angle:

$$\emptyset = 2\theta_f - 90°$$

$$S_{23}^{A} = \frac{Y_C(1 - \sin\emptyset)}{2\cos\emptyset}$$

$$\mu_{nt} = \tan\emptyset$$

$$\mu_{nl} = \mu_{nt} \cdot S_{12}/S_{23}^{A}$$

where Y_C is the standard transverse compressive strength.

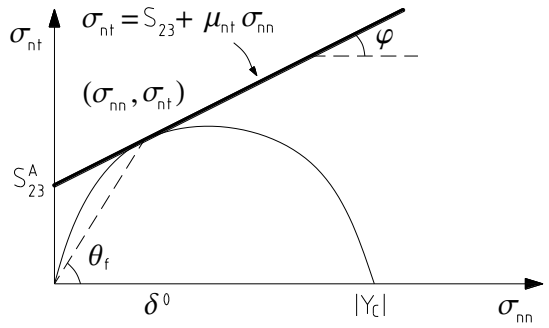

Figure 5-14: The criterion used to predict damage initiation of transverse compression.

After the damage initiation criterion, **Eq. 5-21**, is met, it's reasonable to assume damage growth as a function of total local shear strain:

$$d_{22}^{c}(\gamma_{nt},\gamma_{nl}) = \frac{\gamma^{max}(\gamma-\gamma^{f})}{\gamma(\gamma^{max}-\gamma^{f})} \qquad \textbf{Eq. 5-22}$$

$$\gamma = \sqrt{\gamma_{\mathrm{nt}}^{2}+\gamma_{\mathrm{nl}}^{2}}$$

where γ^{f} is the resultant onset shear strain $\gamma^{f} = \gamma(F_{22}^{C} = 1.0)$; γ^{max} is the shear strain corresponding to the total damage under transverse compression.

- Nonlinear Shear Failure

Experimental evidence indicates that composite materials exhibit a nonlinear and irreversible behaviour under shear loading. As an example, **Figure 5-15** shows the experimental shear response of the prepreg material used in the facesheets of the sandwich panels as obtained by tensile cyclic loading tests on [+45/-45]s laminates.

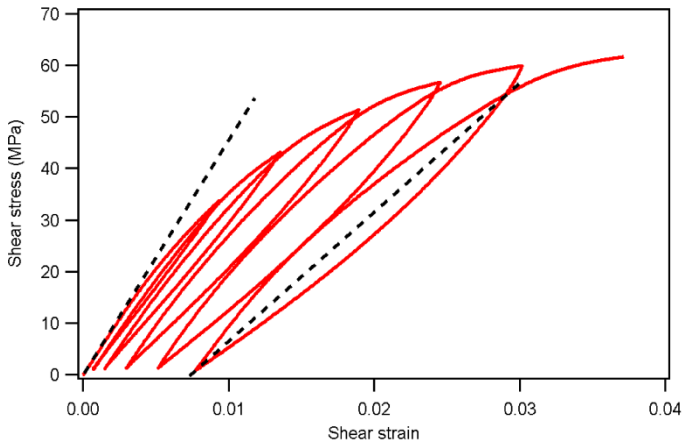

Figure 5-15: Shear stress-strain response of HS300/ET223 prepreg as obtained by tensile cyclic testing on a $[+45/-45]_S$ laminate.

The total shear strain can be decomposed into elastic and damage strain:

$$\gamma_{ij} = \gamma_{ij}^{e} + \gamma_{ij}^{d} \quad i,j = 1,2,3 \quad i \neq j \qquad \textbf{Eq. 5-23}$$

where the nonlinear response may be attributed to a combination of plastic deformation and progressive stiffness reduction due to micro-damage.

The nonlinear shear behaviour was introduced in the FE model through a cubic polynomial stress-strain curve:

$$\tau_{ij}(\gamma_{ij}) = c_1\gamma_{ij} + c_2\gamma_{ij}^2 + c_3\gamma_{ij}^3 \qquad \textbf{Eq. 5-24}$$

where c_1, c_2 and c_3 are coefficients determined by fitting the polynomial to the experimentally obtained shear stress-strain data.

The proposed shear damage model is characterized by two distinct stages, as illustrated in **Figure 5-16**. The first phase characterizes to the nonlinear behaviour associated to matrix micro-cracking; in this region, the damage parameter is defined as:

$$d_{ij}(\gamma_{ij}) = \alpha\gamma_{ij} \quad \gamma_{ij} \leq \gamma_{ij}^{max} \qquad \textbf{Eq. 5-25}$$

where α is a material constant, determined experimentally by cyclic loading unloading tests, which represents the gradual shear modulus reduction with increasing strain (**Figure 5-17**). The second phase simulates the post-failure response of the material, which is described by a linear softening law, expressed by the following equation:

$$d_{ij}(\gamma_{ij}) = \alpha\gamma_{ij}^{max} + \frac{\left(\gamma_{ij}^{f} - \gamma_{ij}^{0}\right)\left(\gamma_{ij} - \gamma_{ij}^{max}\right)}{\left(\gamma_{ij} - \gamma_{ij}^{0}\right)\left(\gamma_{ij}^{f} - \gamma_{ij}^{max}\right)} - \alpha\gamma_{ij}^{max}\frac{\left(\gamma_{ij}^{f} - \gamma_{ij}^{0}\right)\left(\gamma_{ij} - \gamma_{ij}^{max}\right)}{\left(\gamma_{ij} - \gamma_{ij}^{0}\right)\left(\gamma_{ij}^{f} - \gamma_{ij}^{max}\right)} \quad \gamma_{ij} > \gamma_{ij}^{max} \qquad \textbf{Eq. 5-26}$$

$$\gamma_{ij}^{0} = \gamma_{ij}^{max} - \frac{\tau_{ij}(\gamma_{ij}^{max})}{(1 - \alpha\gamma_{ij}^{max})E_{ij}}$$

where $E_{ij} = c_1$ is the initial shear modulus, and the final shear strain γ_{ij}^{f} corresponds to the end of the failure process.

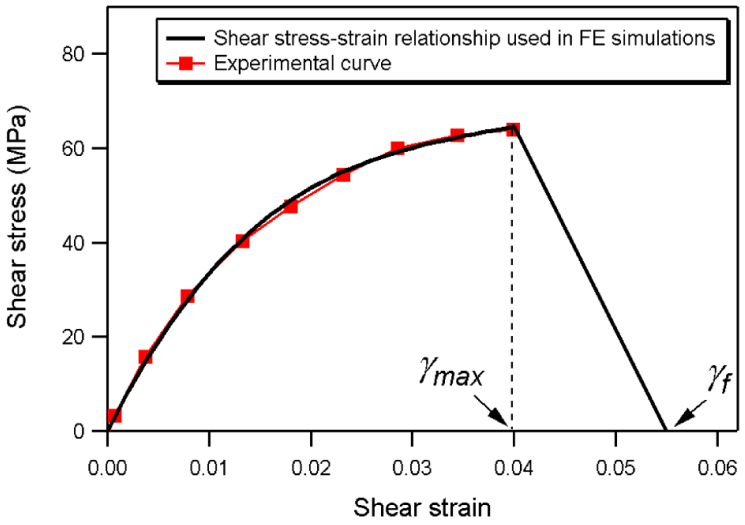

Figure 5-16: Model behaviour of shear stress-shear strain response implemented in the FE model.

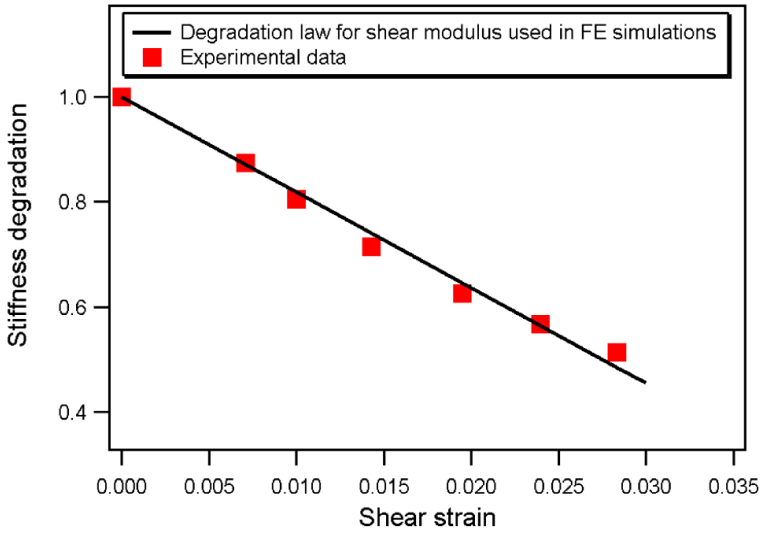

Figure 5-17: Reduction of shear stiffness with increasing strain implemented in the FE model.

5.3.4 Implementation

The intralaminar failure models were implemented into FE package ABAQUS/ Explicit through a user-defined VUMAT subroutine, as shown in **Figure 5-18**.

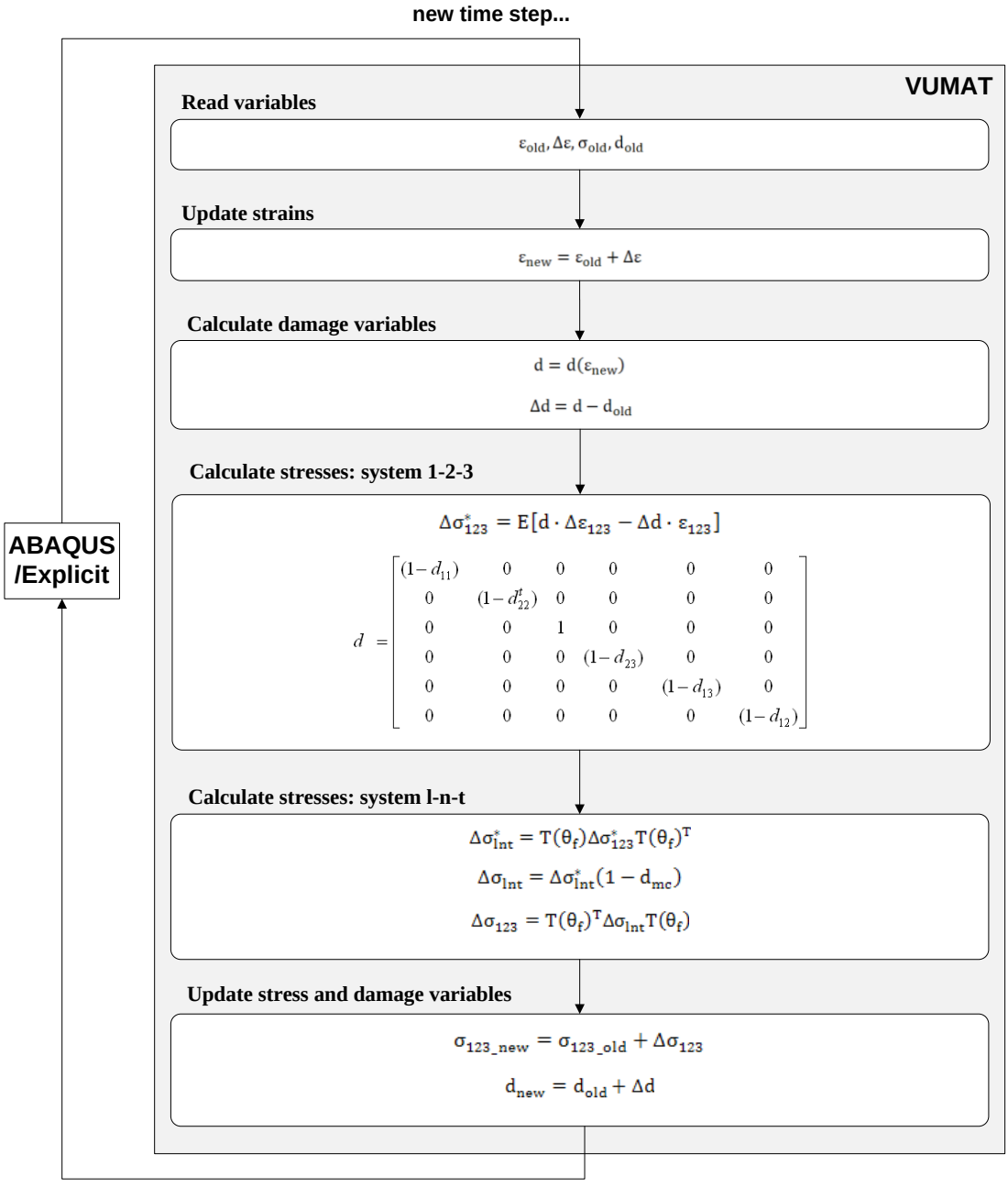

Figure 5-18: Flow diagram of VUMAT subroutine for intralminar failure models.

A smeared formulation is used in this study to avoid strain localization. In smeared formulations, the fracture energy is distributed (smeared) over the full volume of the element.

One of the major difficulties related with the smeared formulation approach is that the material damage laws have to include a length parameter, in order to achieve a constant energy released per unit area of crack generated regardless of the element dimensions. Characteristic element lengths specific to the various simulated failure mechanisms were introduced in the study to solve this problem.

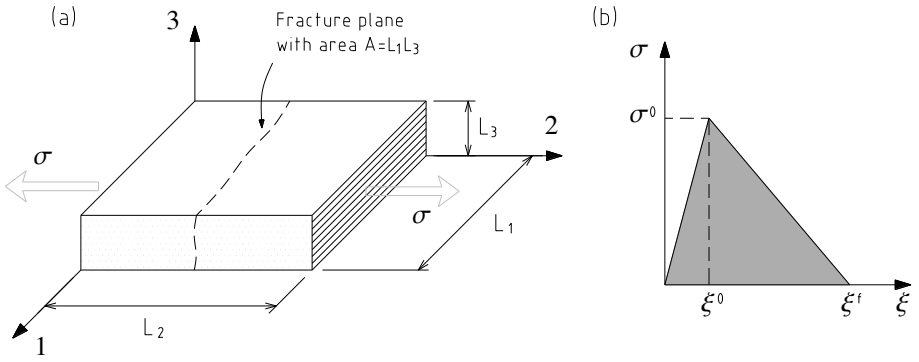

Figure 5-19: Element loaded in tension to failure (a); material law with failure (b).

If we consider a single element subject to matrix tensile fracture as an example, as shown in **Figure 5-19**, it can be easily understood how the length parameter enters the material law. The energy absorption during the process of failure can be easily obtained:

$$U = V \cdot g_f = L_1 L_2 L_3 . \frac{1}{2} \sigma_0 \varepsilon_f \qquad \textbf{Eq. 5-27}$$

The fracture energy (or energy dissipated per unit area) can be written as:

$$G_f = \frac{U}{A_f} = \frac{V}{A_f} \cdot g_f = L_2 \cdot \frac{1}{2} \sigma_0 \varepsilon_f \qquad \textbf{Eq. 5-28}$$

Here the parameter L_2, the element size perpendicular to the fracture plane, is actually what we call *Characteristic Length*, which relates the three-dimensional parameter g_f (unit:J/m^3) with the two-dimensional parameter G_f (unit:J/m^2). From **Eq. 5-28**, one can easily retrieve:

$$\varepsilon_f = \frac{2G_f}{\sigma_0 L_2} \qquad \textbf{Eq. 5-29}$$

So, if strain values ε_f that mark the end of the failure process are defined by **Eq. 5-29**, the energy absorbed by the plate will be independent of the mesh density.

The characteristic element lengths for the various failure modes were selected according to the procedure outlined in (Pinho, Iannucci and Robinson 2006), as illustrated in **Figure 5-20**.

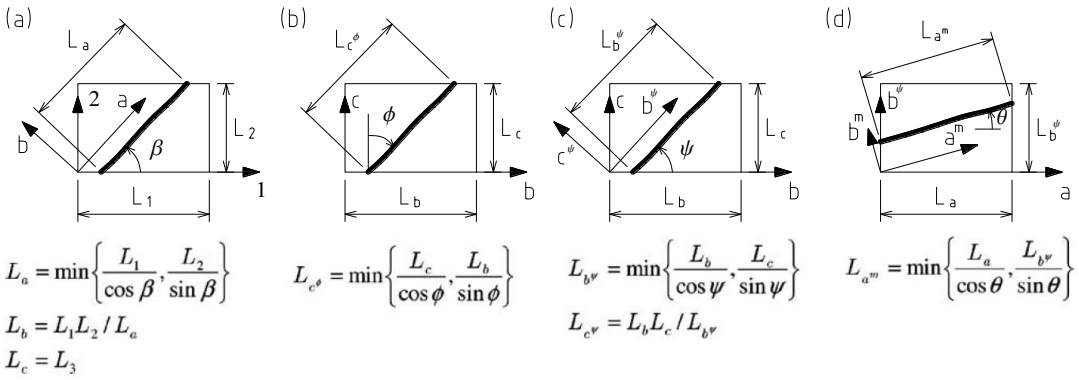

Figure 5-20: Determination of the characteristic length within an element. (Pinho, Iannucci and Robinson 2006)

5.3.5 Model Testing

Before being applied to simulate impact on composite sandwich panels, the user-written subroutine VUMAT was tested with simple FE models in which cases the theoretical solutions could be easily derived. Let us consider fibre tensile failure mode as

an example to show the test results. **Figure 5-21** shows the basic information of the simple composite coupon (20 mm long, 10 mm wide and 2 mm thick) which is subject to tensile loading along the fibre orientation. In order to evaluate the mesh sensitivity of the failure model, the virtual coupon was discretized with three different mesh densities as shown in **Figure 5-22**.

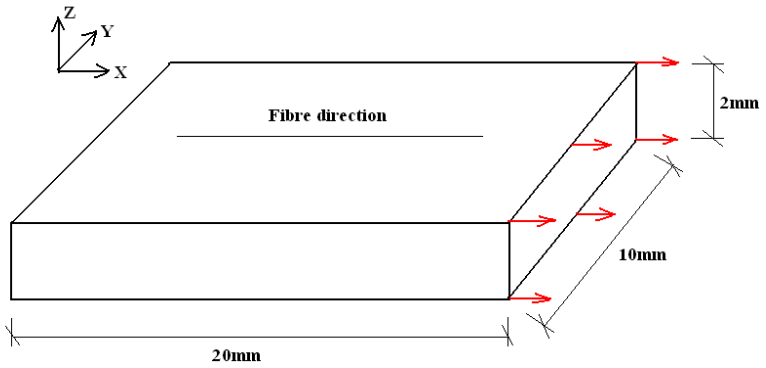

Figure 5-21: Simple composite coupon test.

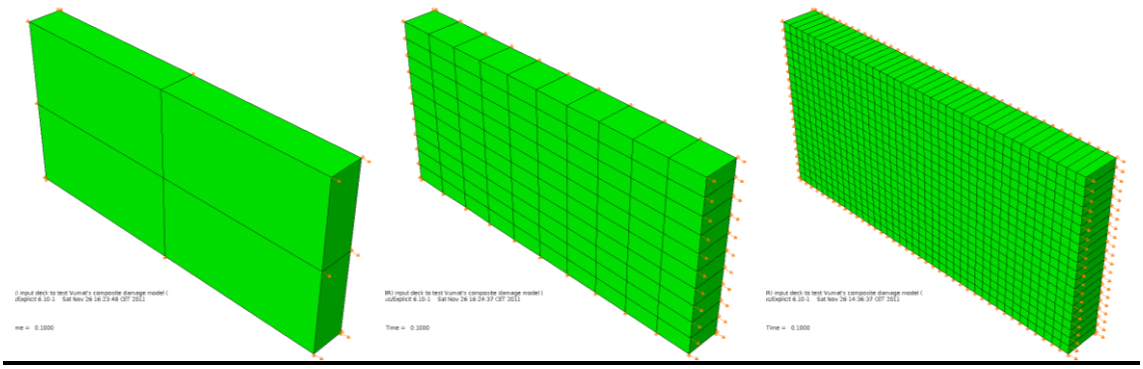

Mesh I	Mesh II	Mesh III
10mm×5mm×2mm	2mm×1mm×2mm	0.5mm×0.5mm×2mm

Figure 5-22: Models discretized with different element sizes for the mesh sensitivity study.

Figure 5-23 depicts the failure plots for different meshes. **Figure 5-24** shows the structural responses (force-displacement curves) with different mesh types. According to **Figure 5-24**, the energy dissipated in the formation of damage is mesh-insensitive.

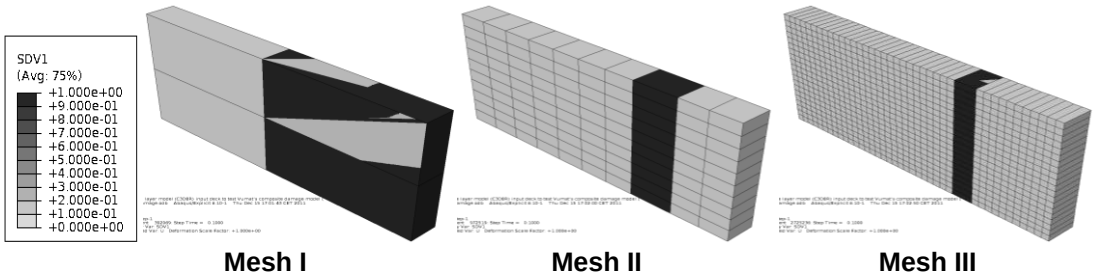

Figure 5-23: Failure localization for different mesh types.

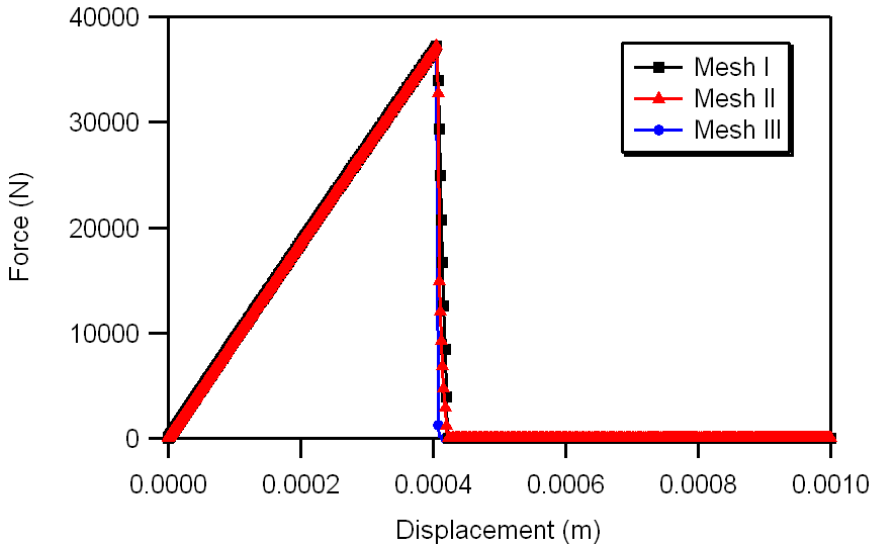

Figure 5-24: Structural responses with different mesh densities.

The stress-strain curves of damaged elements with different mesh densities are plotted in **Figure 5-25**. The key strain values corresponding to damage initiation ε^0 and total damage ε^f are compared with theoretical solutions and a good agreement is observed for all mesh densities.

Analyses using incremental strain formulation and total strain formulation are also compared based on the test case. As shown in **Figure 5-26**, the results obtained using two different solutions are practically coincident.

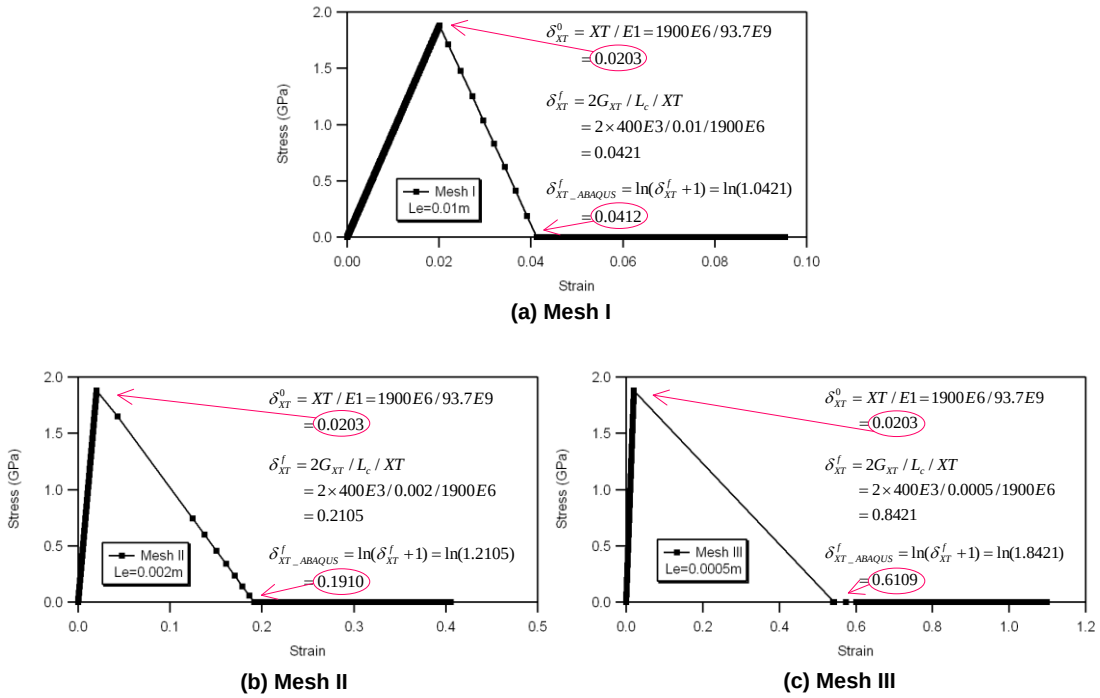

Figure 5-25: Comparison of model predicted and theoretical strains corresponding to damage initiation and total damage with different meshes.

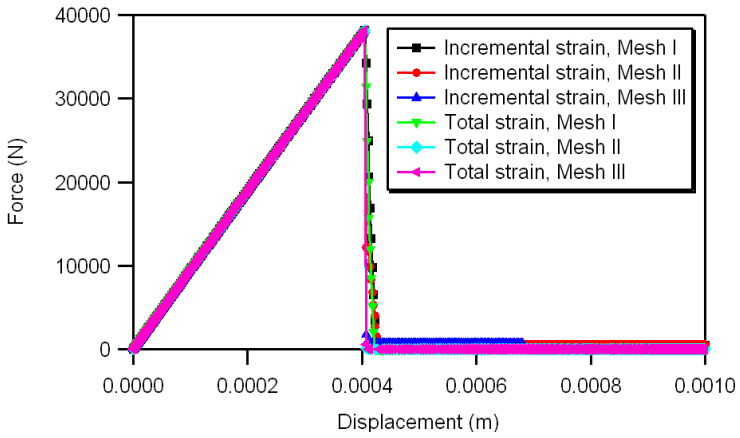

Figure 5-26: Comparison of results between incremental and total strain formulations.

Figure 5-27-**Figure 5-30** show another test example, for the non-linear shear failure mode. **Figure 5-27** illustrates a $[+45/-45]_S$ laminate specimen (20 mm long, 5mm wide and 1.2 mm thick) subjected to a loading-unloading tensile shear test. The FE model is shown in **Figure 5-28**a; the cyclic loading, with a maximum boundary displacement value of $d_{max} = 1mm$, is shown in **Figure 5-28**b.

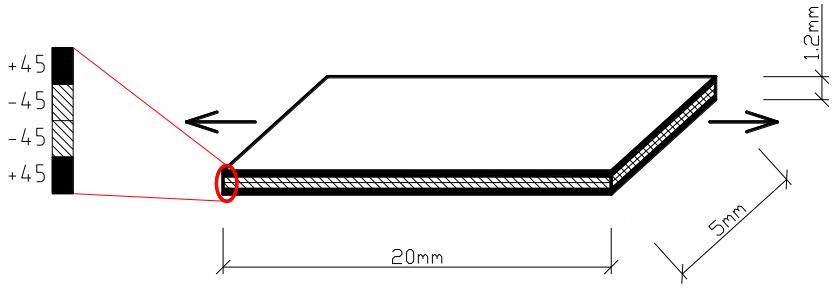

Figure 5-27: Tensile shear test on $[+45/-45]_S$ laminate.

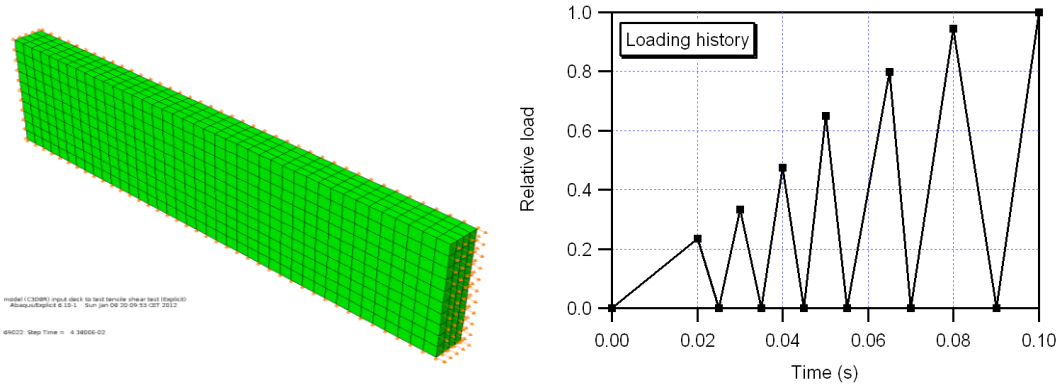

(a) (b)

Figure 5-28: FE model (a) and cyclic loading (b).

Figure 5-29 shows the predicted shear failure. The damage propagates along 45° degree from the fibre orientation, which is in accordance with experimental tests. The shear stress-shear strain curve of selected damaged element (shown as the red box in **Figure 5-29**) is presented in **Figure 5-30**, which shows that the model is able to correctly reproduce the experimental stress-strain curve.

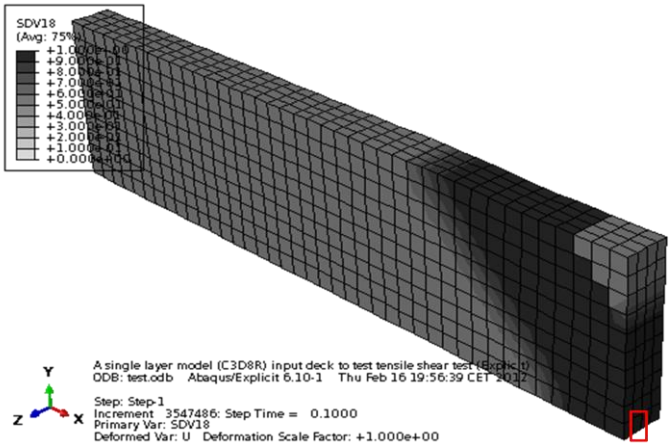

Figure 5-29: Shear failure predicted by the model.

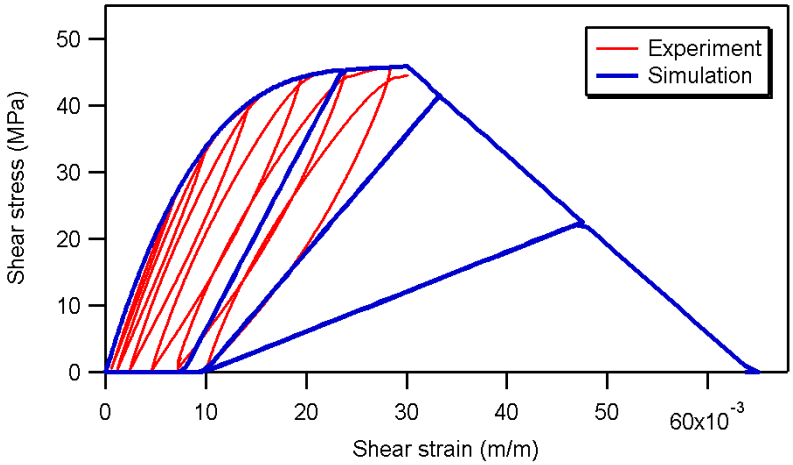

Figure 5-30: Shear stress-shear strain curve of damage element.

5.4 Foam Core Behavior Model

The crushable foam model applied to simulate the nonlinear material response of foam core is based on the model proposed by Deshpande and Fleck (Deshpande and Fleck 2000), which has been implemented in ABAQUS (Abaqus 6.10 Analysis User's manual 2010), and is used in conjunction with the linear elastic material model.

The elastic part of the response is specified as linear isotropic, and the stress-strain relationship is given by:

$$\begin{Bmatrix} \varepsilon_{11} \\ \varepsilon_{22} \\ \varepsilon_{33} \\ \gamma_{12} \\ \gamma_{13} \\ \gamma_{23} \end{Bmatrix} = \begin{bmatrix} 1/E & -\upsilon/E & -\upsilon/E & 0 & 0 & 0 \\ -\upsilon/E & 1/E & -\upsilon/E & 0 & 0 & 0 \\ -\upsilon/E & -\upsilon/E & 1/E & 0 & 0 & 0 \\ 0 & 0 & 0 & 1/G & 0 & 0 \\ 0 & 0 & 0 & 0 & 1/G & 0 \\ 0 & 0 & 0 & 0 & 0 & 1/G \end{bmatrix} \begin{Bmatrix} \sigma_{11} \\ \sigma_{22} \\ \sigma_{33} \\ \sigma_{12} \\ \sigma_{13} \\ \sigma_{23} \end{Bmatrix} \quad \textbf{Eq. 5-30}$$

For the plastic part of the behavior, the yield surface is a Mises circle in the deviatoric stress plane and an ellipse in the meridional (p–q) stress plane. Two hardening models are available: the volumetric hardening model, where the point on the yield ellipse in the meridional plane that represents hydrostatic tension loading is fixed and the evolution of the yield surface is driven by the volumetric compacting plastic strain, and the isotropic hardening model, where the yield ellipse is centered at the origin in the p–q stress plane and evolves in a geometrically self-similar manner.

The hardening curve must describe the uniaxial compression yield stress as a function of the corresponding plastic strain. In defining this dependence at finite strains, "true" (Cauchy) stress and logarithmic strain values should be given. Both models predict similar behavior for compression-dominated loading. However, for hydrostatic tension loading the volumetric hardening model assumes a perfectly plastic behavior, while the

isotropic hardening model predicts the same behavior in both hydrostatic tension and hydrostatic compression.

- **Crushable foam model with volumetric hardening**

The crushable foam model with volumetric hardening uses a yield surface with an elliptical dependence of deviatoric stress on pressure stress. It assumes that the evolution of the yield surface is controlled by the volumetric compacting plastic strain experienced by the material.

The yield surface for the volumetric hardening model is defined as:

$$F = \sqrt{q^2 + \alpha^2(p - p_0)^2} - B = 0 \qquad \textbf{Eq. 5-31}$$

Where p is the pressure stress, p_0 is the center of the yield ellipse on the p-axis, q is the Mises stress, α is the shape factor of the yield ellipse that defines the relative magnitude of the axes, B is the size of the (vertical) q-axis of the yield ellipse.

The yield surface represents the Mises circle in the deviatoric stress plane and is an ellipse on the meridional stress plane, as depicted in **Figure 5-31**.

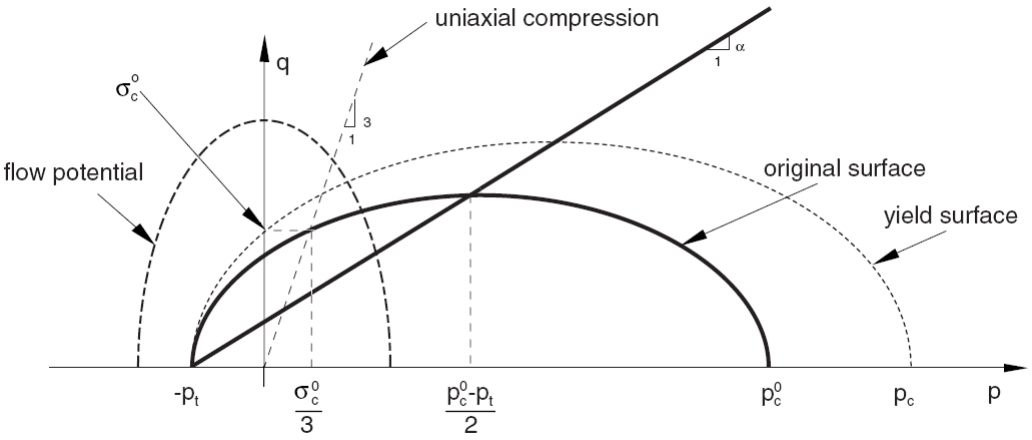

Figure 5-31: Crushable foam model with volumetric hardening: yield surface and flow potential in the p–q stress plane. (Abaqus 6.10 Analysis User's manual 2010)

The yield surface evolves in a self-similar fashion (constant α); and the shape factor can be computed using the initial yield stress in uniaxial compression, σ_c^0, the initial yield stress in hydrostatic compression, p_c^0(the initial value of p_c), and the yield strength in hydrostatic tension, p_t:

$$\alpha = \frac{3k}{\sqrt{(3k_t + k)(3 - k)}} \quad \text{with} \quad k = \frac{\sigma_c^0}{p_c^0} \quad \text{and} \quad k_t = \frac{p_t}{p_c^0}$$

For a valid yield surface the choice of strength ratios must be such that $0 < k < 3$ and $k_t \geq 0$.

- **Crushable foam model with isotropic hardening**

The isotropic hardening model uses a yield surface that is an ellipse centered at the origin in the p–q stress plane. The yield surface evolves in a self-similar manner, and the evolution is governed by the equivalent plastic strain.

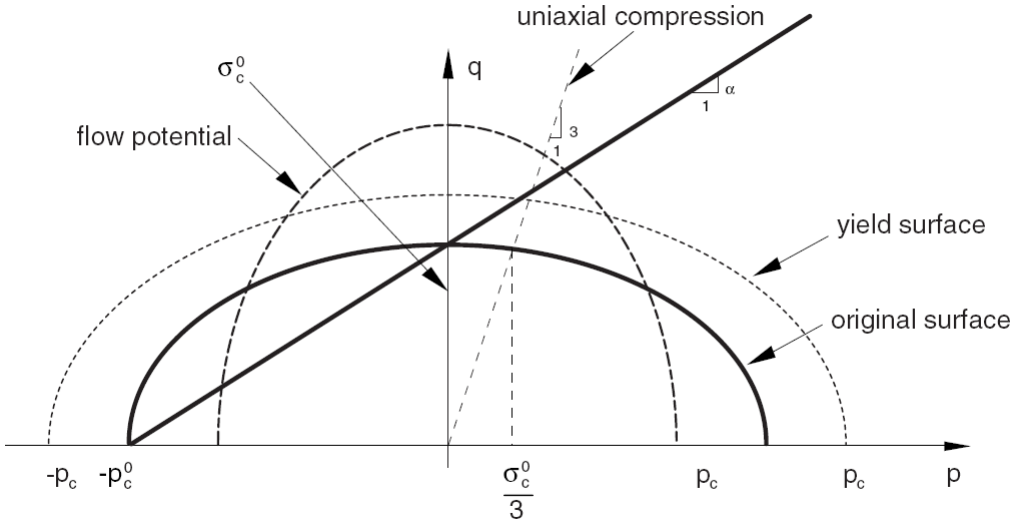

Figure 5-32: Crushable foam model with isotropic hardening: yield surface and flow potential in the p–q stress plane. (Abaqus 6.10 Analysis User's manual 2010)

The yield surface for the isotropic hardening model is defined as:

$$F = \sqrt{q^2 + \alpha^2 p^2} - B = 0 \qquad \textbf{Eq. 5-32}$$

Where p is the pressure stress, q is the Mises stress, α is the shape factor of the yield ellipse that defines the relative magnitude of the axes, B is the size of the (vertical) q-axis of the yield ellipse.

The yield surface represents the Mises circle in the deviatoric stress plane. The shape of the yield surface in the meridional stress plane is depicted in **Figure 5-32**. The shape factor, σ_c^0, can be computed using the initial yield stress in uniaxial compression, σ_c^0, and the initial yield stress in hydrostatic compression, p_c^0(the initial value of p_c), using the relation:

$$\alpha = \frac{3k}{\sqrt{9 - k^2}} \quad \text{with} \quad k = \frac{\sigma_c^0}{p_c^0}$$

The value of k must be thus provided to define the shape of the yield ellipse. For a valid yield surface the strength ratio must be such that $0 \leq k < 3$. The particular case of $k = 0$ corresponds to the Mises plasticity.

It should be noted that PVC foam core may show an increase in the yield stress as strain rates increase like many other materials. For many crushable foam materials this increase in yield stress becomes important when the strain rates are in the range of 0.1-1/s and can be very important if the strain rates are in the range of 10–100/s, as commonly occurs in high-energy dynamic events (Abaqus 6.10 Analysis User’ s manual 2010). According to the findings of previous investigations (Belingardi, Cavatorta and Duella 2003) (Akil and Cantwell 2002) (Schubel, Luo and Daniel 2005), the low-velocity impact

response of foam cored sandwich structures is not greatly affected by the loading rate (at least over a range of impact velocities comparable to that examined in this study). In contrast, other research work (Brooks, et al. 2010) (Mines, Worrall and Gibson 1998) shows some evidence of a rate-dependent behaviour of sandwich structures subjected to transverse loads, as a direct consequence of the influence of strain rate on the deformation properties of the core material.

5.5 Concluding Remarks

Cohesive zone model and progressive failure models based on continuum damage mechanics were implemented in ABAQUS/Explicit via user-defined subroutines VUMAT to model interlaminar and intralaminar failure mechanisms in laminate skins, respectively. The criteria used to define each failure mode and the implementation details were illustrated. Crushable foam model with volumetric hardening were applied to model the nonlinear behaviour of PVC foam core.

The VUMATs were firstly tested on simple FE models before being applied to simulate impact-induced damage in composites; the testing results prove that the failure models have been correctly implemented and are reliable to be used to simulate impacts on composite panels.

CHAPTER 6

NUMERICAL MODELS FOR SIMULATING IMPACTS ON SANDWICH PANELS

6.1 Finite Element Models

Full three-dimensional finite element models of the sandwich panels were constructed in ABAQUS/Explicit using solid elements for simulating the foam core and the layers of laminate skins, and cohesive elements for modelling the behaviour of the interfaces between plies and between core and facesheets (**Figure 6-1**). Both the impactor, which was simulated as a rigid hemispherical body with a 2.34 kg mass, and the supporting plate were modelled using R3D4 rigid shell elements.

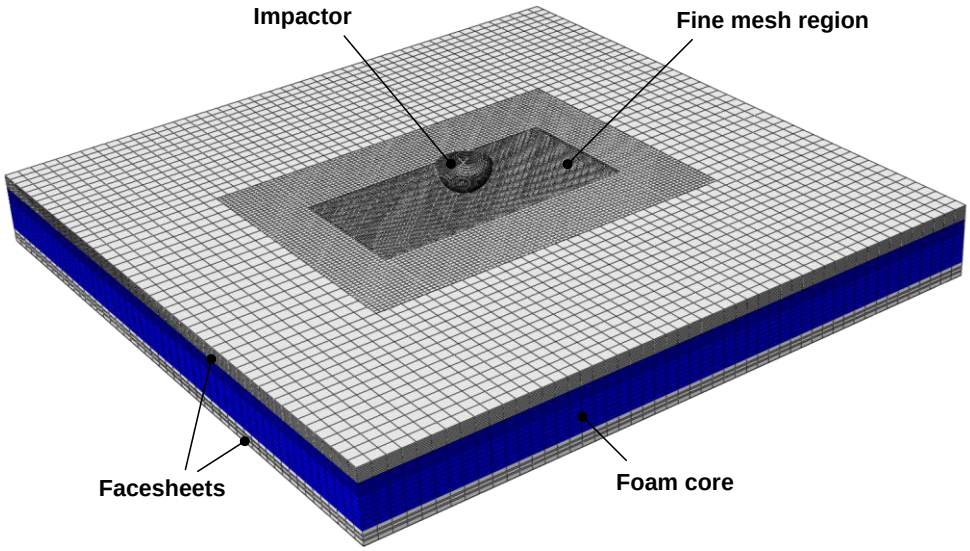

Figure 6-1: Typical FE model of impacted sandwich panels.

Elements with in-plane size of 0.5 mm by 0.5 mm were utilized in a fine mesh region (30 mm by 60 mm, as shown in **Figure 6-1**) centered at the impact location. The size of the elements was selected by a sensitivity analysis which shows convergence of results (in terms of both structural response and damage pattern and extent) for element sizes smaller than about 1 mm.

The laminated skins were modelled by C3D8R solid elements with reduced integration, using one element through the thickness of each layer. Since no damage occurs in the facesheets opposite to the impact side, the intralaminar failure models presented in Section 5.3 were implemented only in the layers of the upper (impacted) facesheet, while the composite layers on the backside of the sandwich panels were modelled as linear elastic materials.

Zero-thickness COH3D8 cohesive elements were inserted at the interfaces between layers with different fibre orientations and at the skin/core interface. The failure criteria illustrated in Section 5.2 were adopted for predicting the initiation and evolution of interlaminar delaminations.

The core was modelled using a total of 10 C3D8R solid elements through the thickness. The crushable foam model with volumetric hardening, as presented in Section 5.4, which is available in Abaqus (CRUSHABLE FOAM and CRUSHABLE FOAM HARDENING options) was used to model the inelastic behaviour of the foam. The hardening behaviour was represented in terms of uniaxial compressive stress versus plastic strain. The average stress-strain curve obtained from three compression tests was used to define the piecewise linear hardening law supplied as input data to the foam plasticity model.

The interaction between the composite plate and the indentor was simulated by surface-to-surface contact pairs, which were also applied to simulate the contact between the panel and the supporting plate. The contact constraints were enforced using a penalty contact algorithm. A friction model was included in the contact property definition in terms of a Coulomb friction model which relates the maximum allowable frictional (shear) stress across the interface to the contact pressure between the contacting bodies. A friction coefficient of μ=0.3 was adopted.

Impacts of different energies were simulated by imposing the appropriate velocities at the instant of contact to the impactor. The geometrical nonlinearity of the problem was taken into account by activating the NLGEOM option for large deformation. No mass scaling was used in the model.

A time increment Δt of about 5.0E-09s was used for the explicit integration of the equilibrium equations. This time-step satisfies the stability restriction imposed by the iterative time-stepping algorithm and was selected using the element-by-element estimation scheme available in ABAQUS/Explicit, based on the evaluation of highest element frequency in the whole FE model (Abaqus 6.10 Analysis User's manual 2010).

6.2 Material Properties

The elastic and fracture properties used in the FE model were obtained by a series of experimental tests or gathered from the literature, as discussed in Section 4.5. The values of the main properties adopted in the analyses are summarized in **Table 6-1**.

In particular, the experimental shear behaviour of the unidirectional lamina was assessed by tensile tests on $[+45/-45]_S$ laminates, and the damage parameter describing the degradation of shear stiffness under increasing loads was characterized by a sequence

of loading-unloading cycles (**Figure 6-2**). It should be noted that, because of the lack of experimental results for out-of-plane shear behaviour, the same curves and mechanical properties for in-plane shear were used to model out-of-plane shear non-linearities.

Table 6-1: Material properties used in FE analyses.

Layer properties	E_{11} = 122 GPa; E_{22} = E_{33}=6.2 GPa; ν_{12} = ν_{13} = 0.35; ν_{23}=0.5; X_t = 1850 MPa; X_c = 1470 MPa; Y_t = 27 MPa; Y_c = 140 MPa; G_{ft}= 92 kJ/m^2; G_{fc} = 80 kJ/m^2; G_{mt} = 520 J/m^2; G_{mc} = 1610 J/m^2
Interface properties	k_N = 120 GPa/mm; k_S = k_T = 43 GPa/mm; N = 27 MPa; S = T = 55 MPa; G_{IC} = 520 J/m^2; G_{IIC} = G_{IIIC} = 920 J/m^2

Figure 6-3 shows the fracture energies at the onset of delamination growth, together with the curve of the power law delamination criterion implemented in the model for interlaminar fracture. The exponents of the power law criterion were selected by fitting to the experimental data.

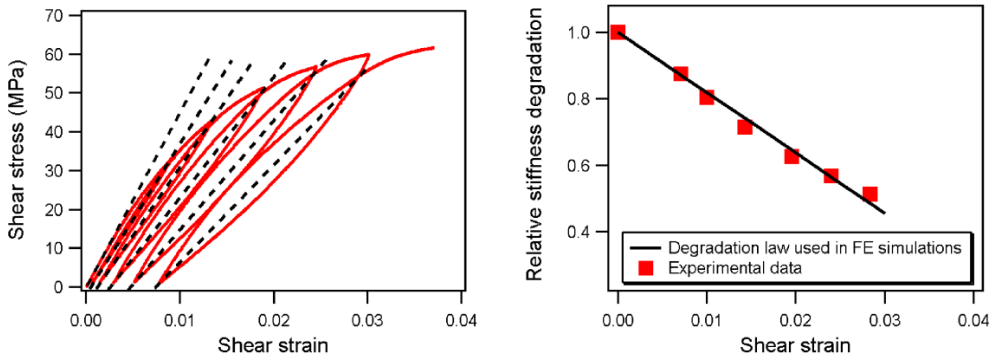

Figure 6-2: Experimental shear stress-strain behaviour under incremental cyclic loading (left) and stiffness degradation under shear loading (right).

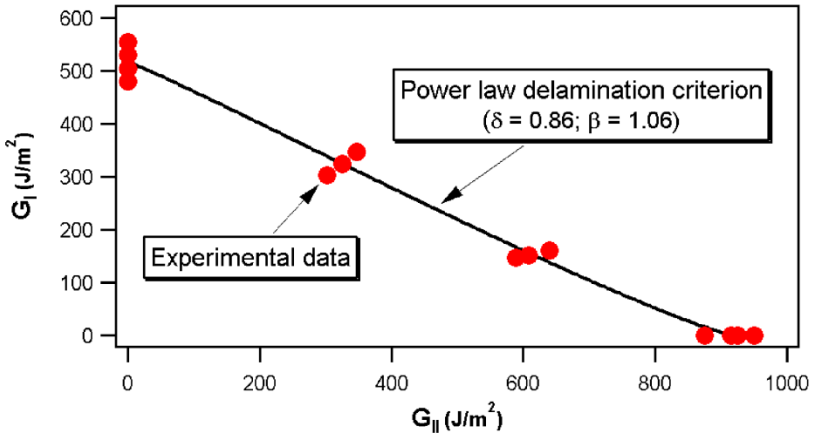

Figure 6-3: Fracture energy values at the onset of delamination propagation obtained by DCB, ENF and MMB tests and power law delamination criterion implemented in the FE model.

Because of the lack of experimental data for the HS300/ET223 prepreg system, values for fibre fracture energy evaluated for a different carbon/epoxy system in (Faggiani and Falzon 2010) were used as input to the model. Sensitivity analyses, which were specifically carried out to assess the influence of these parameters on the simulations, show that fibre fracture energy values have little influence on the predicted results over a wide range of fibre toughnesses; the indications of these analyses are not unexpected, in view of the low entity of fibre damage experimentally observed on composite skins even at highest impact energies examined in the study.

Furthermore, as the low strength of the foams precluded, in spite of various attempts, a proper experimental characterization of the fracture properties of the facesheet/foam interface, the same fracture energy values used for cohesive elements within the laminated skin were adopted to model the cohesive behaviour of the skin/core interface. It is worth noting, however, that this assumption has no influence on the quality of damage predictions, since debonding between core and facings was neither observed

during the experimental analyses, nor predicted by the FE model, even for impact events with the highest energy considered during the study.

Figure 6-4 reports the experimentally obtained stress-strain curves of foams with different densities (HP60, HP100 and HP160 foams, with densities of 65, 100 and 160 kg/m^3, respectively). The core material exhibits the typical deformation behaviour of closed-cell foams under compression, consisting of three regions: an initial linear elastic phase, a stress plateau, and a final densification stage, characterized by a steep increase in stiffness (Gibson and Ashby 1999).

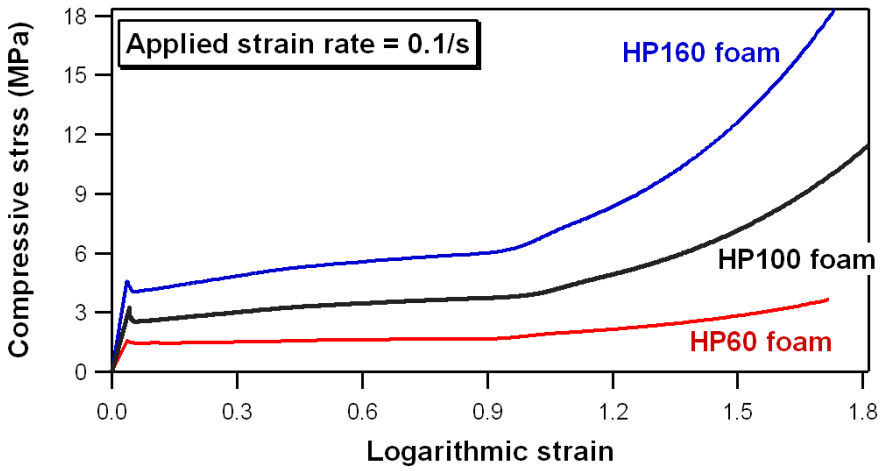

Figure 6-4: Experimental response of PVC foam under uniaxial compression.

6.3 Parallel Executions on Cluster System

In view of the computational complexity of investigated problem, the numerical solutions were obtained using the Abaqus/Explicit parallel solver. The calculations were carried out on a 12 CPU cluster of workstations based on Intel i7-860 processors and

Linux operating system, using the MPI library for parallel execution on distributed memory platforms supported by ABAQUS/explicit.

6.4 Concluding Remarks

This chapter gives an overall description of the numerical models constructed for simulating impacts on sandwich panels, of the material properties applied in the analyses as well as the Linux-based cluster system composed for solving the computational tasks.

Impacts on sandwich panels with various configurations were simulated and analyzed using the numerical models shown in this chapter; the results are presented in the following chapters.

CHAPTER 7

IMPACTS ON SANDWICH PANELS WITH CROSS-PLY LAMINATE SKINS

Impact on sandwich panels with cross-ply laminate facesheets (stacking sequence: $[0/90_3/0]$) bonded to a 10 mm PVC foam core (with three different foam densities: 65 kg/m^3 (HP60), 100 kg/m^3 (HP100) and 160 kg/m^3 (HP160)) was simulated for impact energies ranging approximately from 1 J to 8 J; numerical predictions were compared with experimental results in terms of both structural response and internal damage.

7.1 Analysis of Experimental Results

Figure 7-1 shows examples of measured impact load histories and force-displacement curves for sandwich composites with $[0/90_3/0]$ facings and HP60, HP100 or HP160 foam cores (core thickness = 10 mm) impacted with an energy of 6.3 J. The sandwich panels, 250 mm x 250 mm in size, were simply supported on a steel plate with a 45 mm x 67.5 mm rectangular opening.

It is seen that, as expected, the structural behaviour of the sandwich panels under impact is strongly influenced by the properties of the core material. The load-time histories of **Figure 7-1**a show that the peak load increases of about 25% and the impact duration decreases of approximately 30% when the core density is increased from 65 kg/m3 (HP60 foam) to 160 kg/m3 (HP160 foam). The effect of the core density is also

evident in the force-displacement curves of **Figure 7-1**b, which show that the slope of the curve significantly increases with foam density. The force-displacement plots have an approximately linear behaviour up to a load level of about 1 kN, above which the curves exhibit a stiffness decrease that may be associated to damage and degradation phenomena occurring in the laminated skins and in the cores during the impact events. It may be worth noting that larger slope reductions are recorded beyond this knee point in sandwich panels with the lower density core, thus suggesting that nonlinearities or damage events occurring in the core may possibly play a more significant role in low-density than in high-density foam sandwich composites. It is also seen that the response measured immediately after impact is affected by oscillations and fluctuations, which are signal features that typically appear, especially at high impact energies, in force data acquired during drop weight tests (Zhou, et al. 2012), and that may be associated to the inertial and dynamic behaviour of the plate-impactor system (Feraboli 2006). As the load becomes larger, a slight stiffness increase can be observed in the force-displacement plots.

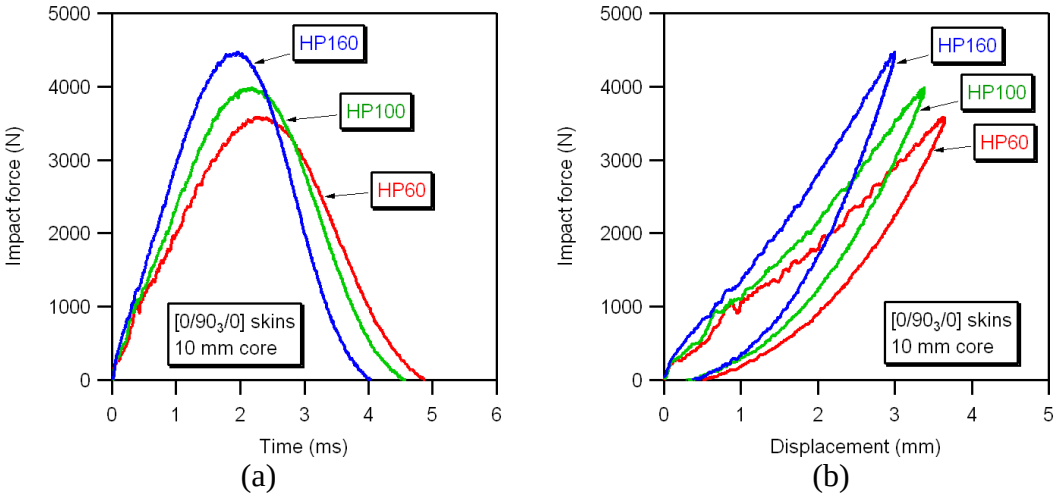

Figure 7-1: Force-time (a) and force-displacement (b) curves of [0/90$_3$/0] sandwich panels with HP60, HP100 and HP160 core impacted at 6.3 J.

Peak contact forces and energies absorbed during the impact by the composite sandwich panels are plotted as a function of impact energy in **Figure 7-2** and **Figure 7-3**. Both peak forces and absorbed energies values exhibit a rising trend that is roughly proportional to the impact energy, but while the values of the peak forces are evidently affected by foam density (as visible in **Figure 7-2**, significantly larger peak forces are sustained by HP100 and HP160 sandwich panels as compared to HP60 panels for the same impact energy), the dissipation of energy occurring during impact appears essentially independent of the density of the core (**Figure 7-3**).

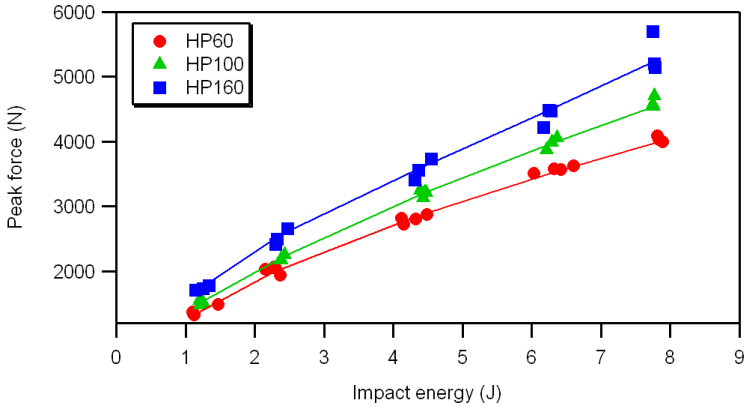

Figure 7-2: Peak contact forces recorded during impact on [0/90$_3$/0] sandwich panels.

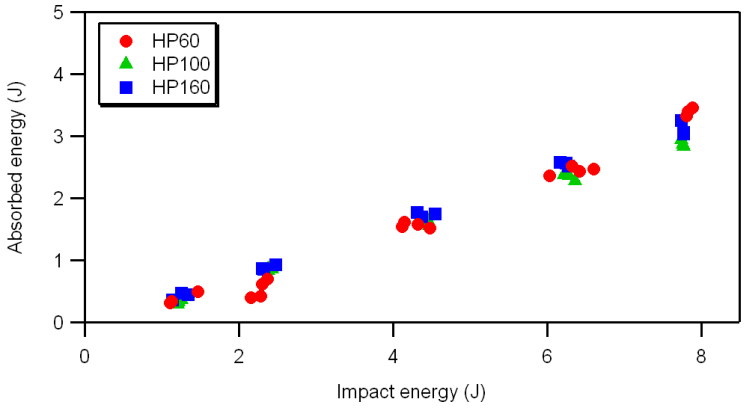

Figure 7-3: Energies absorbed during impact on [0/90$_3$/0] sandwich panels.

Figure 7-4 shows typical damage occurring in the facings of sandwich panels with HP60, HP100 and HP160 foam cores subjected to different impact energies. X-radiographic and microscopy analyses show that, in the range of impact energies investigated (between approximately 1 J and 8 J), the damage induced by impact consists of a combination of tensile or shear matrix cracks and delaminations. The experimental observations also indicate that the size, the nature and the evolution of the damage modes occurring in the laminated skins are not significantly affected by the density of the foam material used in the core.

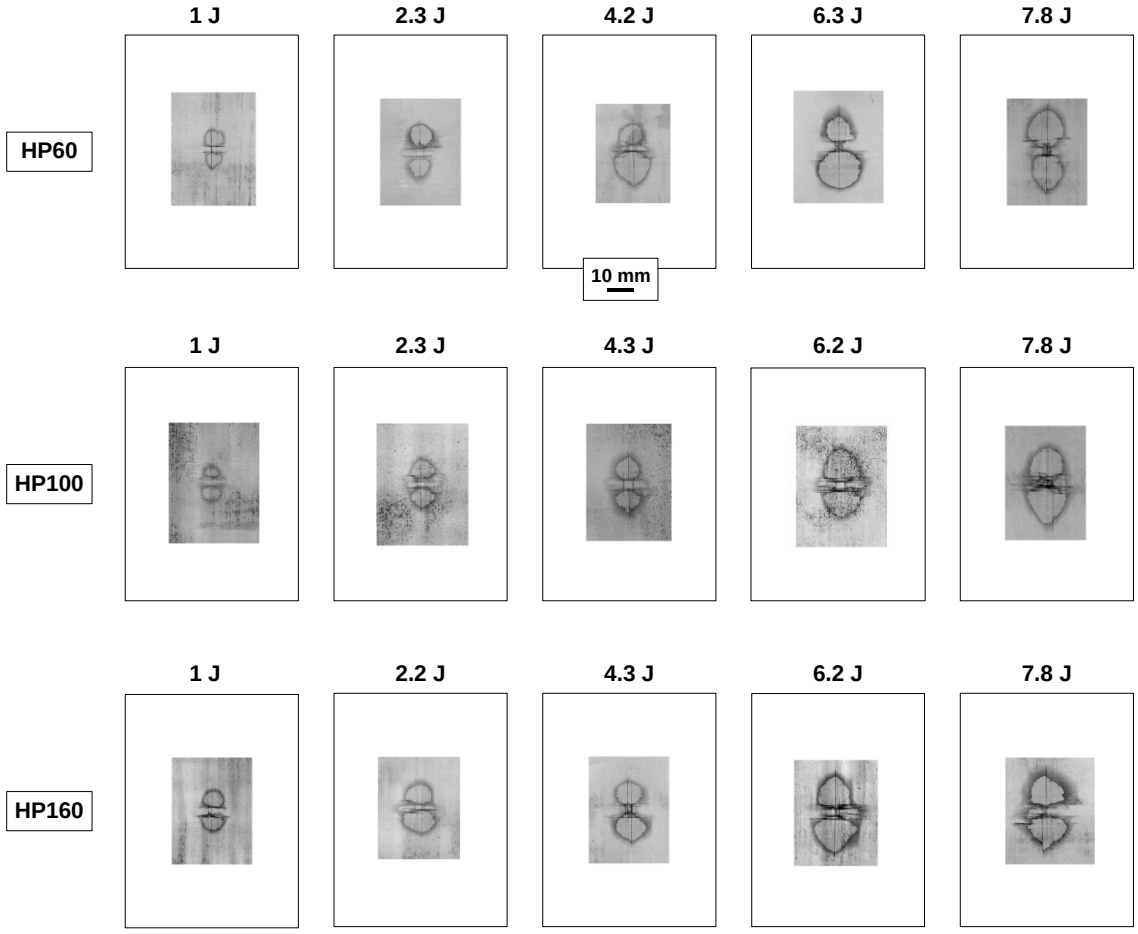

Figure 7-4: X-radiographs of damage induced by impacts on sandwich composites with [0/90_3/0] skins and with HP60, HP100 and HP160 foam cores.

For all HP60, HP100 and HP160 sandwich panels, initial damage in the impacted skin consists of tensile matrix cracks developing in the 0° layer farthest from the impact side, and of shear matrix cracking occurring in the middle 90° layers. With increasing impact energy, tensile and shear matrix cracks promote the initiation of a peanut-shape delamination on the 90°/0° interface between the cracked 0°and 90° plies. Small delaminations were observed on the 0°/90° interface close to the impact side. (**Figure 7-5**) No major fibre damage was detected in the impacted facings for the entire range of impact energies investigated.

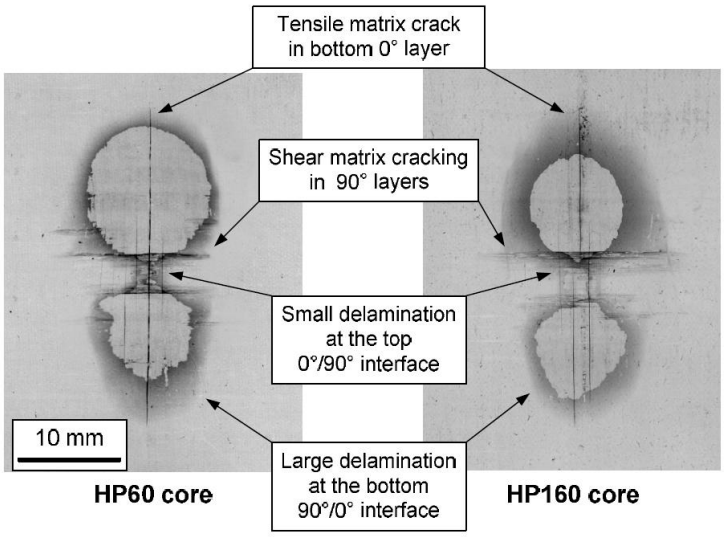

Figure 7-5: X-ray of typical impact damage on the facings of $[0/90_3/0]$ sandwich panels for an impact energy of 6.3J.

It is worth noting that microscopy inspections on polished cross-sections of selected sandwich panels after impact tests showed no clear evidence of major damage phenomena within the foam (such as large cavities or fractured cell walls) or of debonding between the core and the skin, even when the sandwich panels were impacted at the highest impact energies.

Figure 7-6 plots the projected delamination areas, defined as the projection onto a single plane of the delaminated areas at the two interfaces of the impacted skin, as a function of impact energy. It is seen that sandwich panels with HP60, HP100 and HP160 core have similar damage area values for the same impact energy, thus providing indication that the density of the foam core has a small influence on the impact damage resistance of the examined sandwich composites.

Furthermore, the experimental evidence acquired through combined non-destructive and destructive observations show that very little damage occur in the laminated facings at the load level corresponding to the knee point of the force-displacement curves. This suggests that the stiffness reduction exhibited by the sandwich panels at the knee load is mainly induced by nonlinearities associated to localized cell buckling of the foam material below the indentation area, rather than by damage in the composite skins.

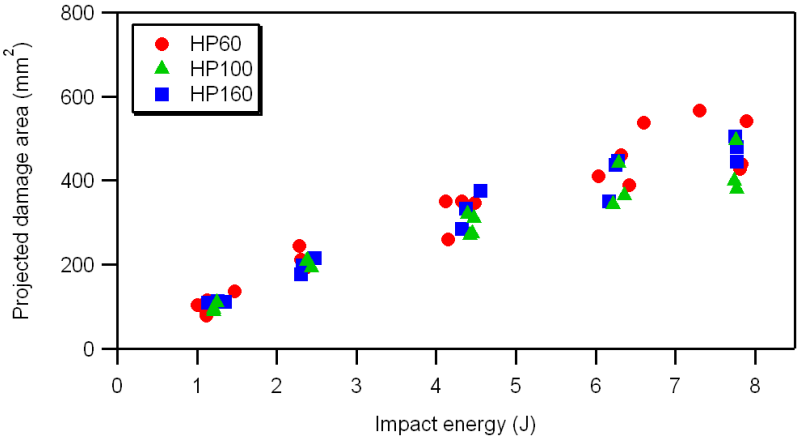

Figure 7-6: Projected delamination areas as a function of impact energy for [0/90$_3$/0] sandwich panels.

7.2 Comparison between Simulations and Experiments

7.2.1 Structural Response

Force vs time and force vs displacement curves predicted by the developed FE model at different levels of impact energy are compared to experimental data in **Figure 7-7** (HP60 panels), **Figure 7-8** (HP100 panels) and **Figure 7-9** (HP160 panels). The figures show that a rather good agreement is achieved between experiments and predictions for both force-time histories and force-displacement curves. The model is able to capture with good accuracy the peak force values (even if some minor discrepancy may be noticed at the highest impact energy level for HP160 panels) and the impact durations for HP60-, HP100- and HP160-based sandwich composites over the whole range of impact energies investigated. In addition, the typical nonlinear trends exhibited by experimental force versus displacement data, characterized by a distinct threshold load above which a clear slope reduction is observed, are also correctly predicted by the FE analyses.

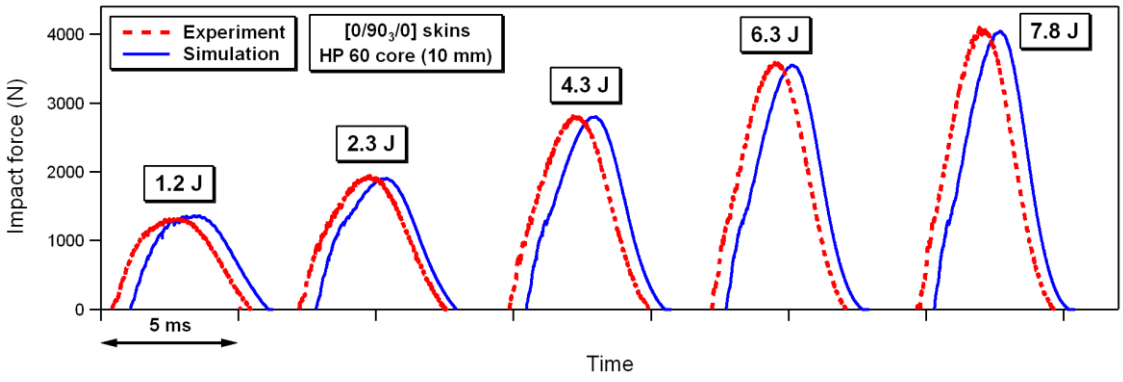

(a)

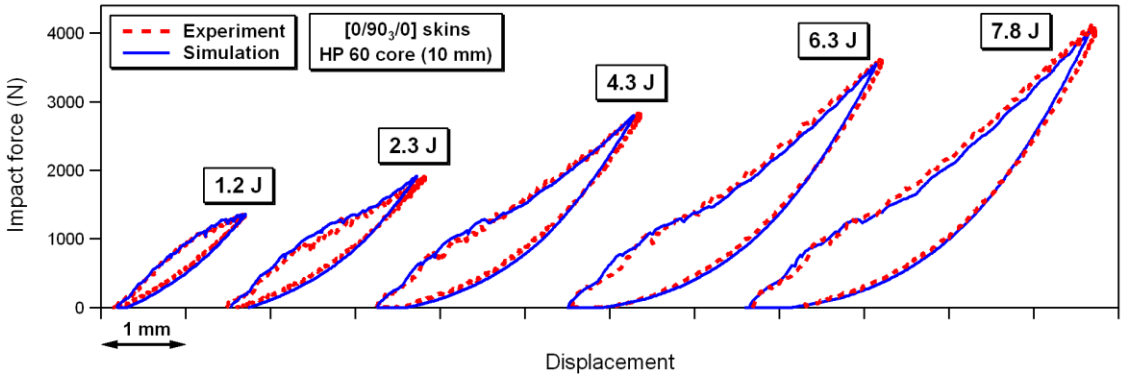

(b)

Figure 7-7: Comparison between predicted and experimental force-time (a) and force-displacement (b) curves for sandwich panels with HP60 core.

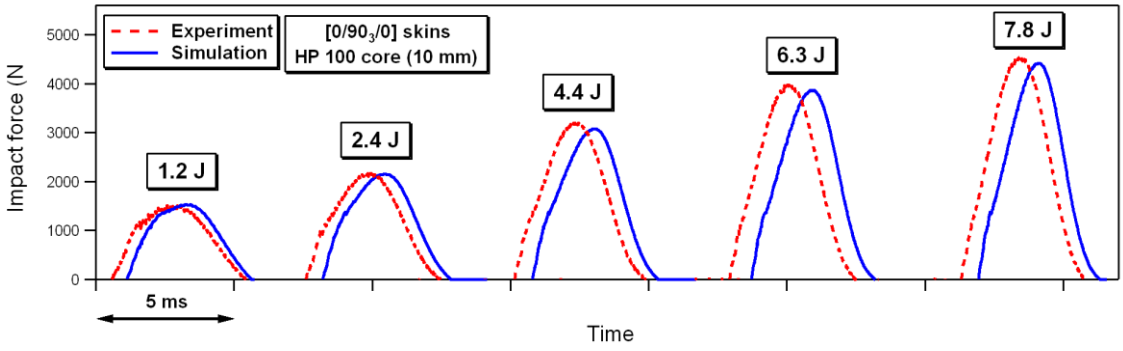

(a)

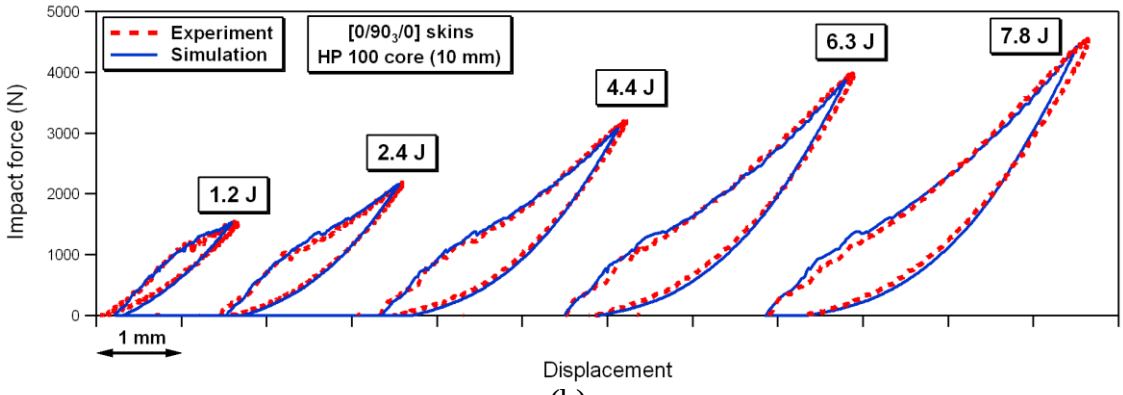

(b)

Figure 7-8: Comparison between predicted and experimental force-time (a) and force-displacement (b) curves for sandwich panels with HP100 core.

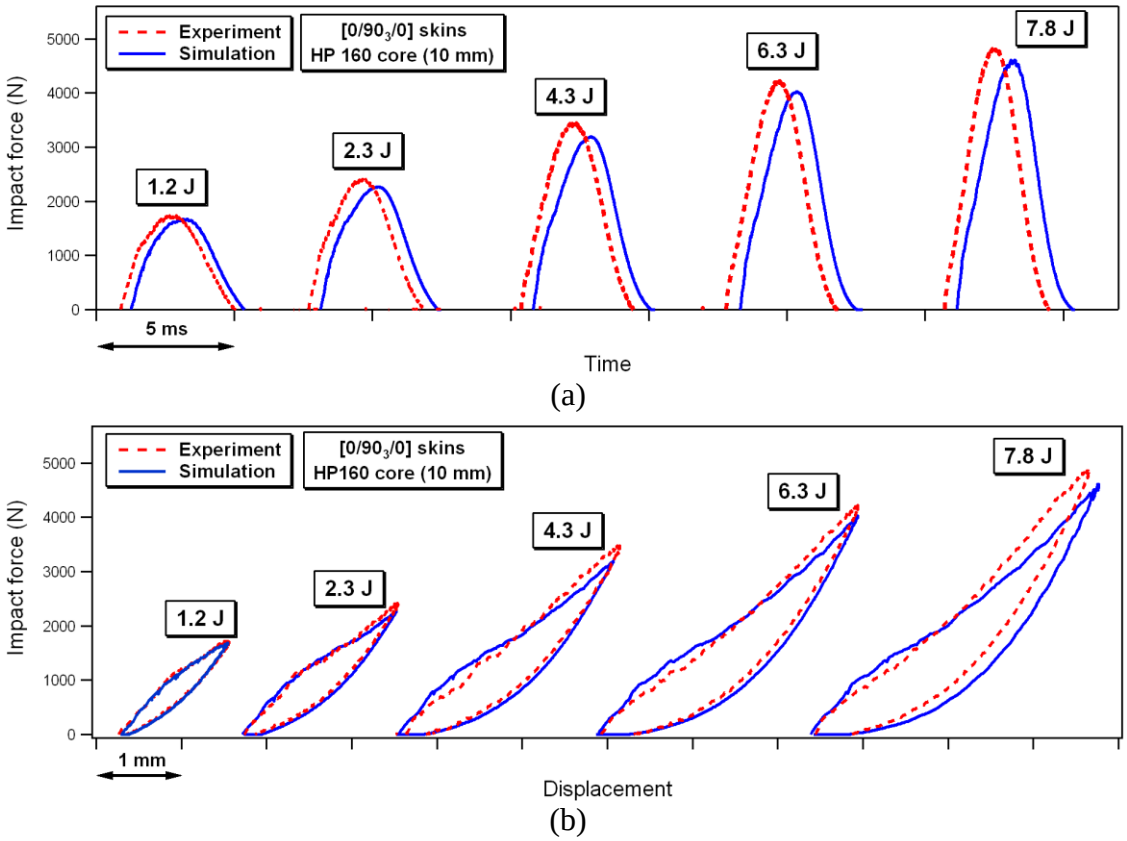

Figure 7-9: Comparison between predicted and experimental force-time (a) and force-displacement (b) curves for sandwich panels with HP160 core.

Quantitative comparisons of predicted and measured peak contact forces and absorbed energies are shown in **Figure 7-10**, **Figure 7-11** and **Figure 7-12** for HP60, HP100 and HP160 panels, respectively. The predicted values of the absorbed energy plotted in the graphs are calculated as the area under the force-displacement curve, and represent the total energy dissipated during the impact in irreversible damage mechanisms (foam nonlinearities, intralaminar or interlaminar fracture in the impacted facesheet, and plastic deformation in the composite layers). The graphs show that there is a very good correlation between numerical predictions and experimental data, with only a slight tendency of the FE model to underpredict the

maximum force values at high impact energies for HP160 sandwich panels.

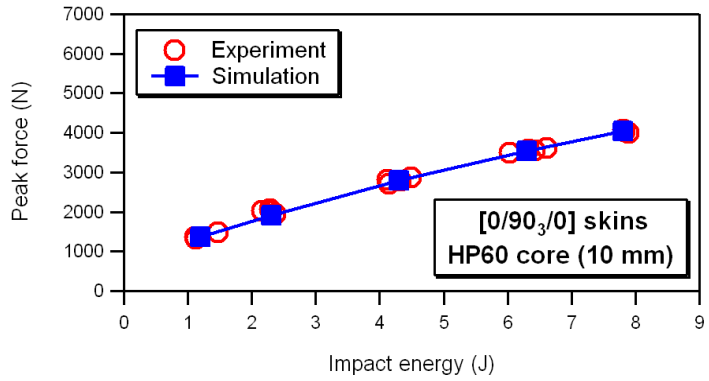

(a)

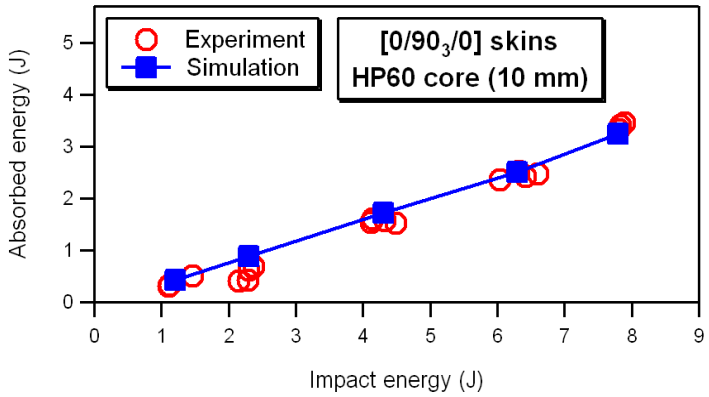

(b)

Figure 7-10: Comparison between predicted and measured peak contact forces (a) and absorbed energies (b) for sandwich panels with HP60 core.

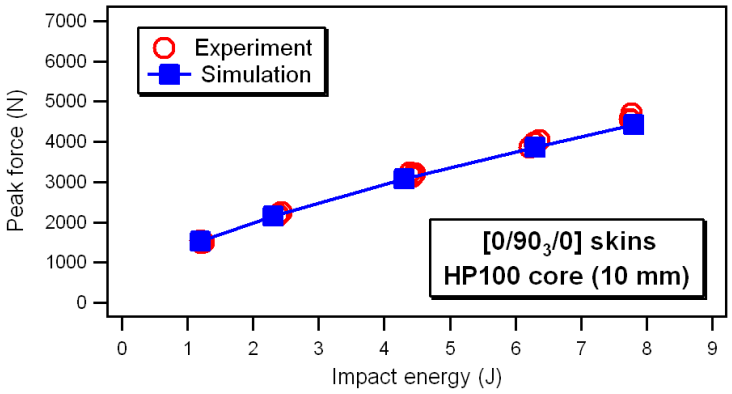

(a)

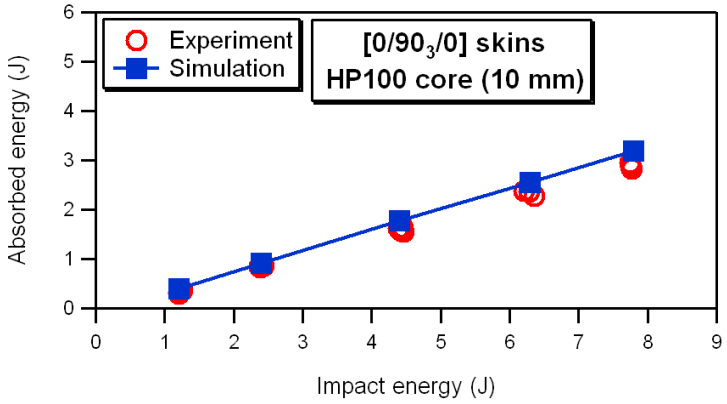

(b)

Figure 7-11: Comparison between predicted and measured peak contact forces (a) and absorbed energies (b) for sandwich panels with HP100 core.

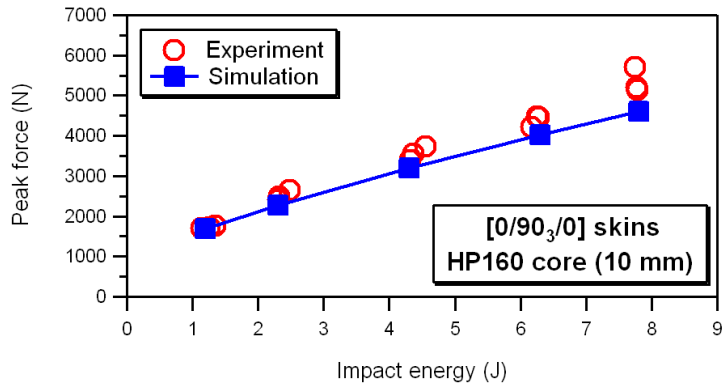

(a)

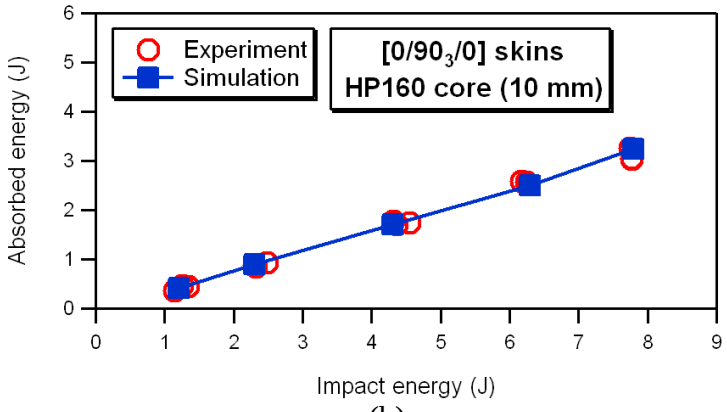

(b)

Figure 7-12: Comparison between predicted and measured peak contact forces (a) and absorbed energies (b) for sandwich panels with HP160 core.

7.2.2 Internal Damage

Experimental and numerical results for sandwich panels of the three foam densities are compared in **Figure 7-13**-**Figure 7-18** in terms of damage occurring in the composite skins at different impact energies. **Figure 7-13**, **Figure 7-15** and **Figure 7-17** report experimental and predicted values of projected damage areas, while the graphs of **Figure 7-14**, **Figure 7-16** and **Figure 7-18** plot length (maximum size along the 0° direction) and width (average of the maximum size along the 90° direction of the two delaminated lobes, as defined in **Figure 7-14**) of projected damage. Images of projected damage areas as revealed by X-radiography and predicted by FE simulations for various impact energies, taking sandwich panels with HP160 foam cores as the example, are directly compared in **Figure 7-19**.

The comparisons show that the FE simulations predict with reasonable accuracy, for all HP60, HP100 and HP160 sandwich panels, length, width and global size of the projected damage area induced by impact as well as the general trends of these parameters with increasing impact energy.

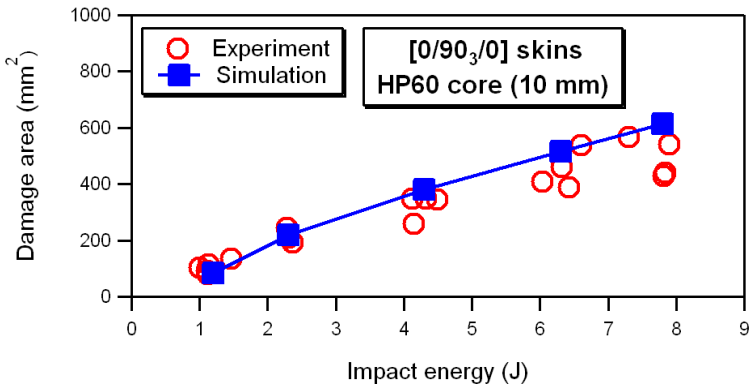

Figure 7-13: Comparison between measured and predicted projected damage areas for sandwich panels with HP60 core.

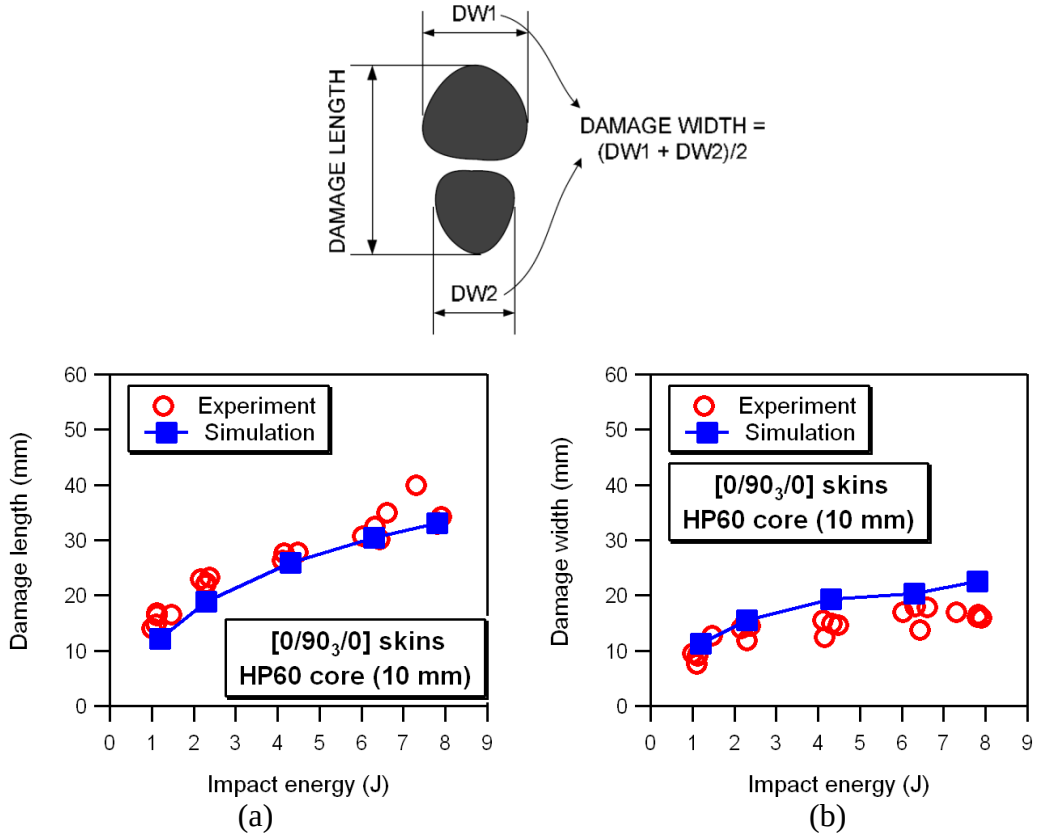

Figure 7-14: Comparison between measured and predicted damage length (a) and damage width (b) for sandwich panels with HP60 core.

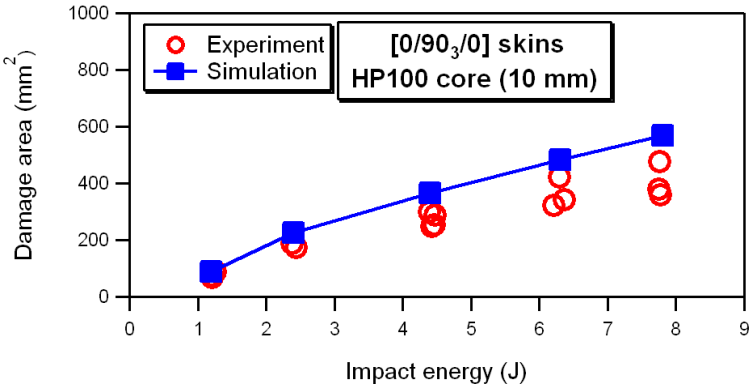

Figure 7-15: Comparison between measured and predicted projected damage areas for sandwich panels with HP100 core.

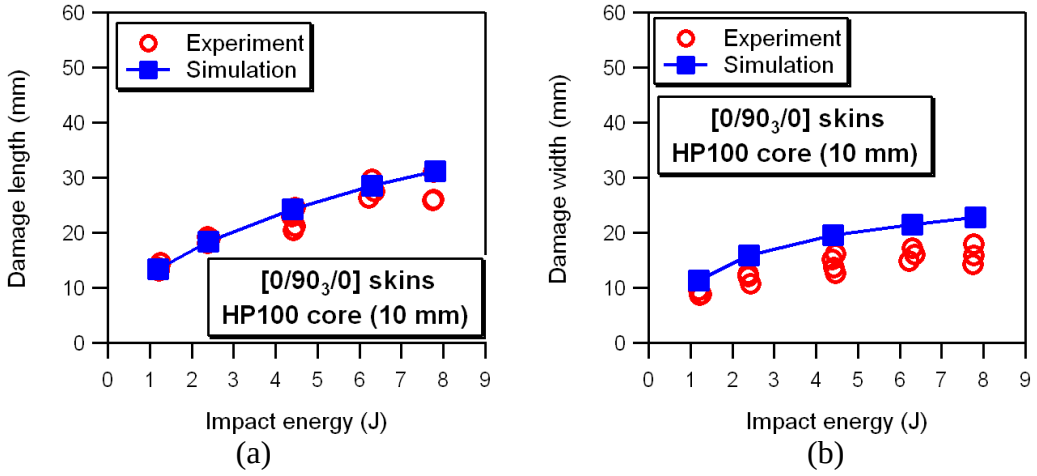

Figure 7-16: Comparison between measured and predicted damage length (a) and damage width (b) for sandwich panels with HP100 core.

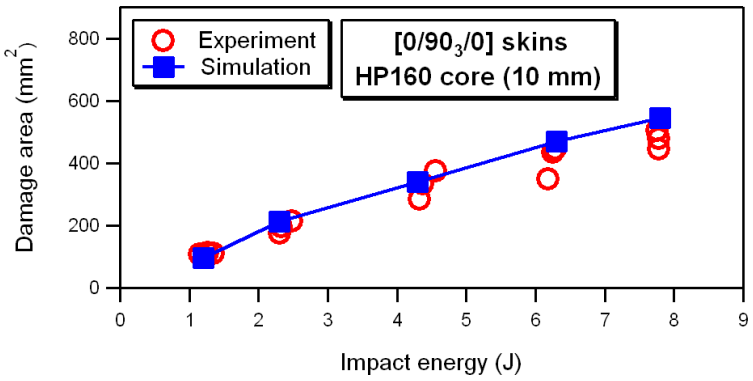

Figure 7-17: Comparison between measured and predicted projected damage areas for sandwich panels with HP160 core.

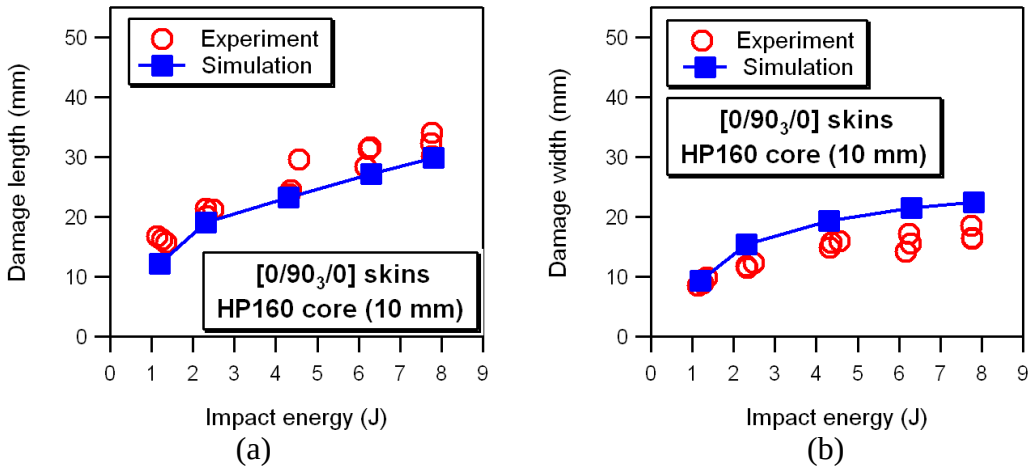

Figure 7-18: Comparison between measured and predicted damage length (a) and damage width (b) for sandwich panels with HP160 core.

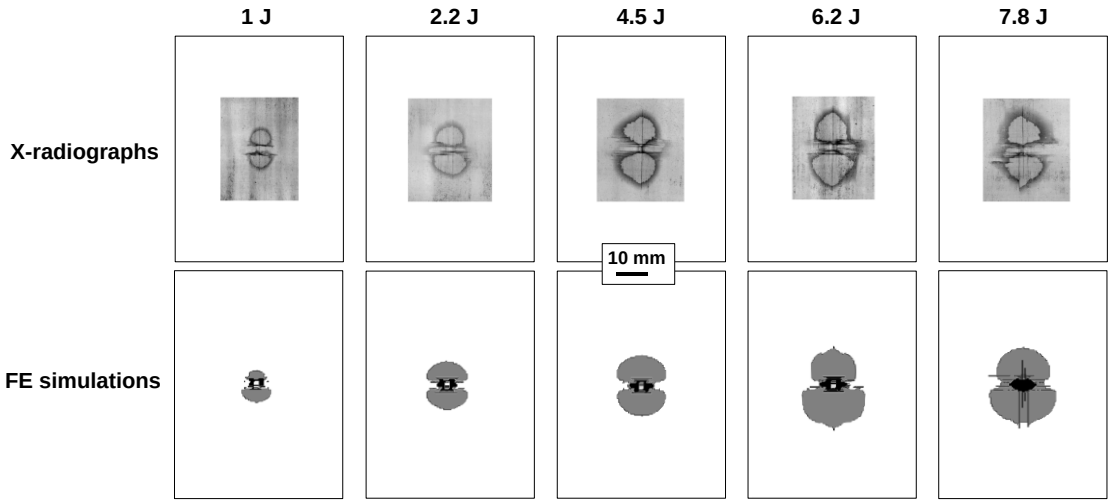

Figure 7-19: Comparison between experimental and predicted impact damage (different gray levels correspond to different delamination depths) in sandwich panels with HP160 foam cores under five impact energies.

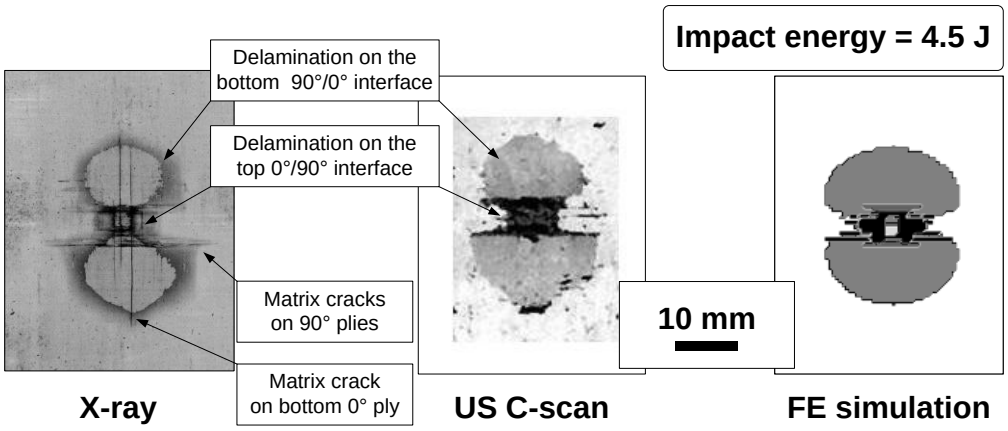

Figure 7-20: Comparison between X-radiograph, ultrasonic C-scan and predicted damage areas for $[0/90_3/0]$ sandwich panels with HP160 core impacted at 4.5 J.

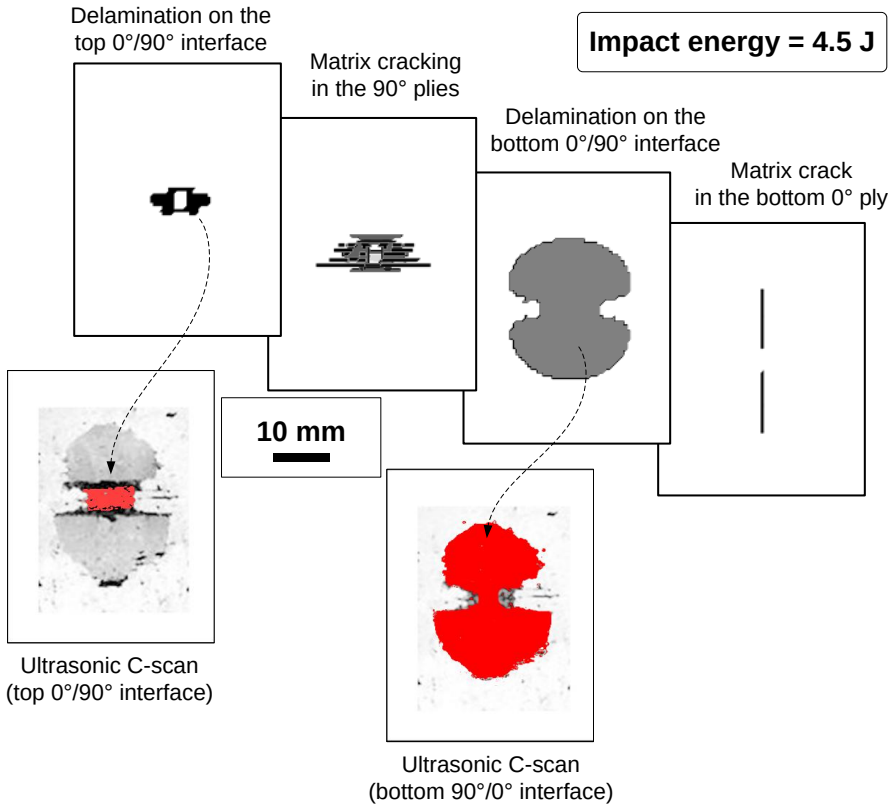

Figure 7-21: Through-thickness distribution of main damage modes as predicted by FE model and constructed by ultrasonic C-scans for $[0/90_3/0]$ sandwich panels with HP160 core impacted at 4.5 J.

Figure 7-20 shows an example of comparison between X-radiograph, ultrasonic C-scan and predicted damage areas with HP160 sandwich panel subjected to a 4.5 J impact. **Figure 7-21** compares the through-thickness distribution of main damage modes for the same impact case. It is seen that a good agreement is achieved between numerical results and experiment observations. The FE model simulates with reasonably good accuracy in size and shape both the bottom 90°/0° delamination, with its typical peanut shape elongated in the fibre direction of the lowermost layer, as well as the smaller delamination on the top 0°/90° interface. In agreement with experimental evidence, the bending matrix cracking in the bottom 0° ply and shear matrix cracks in central 90° plies are also correctly predicted by the FE model.

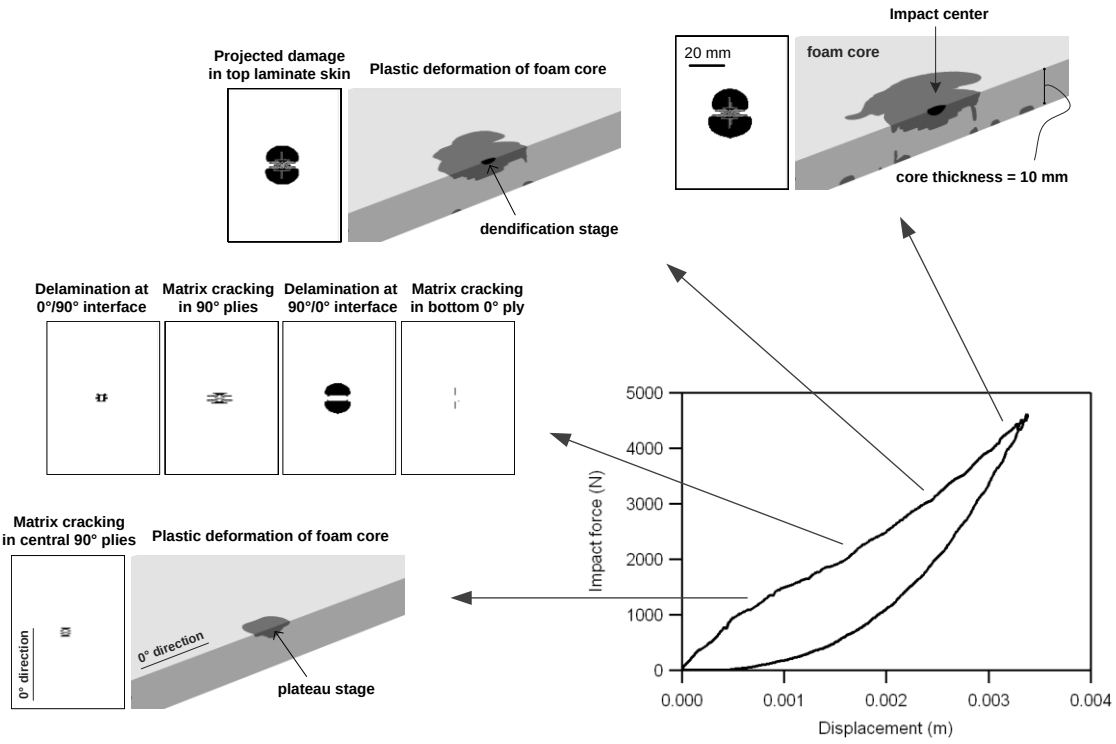

Figure 7-22: Sequence of damage events predicted by the FE model for a 7.8 J impact on a $[0/90_3/0]$/HP160 sandwich panel.

The numerical analyses also provide an accurate prediction of the sequence of the major damage events and of the key features and shapes of the individual damage modes occurring through the laminate thickness at specific interfaces or layers of the sandwich panels. As an example, **Figure 7-22** shows different stages of damage evolution as simulated by the FE model during a 7.8 J impact on a HP160-base sandwich plate. The numerical simulations indicate that a significant volume of foam core below the impact area reaches the plateau stress stage (where plastic strain of the foam increases at a nearly constant compressive stress) at an impact force level of about 1 kN, while only a small amount of matrix cracking is predicted in 90° layers of the laminated facesheet; these results support the assumption that the stiffness reduction exhibited by the force-displacement curve at the knee load is mainly induced by localized cell buckling of the foam material, rather than by damage of the composite skin. The development of a major tensile matrix crack in the bottom 0° layer, a two-lobe delamination at the bottom 90°/0° interface and a smaller delamination at the top 0°/90° interface are subsequently predicted by the model under increasing contact forces. When the impact force achieves about 3 kN, a small area of foam under the impact center reaches the densification stage (where the compressive stress of foam increase rapidly with increasing strain); the initiation of foam densification, together with membrane effects on the impacted skin, could account for the continuous slight increase in slope exhibited by the force-displacement curve after the stiffness drop at the knee point. In agreement with experimental observations, no debonding at the core/skin interface and no fibre breakage in the laminated skin is predicted by the model.

7.3 Concluding Remarks

Low-velocity impacts on sandwich panels with cross-ply laminate skins ($[0/90_3/0]$) were simulated by applying the implemented failure models. Numerical simulations were compared with experimental results for sandwich panels with different foam cores (HP60, HP100 and HP160) subjected to various impact energies. It is shown that the numerical predictions are quite good not only in terms of structural response (force histories, force-displacement curves and absorbed energies), but also in terms of internal damage (temporal sequence of major damage events; projected damage shapes, sizes and through-thickness distributions).

CHAPTER 8

IMPACTS ON SANDWICH PANELS WITH MULTI-DIRECTIONAL LAMINATE SKINS

Investigation of impacts on sandwich panels with multidirectional laminate skins (stacking sequence: $[0_3/+45/-45]_S$) bonded to a 10 mm PVC foam core with different foam densities(65 kg/m^3 (HP60), 100 kg/m^3 (HP100) and 160 kg/m^3 (HP160)) was also carried out.

8.1 Analysis of Experimental Results

Typical load histories and force-displacement curves measured during 6.2 J impacts on sandwich composites with $[0_3/+45/-45]_S$ facings and 10 mm-thick HP60, HP100 and HP160 foam cores are shown in **Figure 8-1**. Similarly to what observed in panels with $[0/90_3/0]$ skins, $[0_3/+45/-45]_S$ sandwich composites exhibit a strong increase in maximum contact force and force-displacement slope, as well as a decrease in impact duration, with increasing foam density, thus confirming that the local structural response to impact of sandwich composites is greatly affected by the properties of the core.

In spite of the presence of inertial oscillations during the initial stages of the impact, it may be also seen that the force-displacement curves are approximately linear up to a load level of about 2 kN, beyond which the curves clearly exhibit a significant decrease in slope.

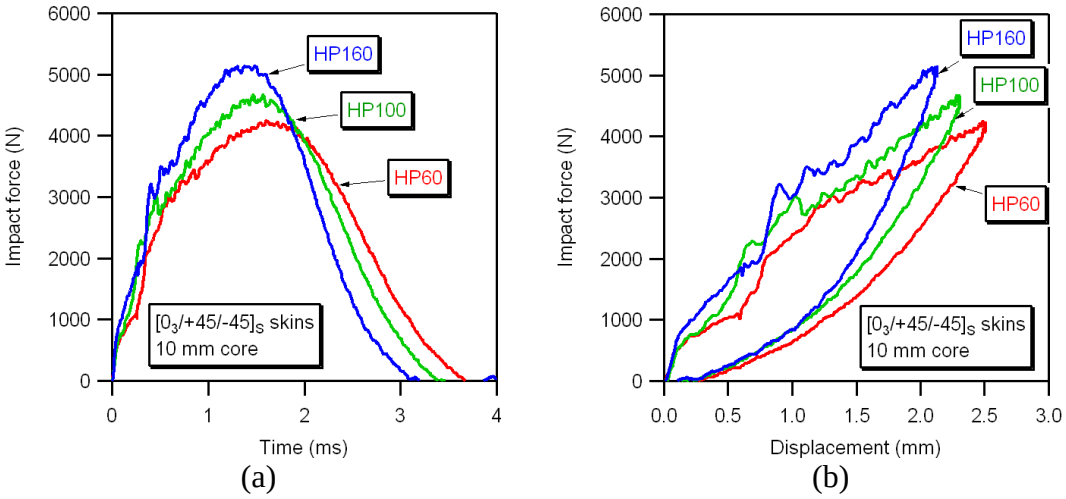

Figure 8-1: Force-time (a) and force-displacement curves (b) for $[0_3/+45/-45]_S$ sandwich panels with HP60, HP100 and HP160 foam cores. Impact energy=6.2 J.

The trends of peak contact forces and energies absorbed during the impact as a function of impact energy (**Figure 8-2** and **Figure 8-3**) are also analogous to those observed in $[0/90_3/0]$ sandwich composites. In particular, the dissipation of energy appears to be substantially independent of the foam density, in spite of the fact that HP100 and HP160 sandwich panels are subjected to larger impact forces, for the same impact energy, than HP60-based panels.

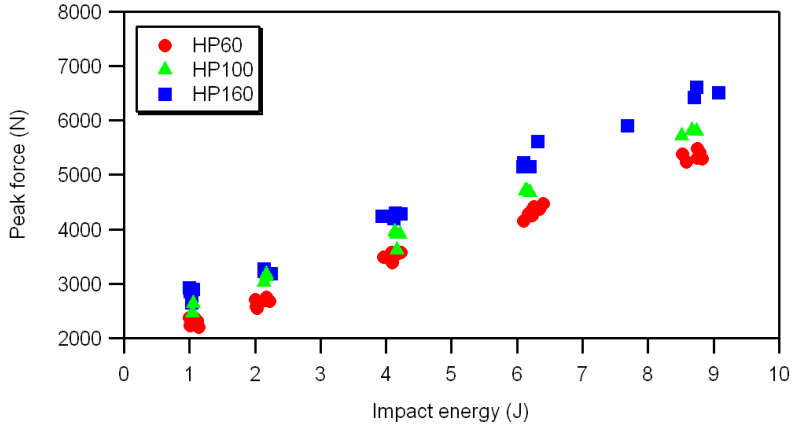

Figure 8-2: Peak forces recorded during impact on $[0_3/+45/-45]_S$ sandwich panels.

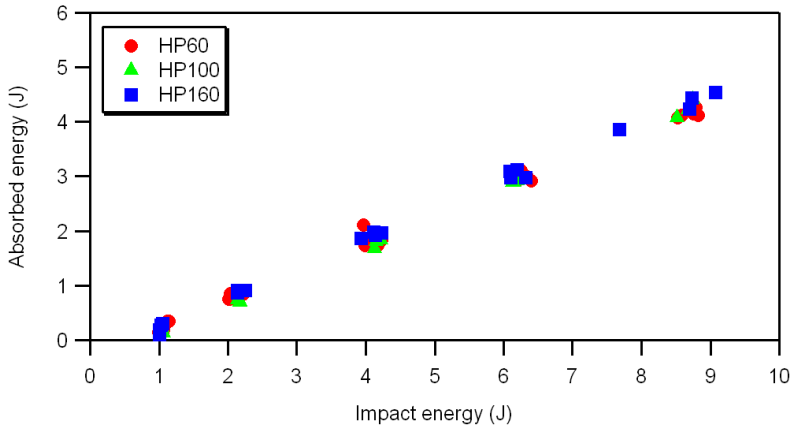

Figure 8-3: Energies absorbed during impact on $[0_3/+45/-45]_S$ sandwich panels.

The X-radiographs of **Figure 8-4** show typical damage induced by impacts in the composite facings of HP60, HP100 and HP160 sandwich panels. In all sandwich configurations, damage initiates at an impact energy level of about 1 J with a large bending matrix crack developing in the lower 0° layers, immediately followed by delamination at the -45°/+45° interface and fine matrix cracking in the +45° plies. With increasing impact energies, delaminations tend to initiate and grow at all remaining interfaces between layers with different orientations, in association with matrix cracking in adjacent layers. (**Figure 8-5**) Significant fibre damage, consisting of short fibre fracture paths developing in the top 0° layers in the indentation area, is only observed for impact events with energies higher than about 6 J.

As in sandwich panels with $[0/90_3/0]$ skins, collapse of the foam material in the vicinity of the impacted region, as opposed to damage in the composite layers (which is still very limited immediately after reaching the knee point of the force-displacement curves), appears as the major degradation mechanism responsible for the change in stiffness exhibited by the sandwich panels at the knee load.

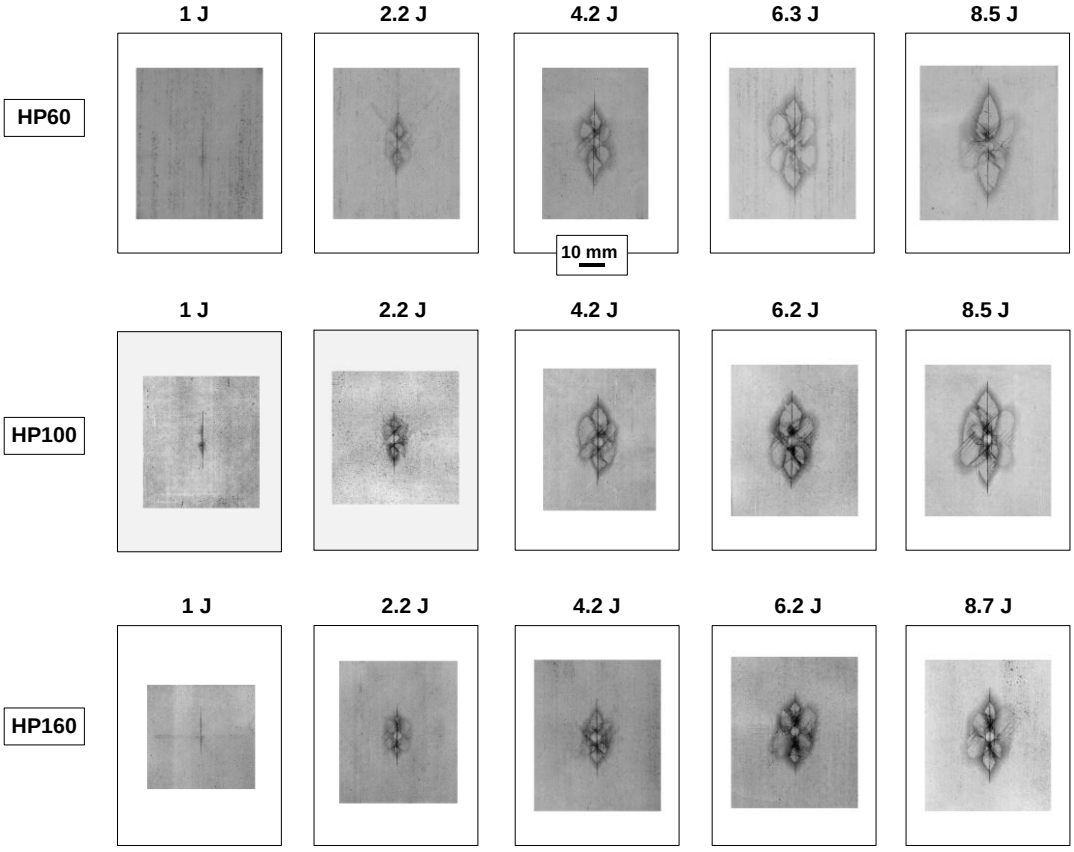

Figure 8-4: X-radiographs of damage induced by impacts for sandwich composites with $[0_3/+45/-45]_S$ skins and with HP60, HP100and HP160 foam cores.

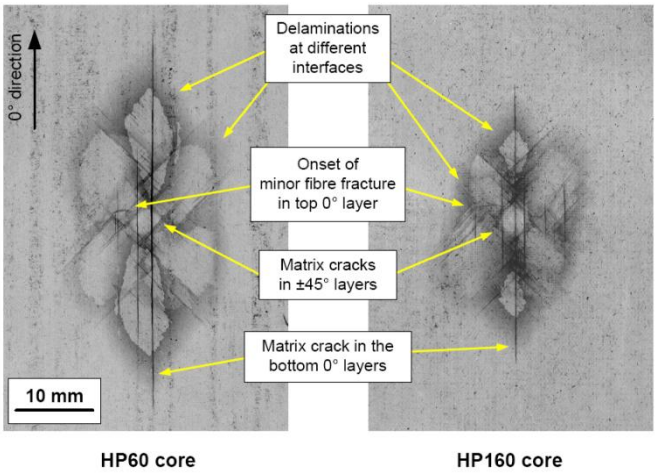

Figure 8-5: X-ray of typical impact damage on the facings of $[0_3/+45/-45]_S$ sandwich panels for an impact energy of 6.3J.

The areas of the projected damage induced by impact are plotted versus impact energy in the graph of **Figure 8-6**. Even though the features and the temporal sequence of the damage mechanisms occurring in sandwich composites with HP60, HP100 and HP160 core are very similar, we may notice that sandwich panels with higher foam densities (HP100 and HP160) exhibit smaller projected delamination areas (as clearly visible in the comparison of **Figure 8-4**), in spite of the larger impact forces experienced by HP100- and HP160-based panels as compared to HP60 panels.

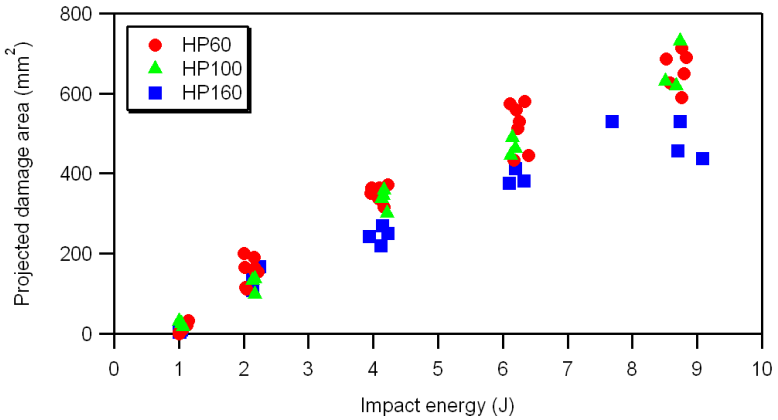

Figure 8-6: Projected delamination areas for $[0_3/+45/-45]_S$ sandwich panels.

8.2 Comparison between Simulations and Experiments

8.2.1 Structural Response

The structural responses predicted by FE simulations at different levels of impact energy are compared to experimentally obtained curves in **Figure 8-7** - **Figure 8-9**. It may be seen that a good agreement is achieved between FE simulations and experiments in terms of both force-time histories and force-displacement relationships for the three sandwich configurations. In particular, the developed FE model is capable of reproducing

the characteristic nonlinearities, as well as the drastic stiffness change occurring above a threshold load level, typical of the deformation response of the sandwich panels.

The good match achieved between experiments and predictions is also confirmed by the comparisons illustrated in the graphs of **Figure 8-10 - Figure 8-12**, which plot the maximum contact forces and the energies absorbed during the impact for sandwich composites with the three examined core densities.

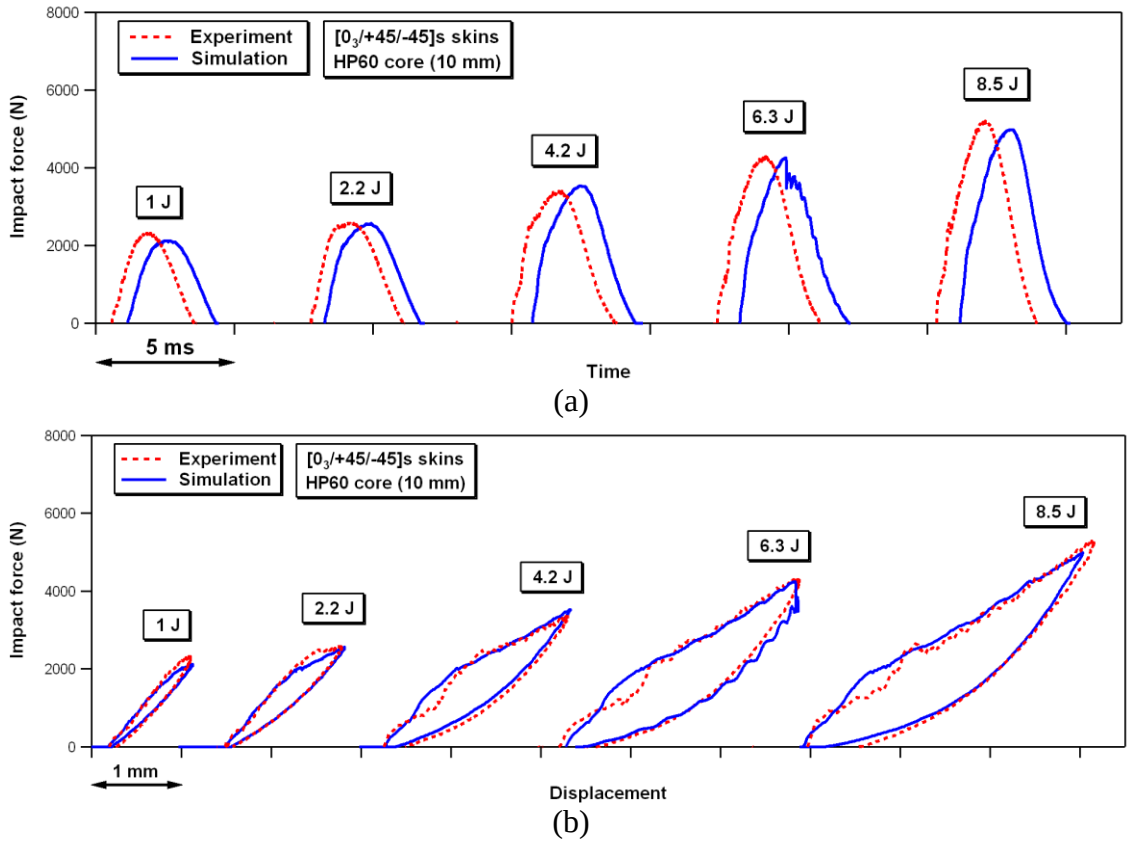

Figure 8-7: Comparison between predicted and experimental force-time (a) and force-displacement (b) curves for sandwich panels with HP60 core.

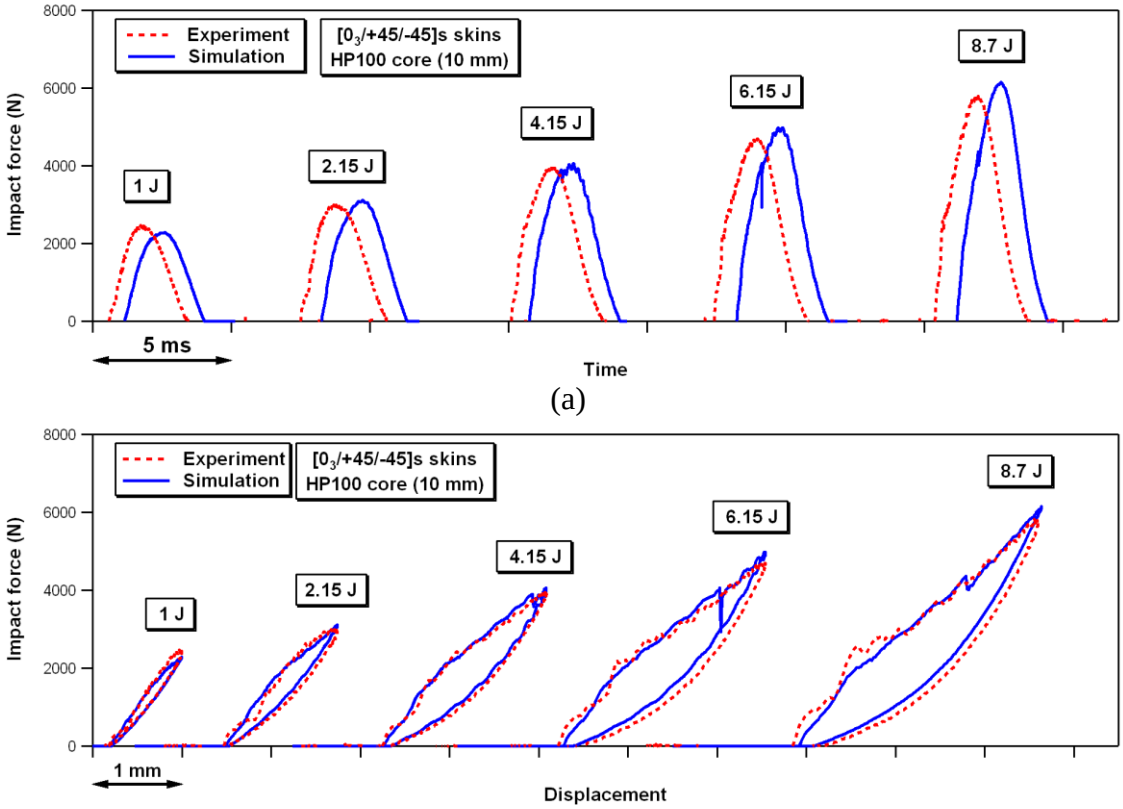

Figure 8-8: Comparison between predicted and experimental force-time (a) and force-displacement (b) curves for sandwich panels with HP100 core.

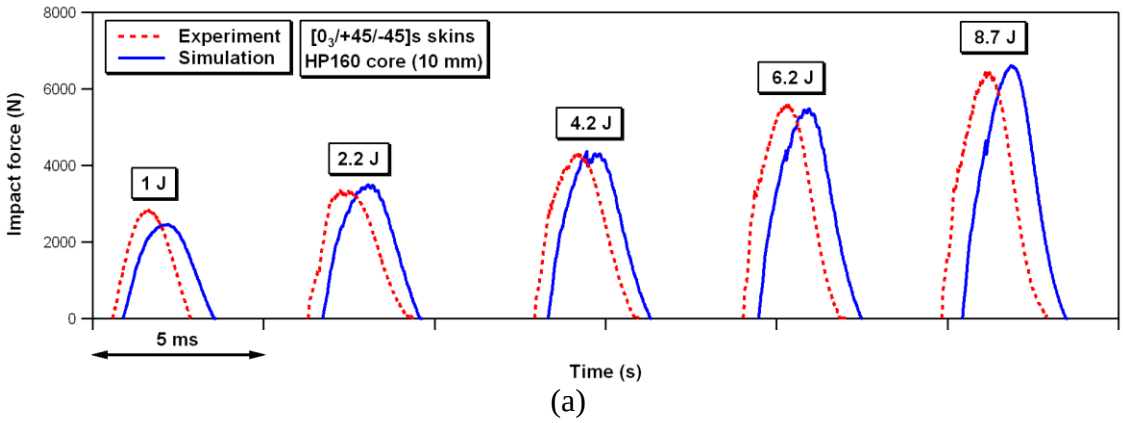

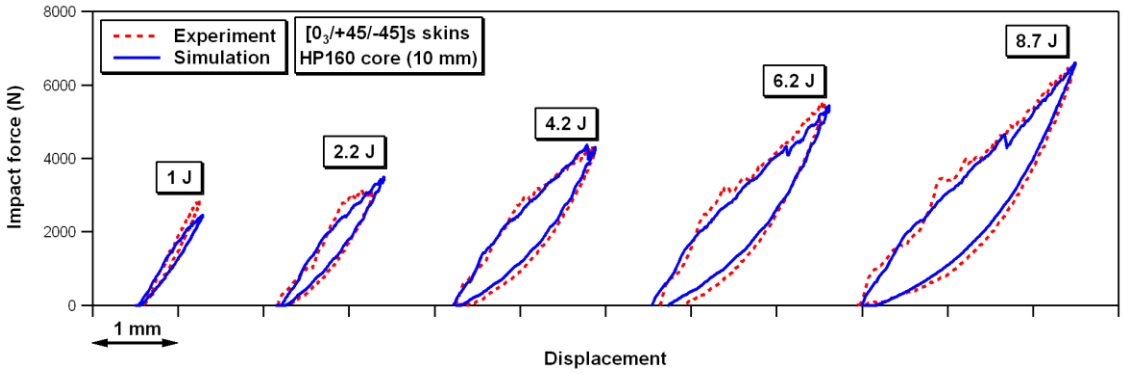

(b)

Figure 8-9: Comparison between predicted and experimental force-time (a) and force-displacement (b) curves for sandwich panels with HP160 core.

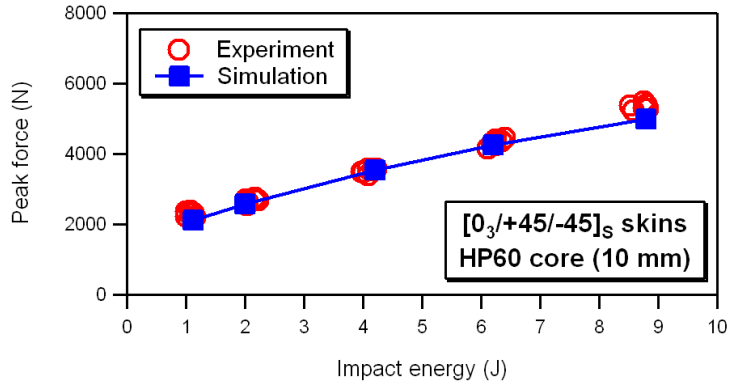

(a)

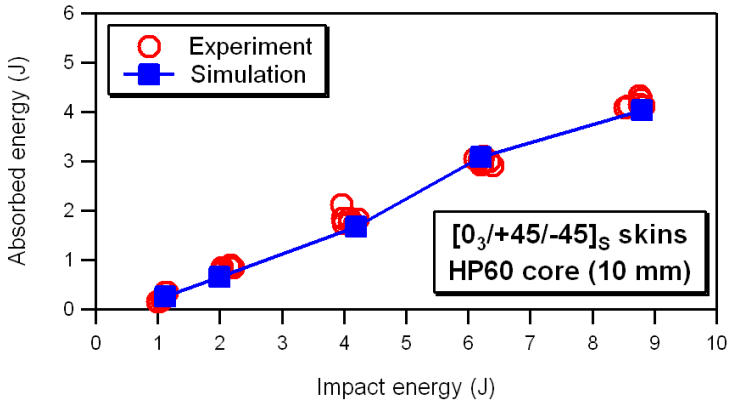

(b)

Figure 8-10: Comparison between predicted and measured peak contact forces (a) and absorbed energies (b) for sandwich panels with HP60 core.

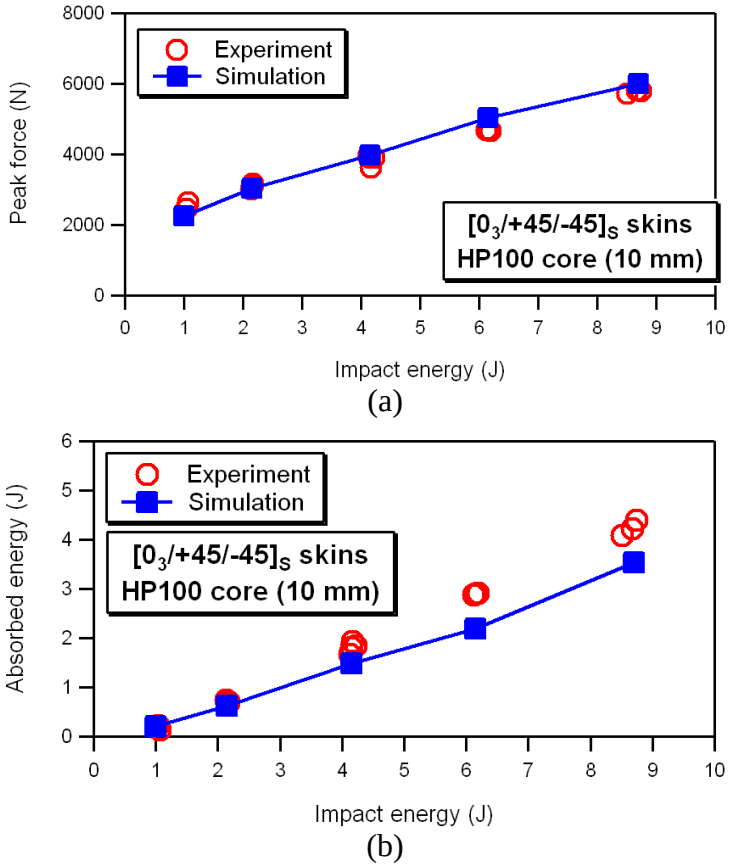

Figure 8-11: Comparison between predicted and measured peak contact forces (a) and absorbed energies (b) for sandwich panels with HP100 core.

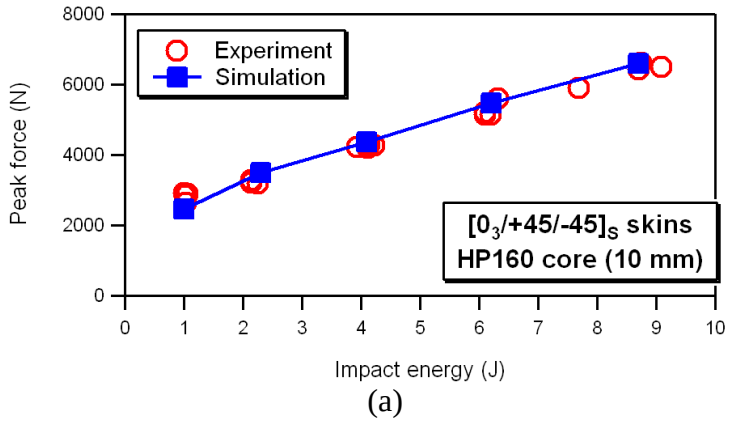

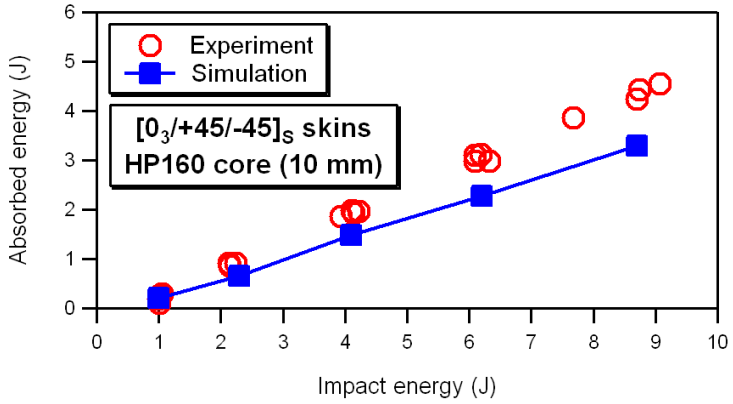

(b)

Figure 8-12: Comparison between predicted and measured peak contact forces (a) and absorbed energies (b) for sandwich panels with HP160 core.

8.2.2 Internal Damage

Comparisons between experiments and simulations in terms of damage occurring in the composite skins at different impact energies for HP60, HP100 and HP160 sandwich panels are illustrated in the graphs of **Figure 8-13** - **Figure 8-20**.

Figure 8-13, **Figure 8-14** and **Figure 8-15** report experimental and predicted values of projected damage areas, while the graphs of **Figure 8-16**, **Figure 8-17** and **Figure 8-18** plot length and width of projected damage (length and width of damage are schematically defined in the inset of **Figure 8-16**). Images of projected delaminated areas as revealed by X-radiography and predicted by FE simulations (where different colours correspond to different delamination depths) are compared in **Figure 8-19** (HP60 sandwich panels) and **Figure 8-20** (HP160 sandwich panels).

The results illustrated in **Figure 8-13** - **Figure 8-20** show that the FE model accurately predicts the size of total damage induced by impact in the three sandwich configurations, correctly simulating smaller damage areas in sandwich composites with

higher core density (HP100, HP160); the model is also able to reproduce the elongated shape of the projected delaminated areas, with the major axis oriented along the 0° direction, and to capture the different rate of growth of projected damage along the 0° direction (damage length) and 90° direction (damage width).

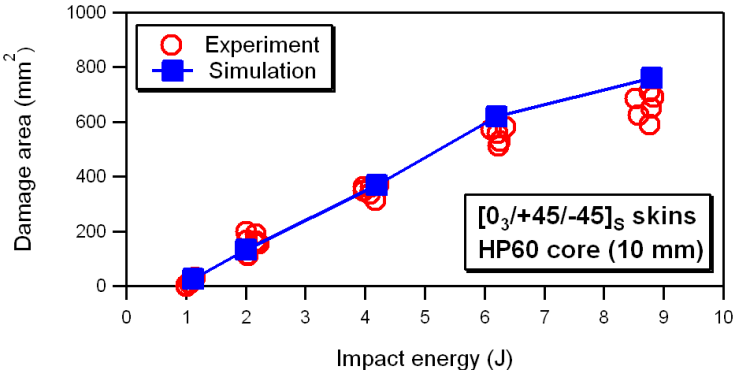

Figure 8-13: Comparison between measured and predicted projected damage areas for sandwich panels with HP60 core.

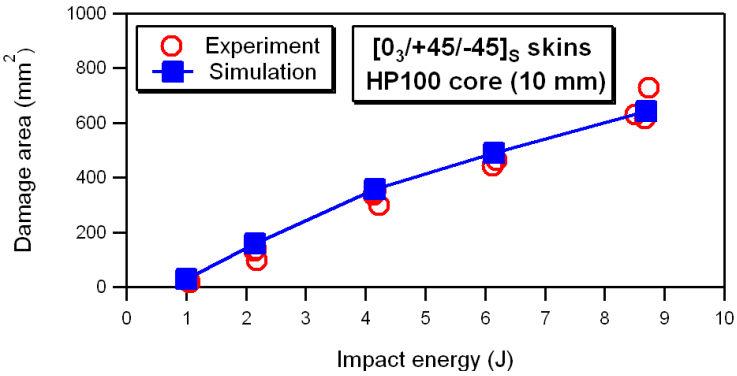

Figure 8-14: Comparison between measured and predicted projected damage areas for sandwich panels with HP100 core.

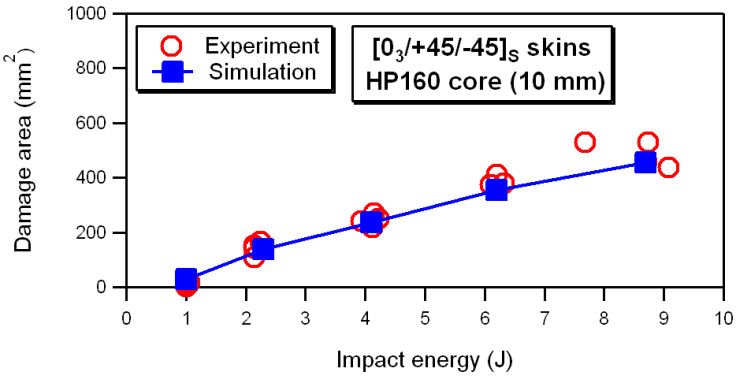

Figure 8-15: Comparison between measured and predicted projected damage areas for sandwich panels with HP160 core.

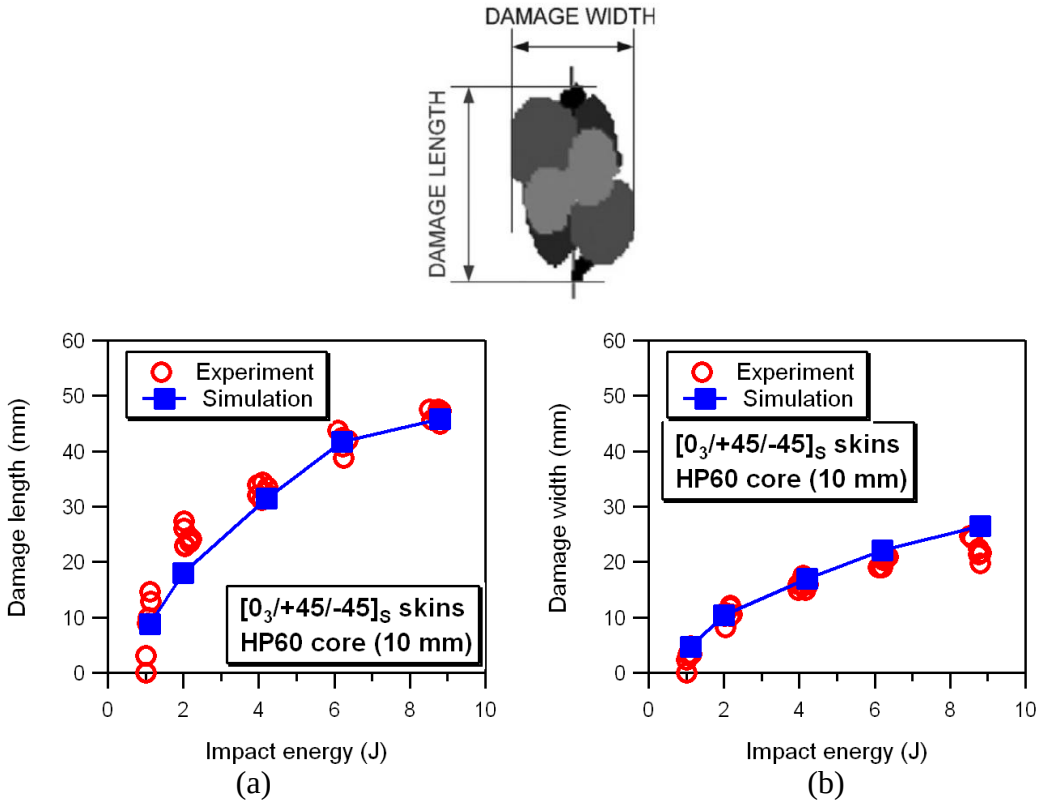

Figure 8-16: Comparison between measured and predicted damage length (a) and damage width (b) for sandwich panels with HP60 core.

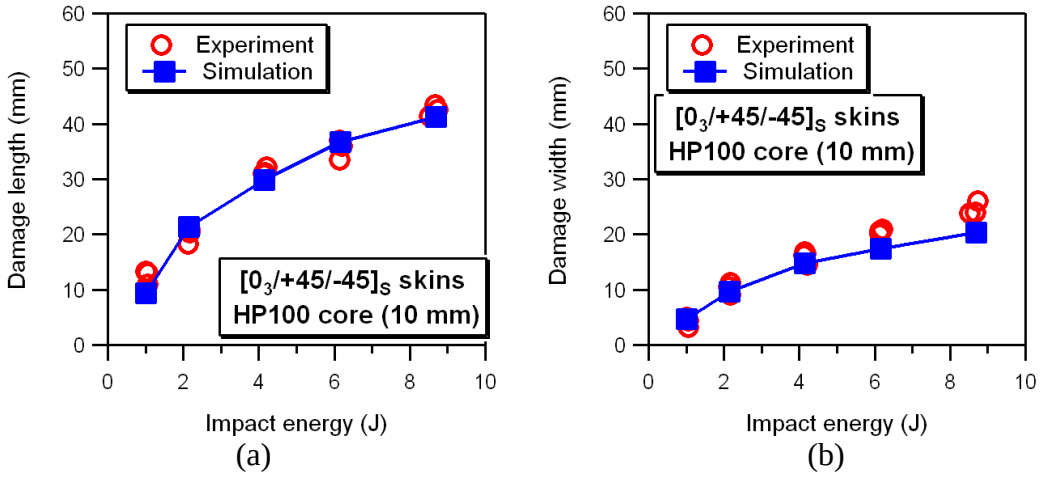

Figure 8-17: Comparison between measured and predicted damage length (a) and damage width (b) for sandwich panels with HP100 core.

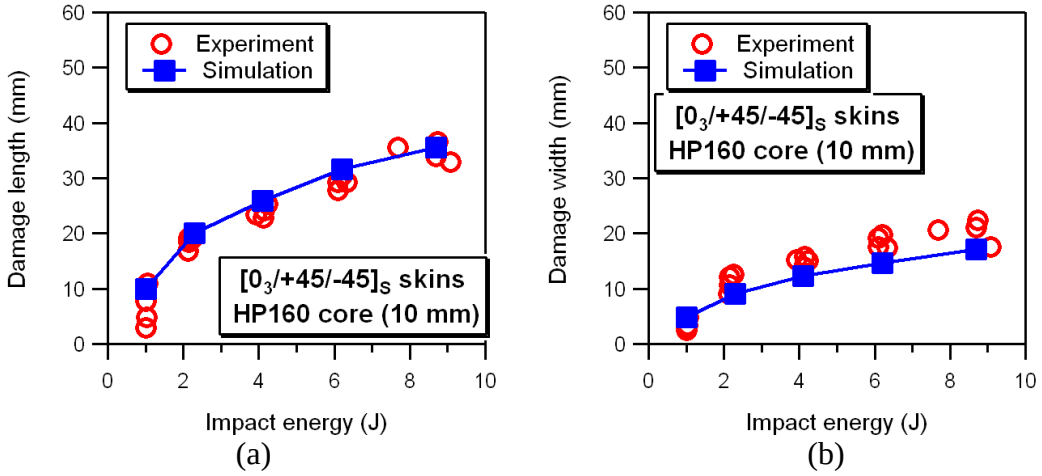

Figure 8-18: Comparison between measured and predicted damage length (a) and damage width (b) for sandwich panels with HP160 core.

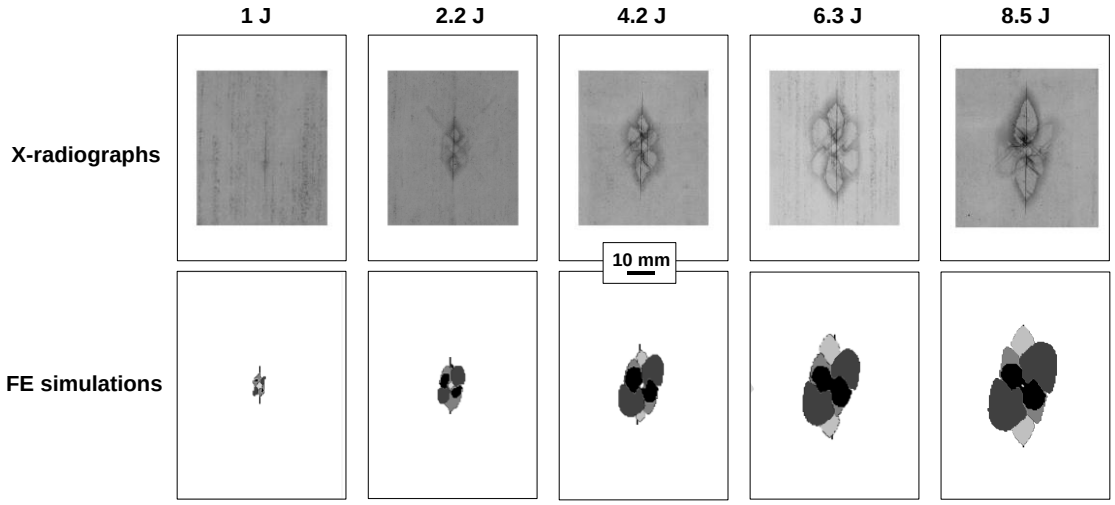

Figure 8-19: Comparison between experimental and predicted impact damage (different gray levels correspond to different delamination depths) in HP60 sandwich panels for five impact energies.

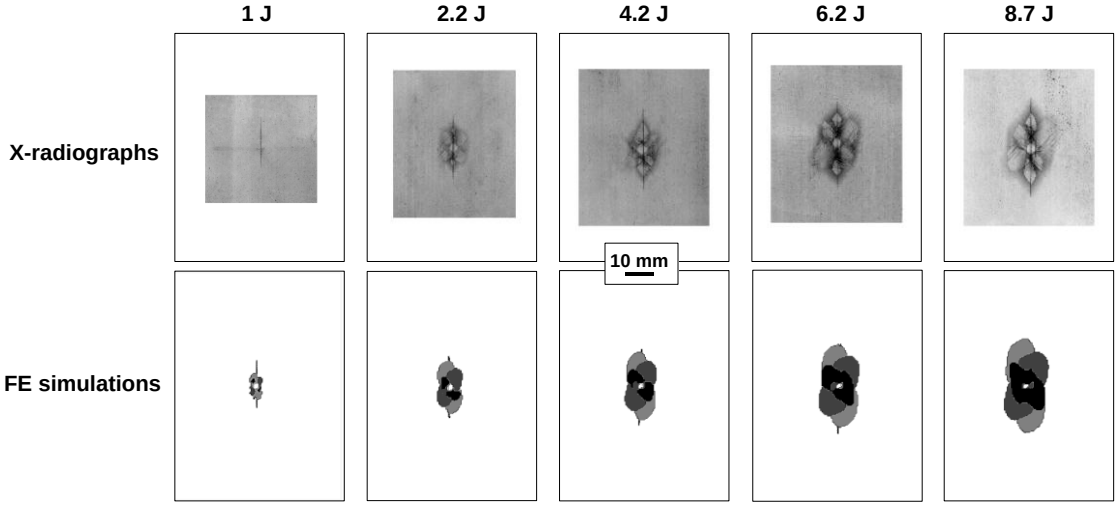

Figure 8-20: Comparison between experimental and predicted impact damage (different gray levels correspond to different delamination depths) in HP160 sandwich panels for five impact energies.

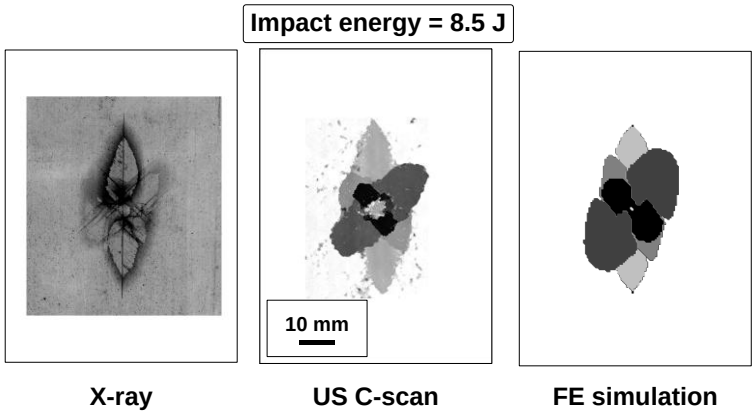

Figure 8-21: Comparison between X-radiograph, ultrasonic C-scan and predicted damage areas for [0_3/+45/-45]s sandwich panels with HP60 core impacted at 8.5 J.

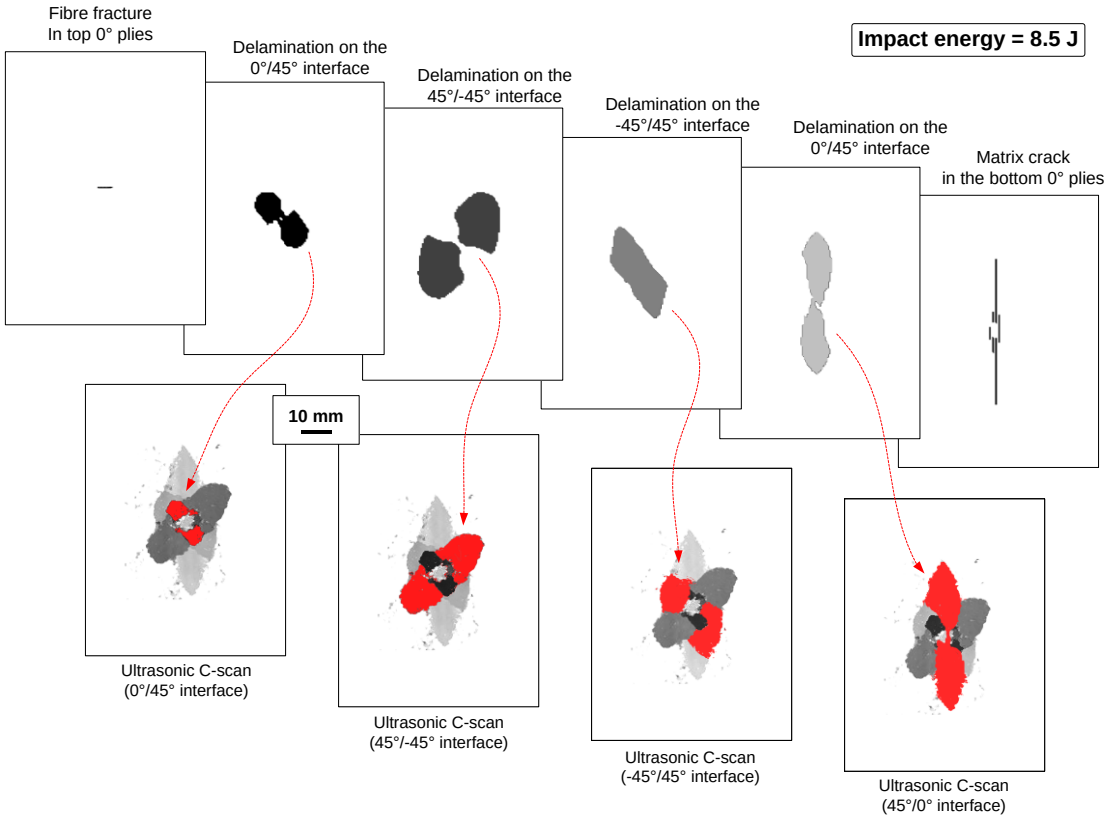

Figure 8-22: Through-thickness distribution of main damage modes as predicted by FE model and constructed by ultrasonic C-scans for [0_3/+45/-45]s sandwich panels with HP60 core impacted at 8.5 J.

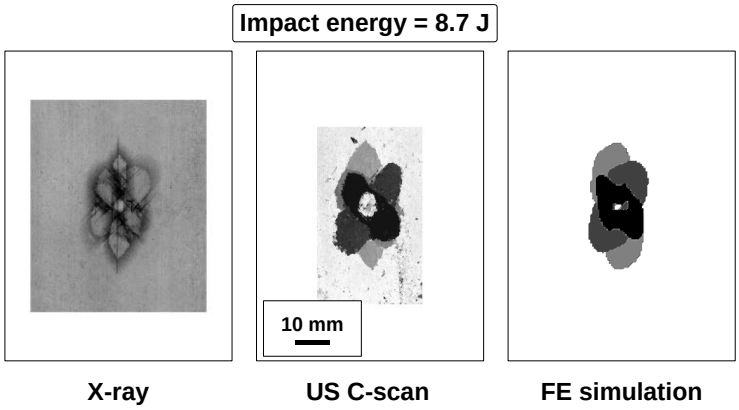

Figure 8-23: Comparison between X-radiograph, ultrasonic C-scan and predicted damage areas for [0_3/+45/-45]s sandwich panels with HP160 core impacted at 8.7 J.

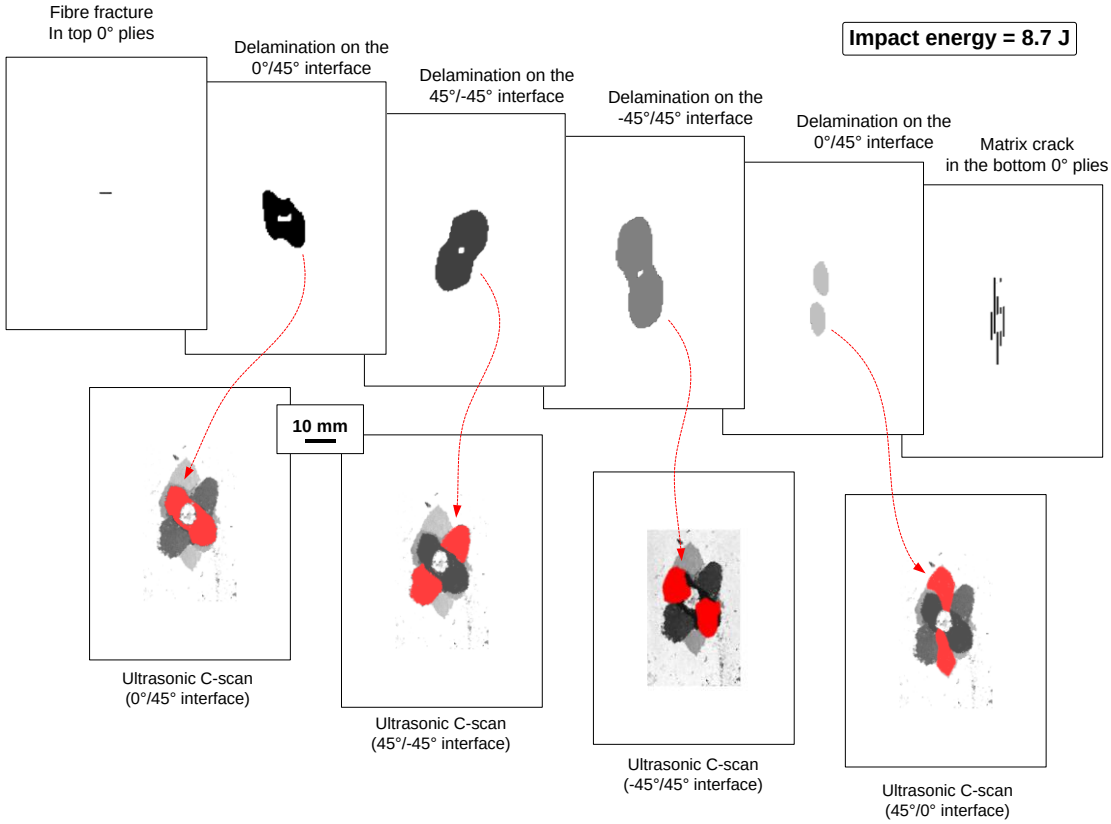

Figure 8-24: Through-thickness distribution of main damage modes as predicted by FE model and constructed by ultrasonic C-scans for [0_3/+45/-45]s sandwich panels with HP160 core impacted at 8.7 J.

Figure 8-21 and **Figure 8-23** shows an example of comparison between X-radiographs, ultrasonic C-scans and predicted delaminated areas, with HP60 and HP160 sandwich panels respectively. Detailed through-thickness distributions of main damage modes predicted by the FE model in the laminated skin of $[0_3/+45\text{-}45]_S$ sandwich panels with HP60 and HP160 foam cores are compared with those constructed by ultrasonic C-scans, as shown in **Figure 8-22** and **Figure 8-24**.

A good agreement is observed between numerical results and experiments for different foam densities. In agreement with the internal damage scenario that was reconstructed through X-radiography and ultrasonic observations, FE models simulate with reasonably good accuracy the size, shape and through-thickness location of delaminations at each interface; the characteristic two-lobe shapes of individual delaminations, with the axis oriented along the fibre direction of the lower adjacent layer, and the three-dimensional arrangement of delaminated areas resulting in a typical spiral staircase pattern, are successfully predicted by the FE tool. The FE models also correctly predict the development of bending matrix cracking in bottom 0° layers and minor fibre fracture in top 0° plies.

As illustrated in the graph of **Figure 8-25**, which shows an example of individual damage modes predicted at various stages during an 8.5 J impact on an HP60-based panel, the FE model is also able to simulate correctly the succession of the major damage events occurring under increasing impact loads.

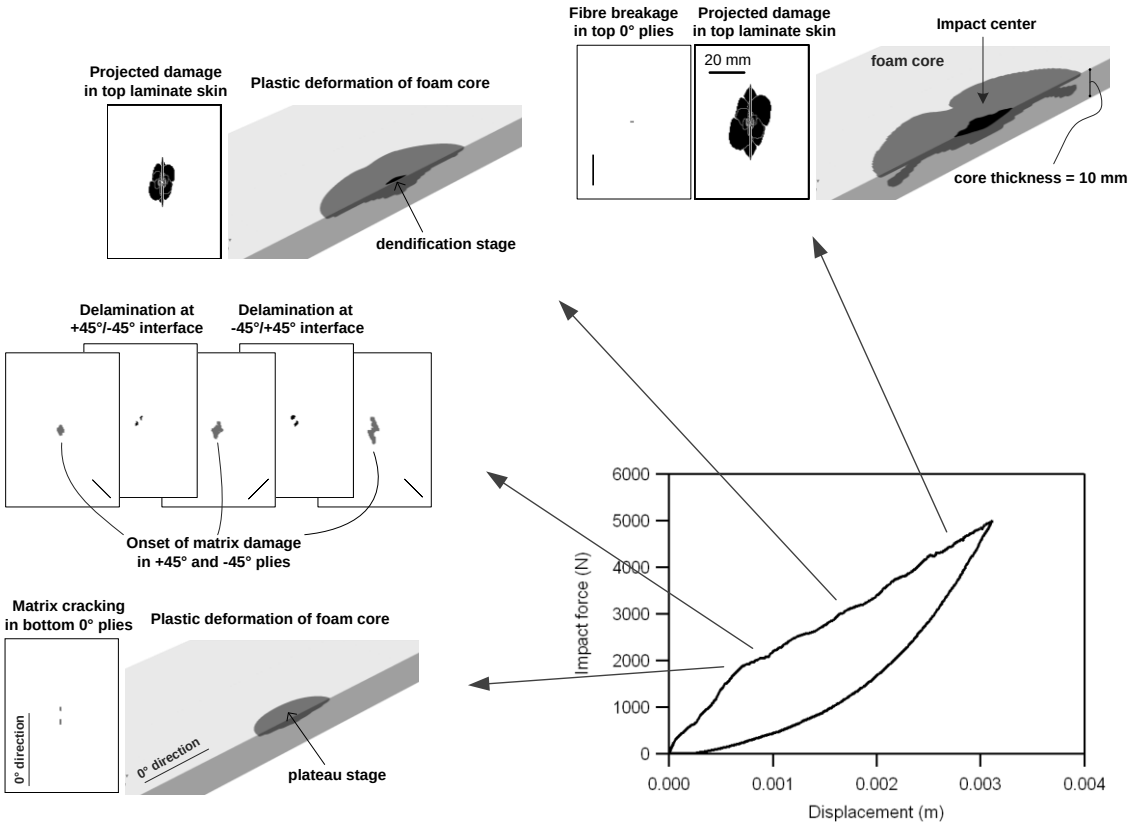

Figure 8-25: Sequence of damage events predicted by the FE model for a 8.5 J impact on a $[0_3/+45/-45]_S$/HP60 sandwich panel.

As shown in **Figure 8-25**, very little damage of the composite skins (a small bending matrix crack in the bottom 0° layers) is predicted by the FE model at a load of 2 kN; the numerical simulations indicate however the initiation of plastic deformation of the foam core (reaching the plateau stress of the stress-strain curve) at that load level, These results appear to confirm the evidence provided by experimental observations, that suggest that foam crushing plays a major role in the noticeable stiffness drop recorded during the impact event upon reaching the knee load level. Soon after the knee point, delaminations initiate to develop at the +45°/-45° and -45°/+45° interfaces; with increasing load, the FE model simulates the development and subsequent growth of delaminations at remaining interfaces, together with associated matrix damage in 0° and

±45° layers. A small volume of foam core enters the densification stage at a load level of about 3 kN, causing the slight stiffness increase after that. Localized fibre fracture, which may be possibly related to the small stiffness reduction exhibited at high loads by the force-displacement curve, is finally predicted on the indentation area of the top 0° layers for a load of about 4.5 kN. In accordance with experimental findings, no delamination is predicted by the model at the interface between core and facesheet over the entire impact energy range investigated.

8.3 Concluding Remarks

Low-velocity impacts on sandwich panels with multidirectional laminate skins ($[0_3/+45/-45]_S$) and three different foam cores (HP60, HP100 and HP160) were simulated. Comparisons between numerical and experimental results were carried out for various impact energy levels. Good agreement is again obtained between predictions and experiments not only in terms of structural response (force histories, force-displacement curves and absorbed energies), but also in terms of internal damage (temporal sequence of major damage events; projected damage shapes, sizes and through-thickness distributions).

CHAPTER 9

IMPACTS ON SANDWICH PANELS WITH DIFFERENT CONFIGURATIONS

The developed FE tool was also applied to simulate impacts on sandwich panels with different configurations (different core thickness, panel size and boundary condition) to further evaluate the accuracy of predictions and the application range of the model.

9.1 Impacts on Sandwich Panels with Different Core Thickness

The performance of the FE tool was further assessed by comparing the results of the numerical analyses to experimental impact data obtained on $[0_3/+45/-45]_S$/HP60 sandwich panels with a core thickness of 40 mm.

9.1.1 Analysis of Experimental Results

The structural responses to impact of sandwich composites with 10 mm and 40 mm HP60 foam cores, as characterized by the force vs time and force vs displacement curves for an impact energy of about 8.5 J, are compared in the graphs of **Figure 9-1**. It is evident that increasing the core thickness from 10 to 40 mm has a limited effect, for the support conditions adopted in the experiments, on the localized response to impact, with 40 mm core panels only exhibiting a slight reduction in the slope of the force-displacement curve as compared to 10 mm core panels. X-radiographic inspections also show that the extent, features and through-thickness distribution of the damage

mechanisms induced by impact in the laminated skins are not significantly influenced, in the examined range, by the thickness of the core.

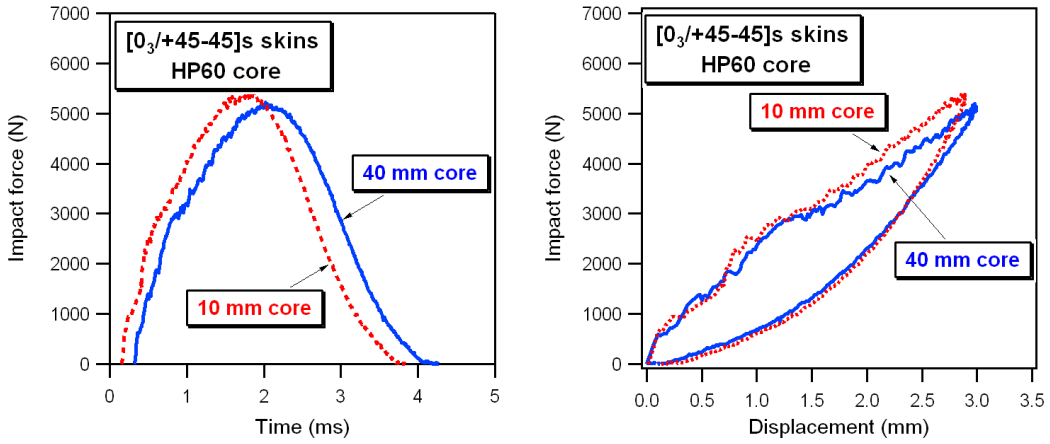

Figure 9-1: Comparison of force-time (a) and force-displacement (b) curves for $[0_3/+45/-45]_S$ sandwich panels with 10 mm and 40 mm thick HP60 cores.

9.1.2 Comparison between Simulations and Experiments

FE simulations are compared with the results obtained during the experimental tests for sandwich panels with 40 mm-thick core in the **Figure 9-2** - **Figure 9-4**.

It's seen that both force-time histories and force-displacement relationships (**Figure 9-2**) are simulated with reasonable accuracy by the model over the whole span of investigated impact energies, even though the FE analyses appear to slightly overestimate the stiffness reduction produced by damage for high impact energies. As visible in the plots of **Figure 9-3**, the results of the FE analyses are also in good agreement with the values of peak contact forces and absorbed energies experimentally measured during the impact tests. Similarly, the graphs of **Figure 9-4** show that the predictions of the model are in very good agreement with the experimental results with regard to the various

metrics indicators used to describe the main damage features (projected damage area, damage length and damage width).

A qualitative validation of the predictive capabilities of the model is further illustrated in **Figure 9-5**, which shows, for the whole range of impact energies investigated , the good correspondence between the projected delamination pattern as predicted by FE calculations and the actual internal damage as experimentally obtained by X- radiography.

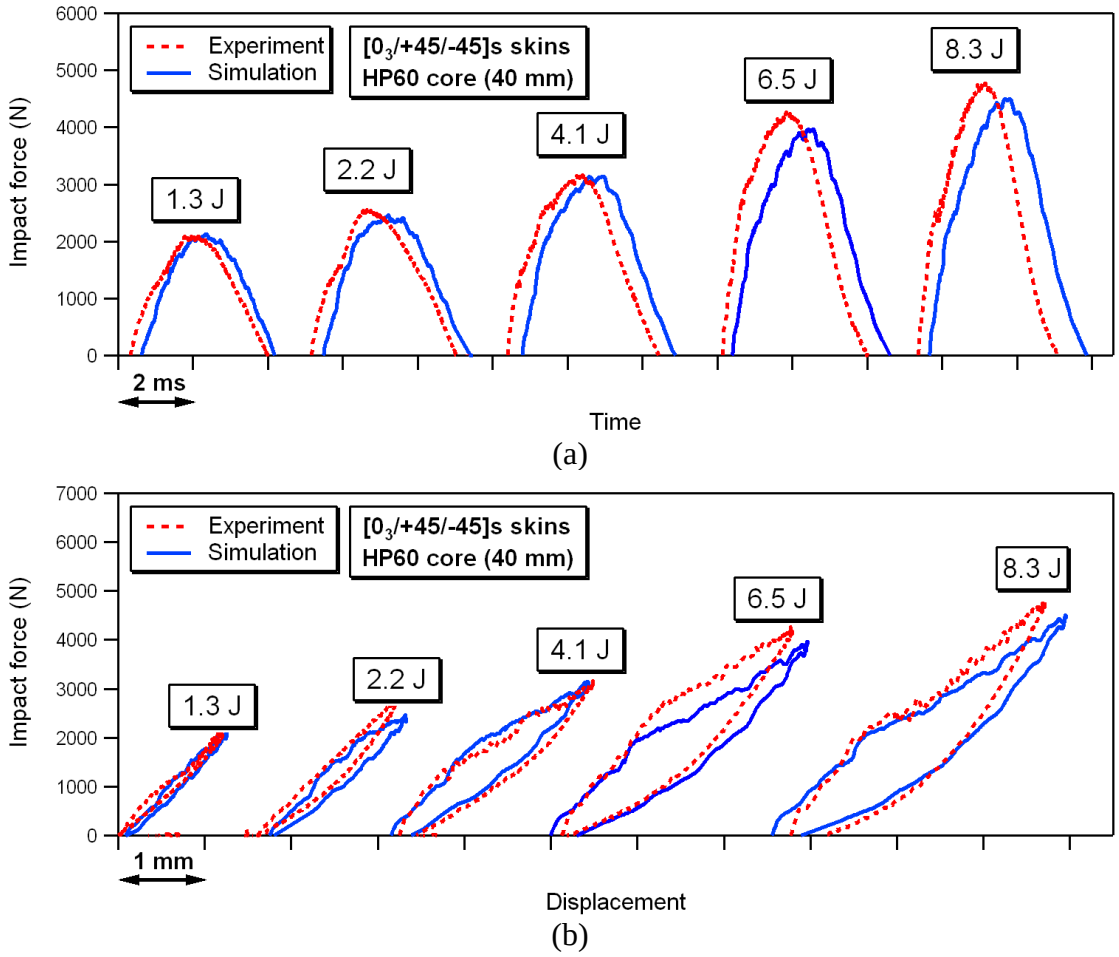

Figure 9-2: Comparison between predicted and experimental force-time (a) and force-displacement (b) curves for sandwich panels with 40 mm thick HP60 core.

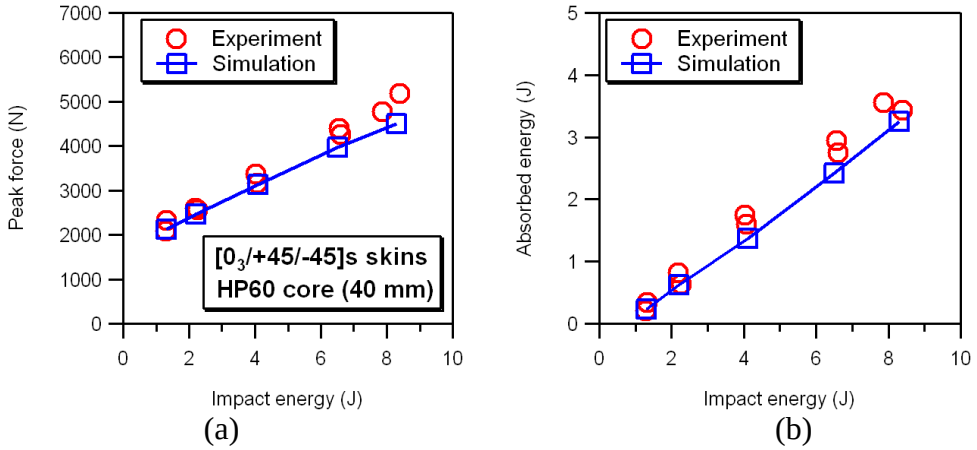

Figure 9-3: Comparison between predicted and measured peak contact forces (a) and absorbed energies (b) for sandwich panels with 40 mm HP60 core.

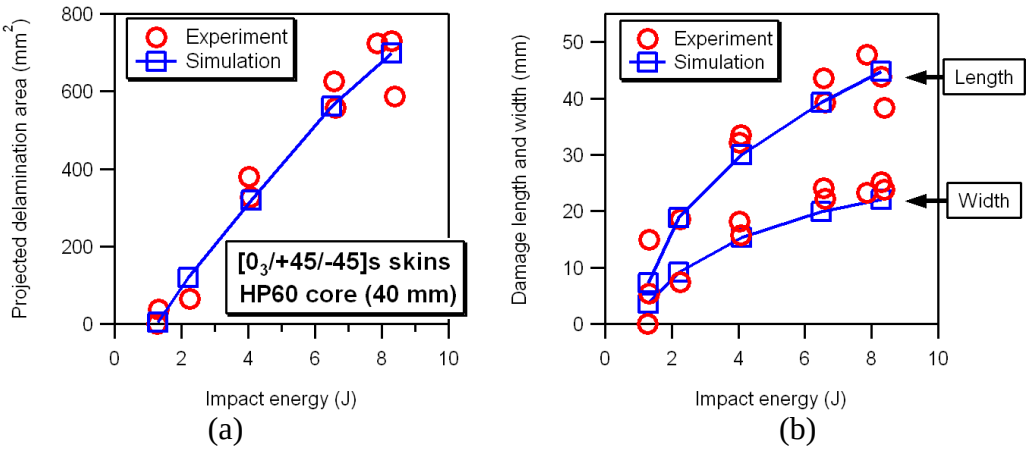

Figure 9-4: Comparison between predicted and measured projected delamination area (a) and damage length and width (b) for sandwich panels with 40 mm HP60 core.

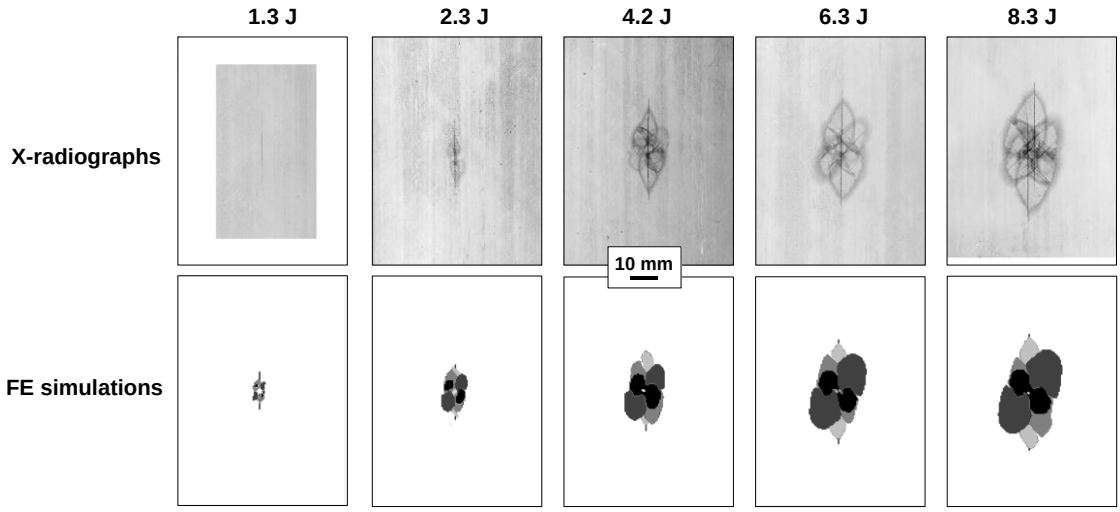

Figure 9-5: Comparison between experimental and predicted impact damage in an HP60 sandwich panel with 40 mm thick core subjected to five impact energies.

9.2 Impacts on Sandwich Panels with Different Boundary Condition

The quality of the predictions achieved by the developed FE tool has been further assessed and validated against experimental results from a series of impact tests carried out on sandwich plates of a larger structural size (350 mm x 350 mm) and different boundary condition, as compared to those illustrated in the previous sections.

9.2.1 Test Configuration and FE Model

In particular, the experimental data collected during impact tests on 350 mm x 350 mm panels with $[0_3/+45/-45]_S$ skins and with 20 mm-thick HP60 or HP160 foam core was used for comparison with the results of FE simulations. The panels were simply supported along two opposite sides parallel to the 0° direction and free over the other two edges (**Figure 9-6**). The support length at the edges of the panels is 25 mm, thus resulting

in an inner span of 300 mm. The sandwich panels were impacted at the center with energies ranging from 2 to about 6 J.

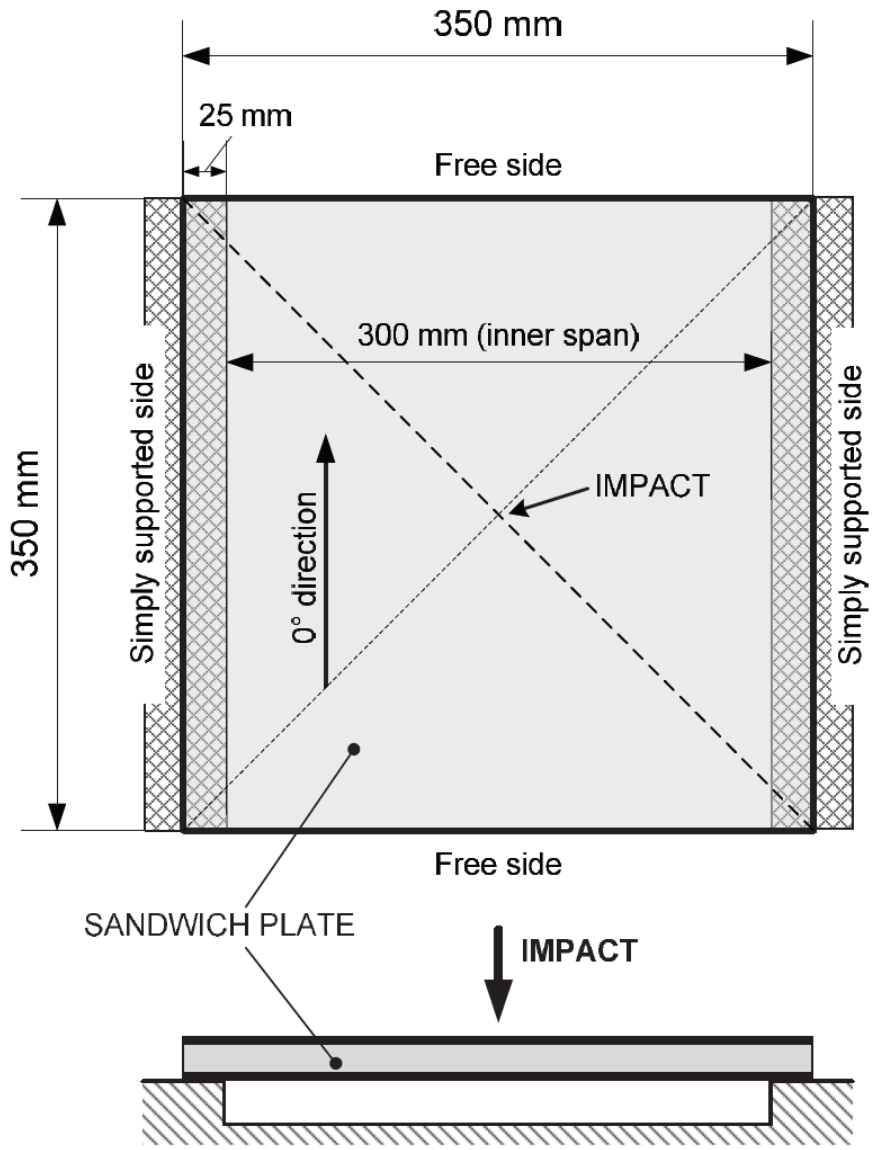

Figure 9-6: Geometry and boundary conditions of impacted 350 mm x 350 mm sandwich composites.

Figure 9-7 shows the FE model constructed for the numerical calculations. The same element size used for meshing the model of the smaller sandwich panels (0.5 mm × 0.5 mm in the plane of the laminated skins) was used in the fine region of the mesh.

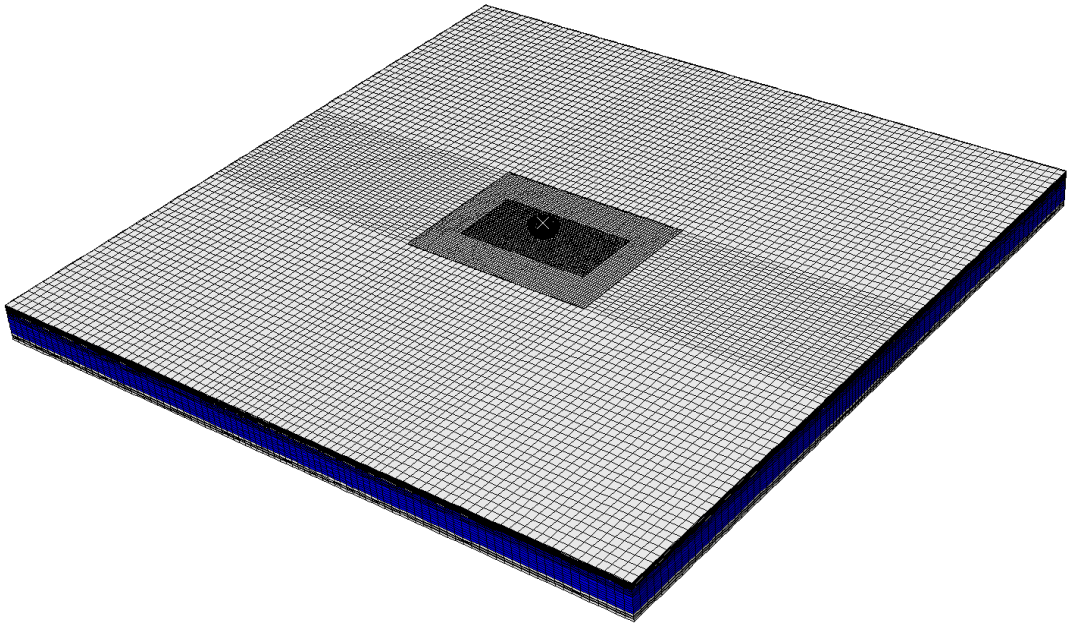

Figure 9-7: FE model of 350mm x 350 mm sandwich panels.

9.2.2 Comparison between Simulations and Experiments

Experimental and predicted force-time and force-displacement curves corresponding to impacts of different energy levels are compared in the graphs of **Figure 9-8** and **Figure 9-9**, for sandwich panels with HP60 and HP160 foam cores, respectively. As visible in these graphs, the impact behaviour of the sandwich composite is strongly affected by the elastic reaction of the whole sandwich structure, and the force-time and force-displacement curves may be seen as the result of the complex combination of the localized response to indentation, the global elastic response of the panel, and the dynamic interaction between the impactor, the target panel and the surfaces of the supporting fixture (Castanié, et al. 2008). In spite of the complexity of the problem, the plots of **Figure 9-8** and **Figure 9-9** show that an acceptable agreement is achieved

between FE simulations and experiments in terms of force-time histories and force–displacement responses for the sandwich configurations with the different foam densities.

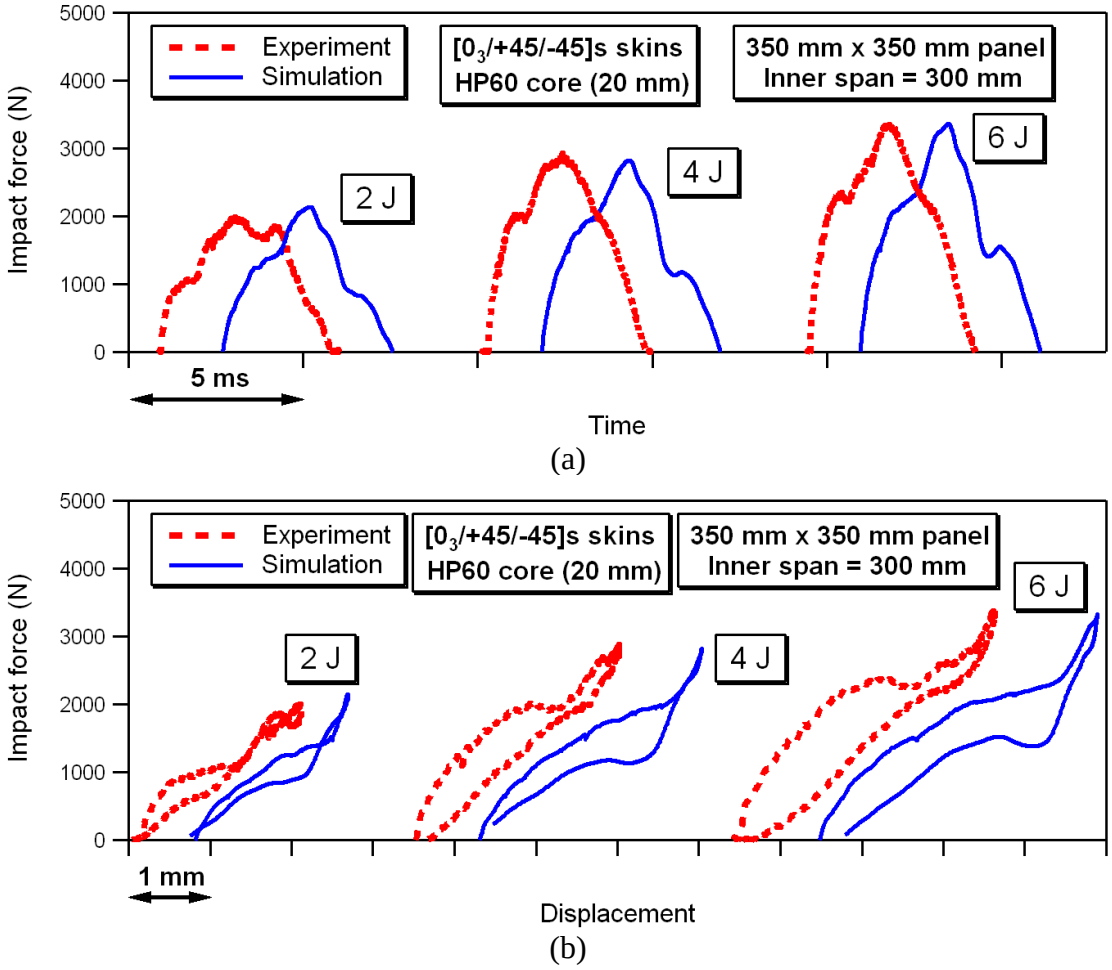

Figure 9-8: Comparison between predicted and experimental force-time (a) and force-displacement (b) curves for 350mm x 350 mm sandwich panels with HP60 foam core. Core thickness = 20 mm.

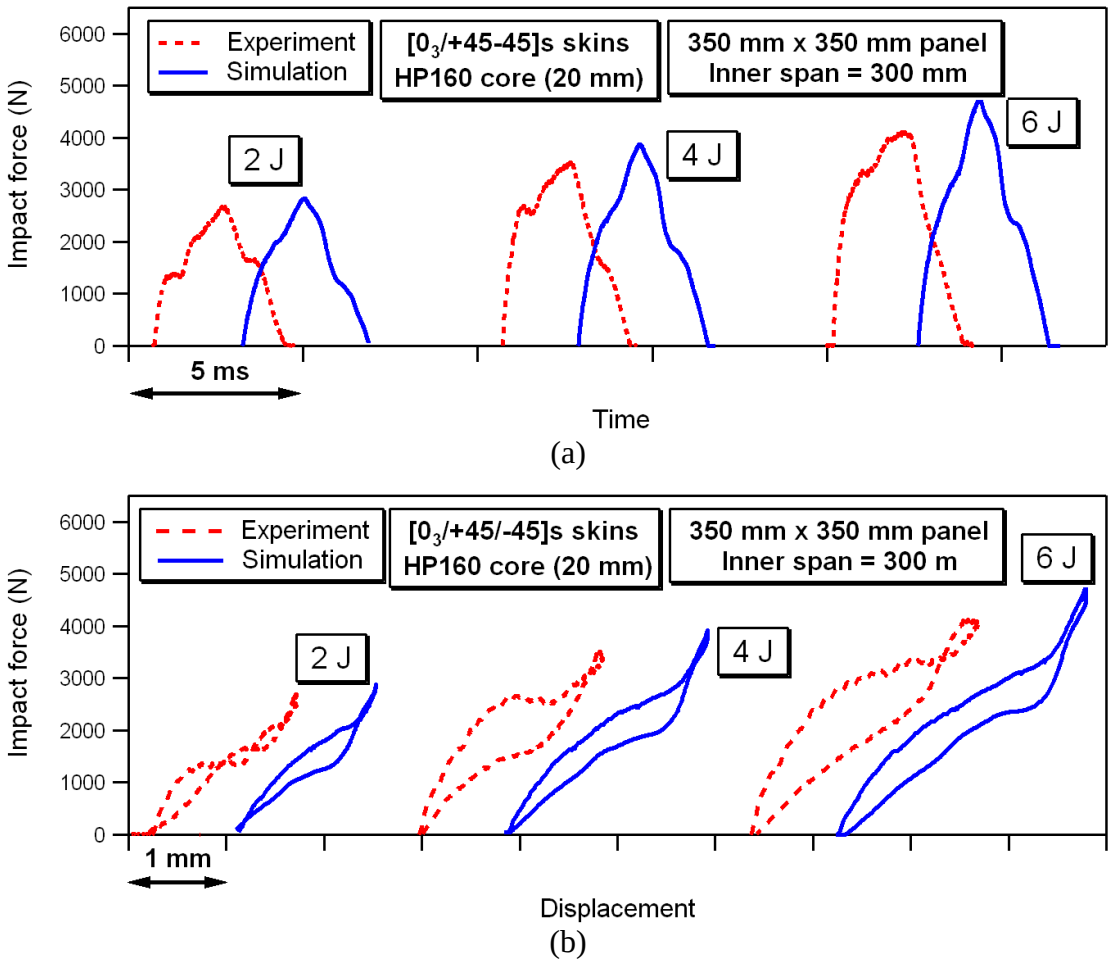

Figure 9-9: Comparison between predicted and experimental force-time (a) and force-displacement (b) curves for 350mm x 350 mm sandwich panels with HP160 foam core. Free span = 300 mm.

Comparisons of simulated and experimental peak forces and absorbed energies at various impact energies are reported in the plots of **Figure 9-10** and **Figure 9-11**, which show that there is an acceptable match between predictions and experiments in terms of maximum contact force and energy dissipated by the panels during the impact.

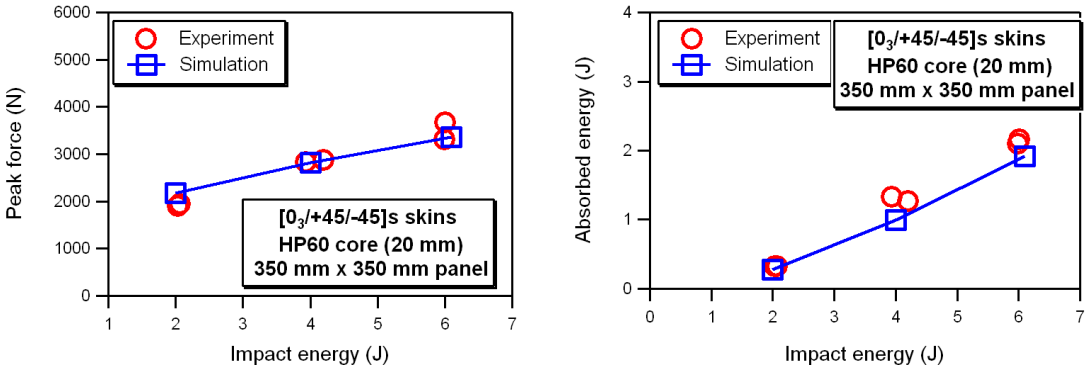

Figure 9-10: Comparison between predicted and measured peak contact forces (a) and absorbed energies (b) for a 350 mm x 350 mm sandwich panels (HP60 foam core) simply supported on a 300 mm span.

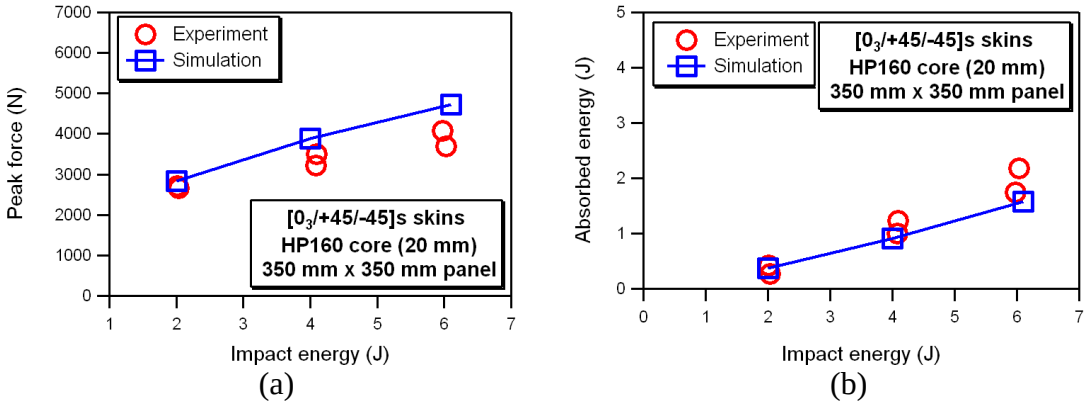

Figure 9-11: Comparison between predicted and measured peak contact forces (a) and absorbed energies (b) for 350 mm x 350 mm sandwich panels (HP160 foam core) simply supported on a 300 mm span.

The damage sizes and maps reported in **Figure 9-12** - **Figure 9-15** show that the model provides again damage predictions that are in generally good agreement, both in terms of projected planar views and on a ply-by-ply basis, with damage sizes and features as obtained through experimental tests at various impact energies.

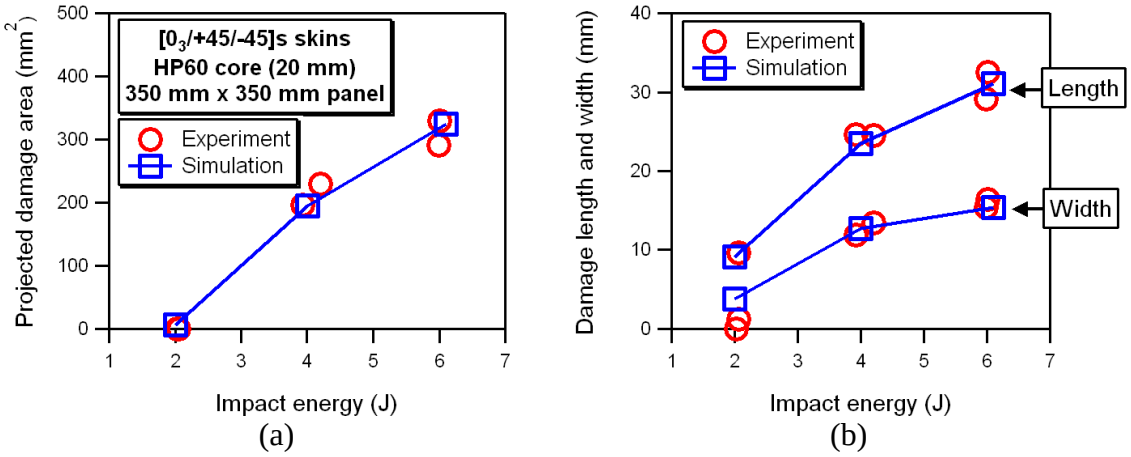

Figure 9-12: Comparison between predicted and measured projected delamination area (a) and damage length and width (b) for 350 mm x 350 mm sandwich panels (HP60 foam core) simply supported on a 300 mm span.

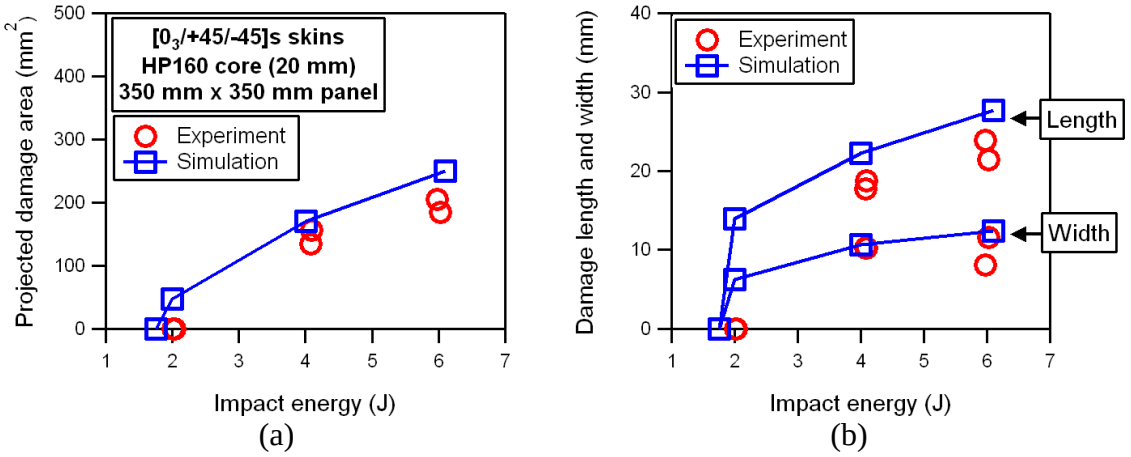

Figure 9-13: Comparison between predicted and measured projected delamination area (a) and damage length and width (b) for 350 mm x 350 mm sandwich panels (HP160 foam core) simply supported on a 300 mm span.

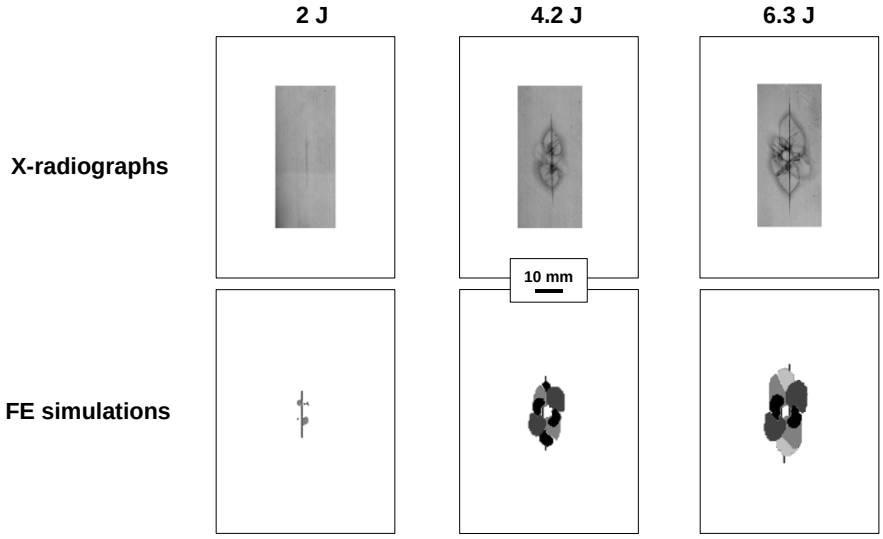

Figure 9-14: Comparison between experimental and predicted impact damage in 350 mm x 350 mm sandwich panels with HP60 foam cores subjected to three impact energies.

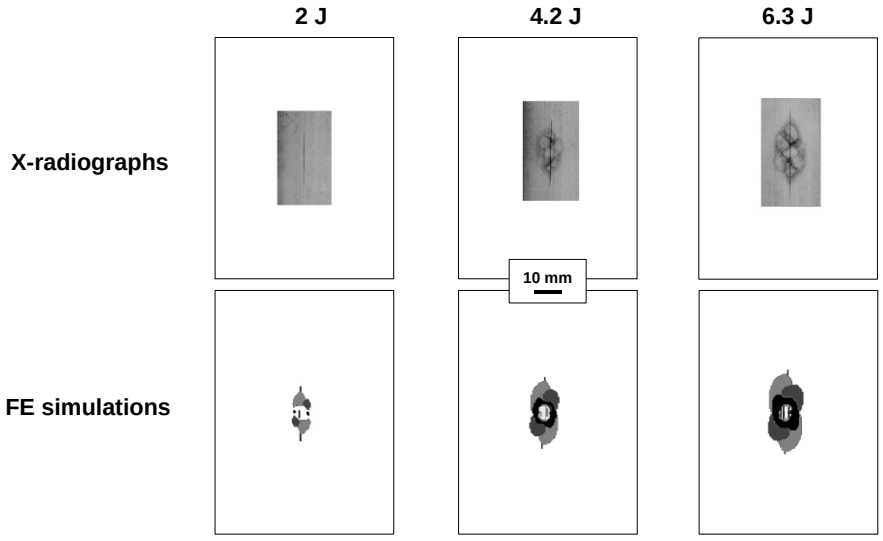

Figure 9-15: Comparison between experimental and predicted impact damage in 350 mm x 350 mm sandwich panels with HP160 foam cores subjected to three impact energies.

9.3 Concluding Remarks

The developed failure models were further applied to impact cases with different settings: different foam core thickness, different in-plane panel size and boundary condition. It is proved that the failure models are applicable to a wide range and show reasonably good prediction accuracy.

CHAPTER 10

ANALYSIS OF IMPACTS ON LAMINATES

The results in Chapter 7-9 show that the developed model is able to provide quite reliable numerical predictions for sandwich panels with various configurations. As a final investigation case, the developed damage models were applied to simulate low-velocity impact events on composite laminates, for which the structural response and the damage resistance may be quite different from those of sandwich composites, because of the lack of the supporting effect of the core material. (Foo, Chai and Seah 2008).

Moreover, additional numerical analyses were conducted to investigate how the implementation of intralaminar damage mechanism in the model affects the whole prediction accuracy of the model, in order to assess whether a simplified model only accounting for interlaminar damage (and thus requiring reduced computational resources as compared to the developed model) could provide damage prediction of sufficient quality for use in damage tolerance design procedures.

10.1 Simulation of Impacts on Laminates

The examined laminate plates have a 10 layer $[0_3/+45/-45]_S$ stacking sequence (the same with that adopted for the facesheets in a class of sandwich panels examined in Chapter 8) and a total thickness of 3.2 mm. The experimental setup of the impact test and

the finite element model reproducing the laminated plate are similar with the sandwich cases, as illustrated in **Figure 10-1**.

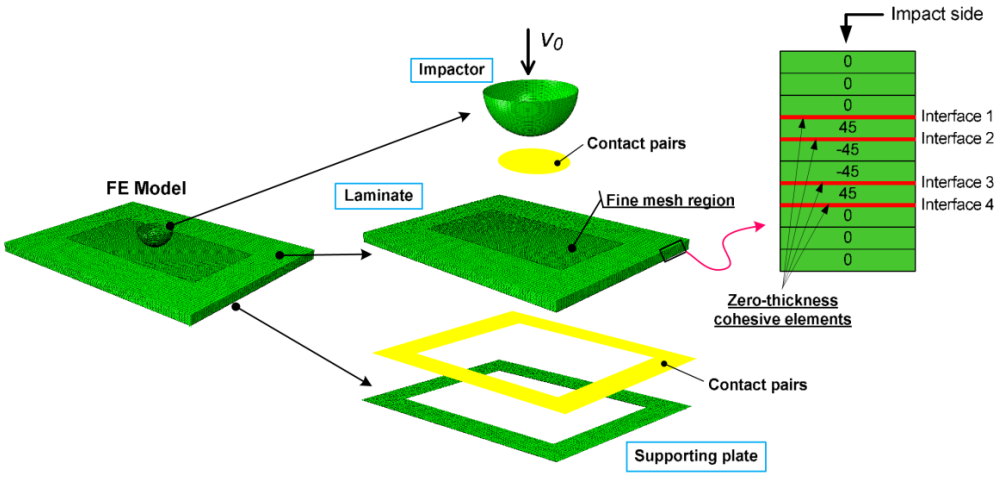

Figure 10-1: FE model of impacted laminate plate.

10.1.1 Structural Response

Figure 10-2 shows force vs. time and force vs. displacement plots as obtained by experimental tests and numerical simulations at various impact energy levels. It is seen that the computed results agree well with the experimental ones not only in duration of impact events but also in peak contact forces and absorbed energies (**Figure 10-3**), which are calculated as the area under the force-displacement curve and represent the total energy dissipated in irreversible damage phenomena (intralaminar or interlaminar fracture, matrix plasticity).

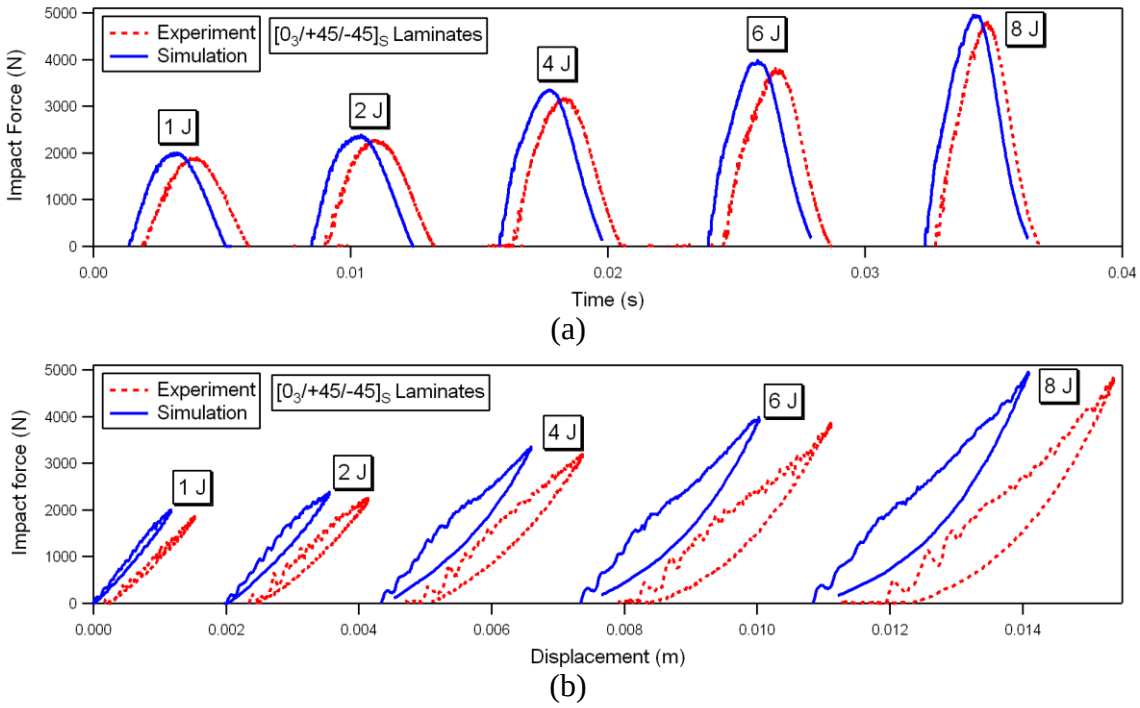

Figure 10-2: Comparison between experimental and numerical force-time (a) and force-displacement (b) curves for laminate panels.

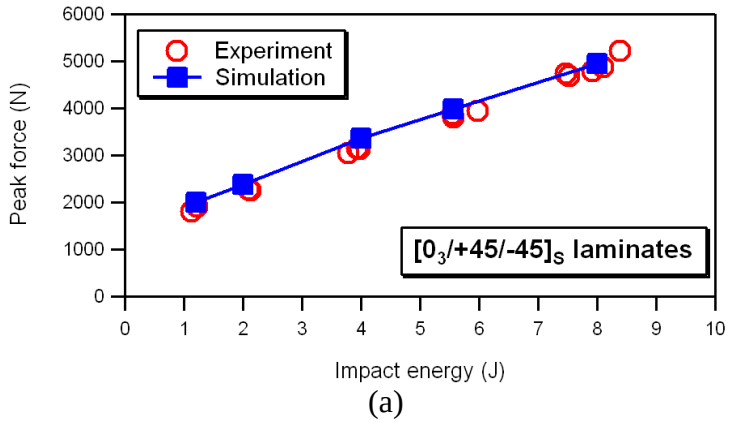

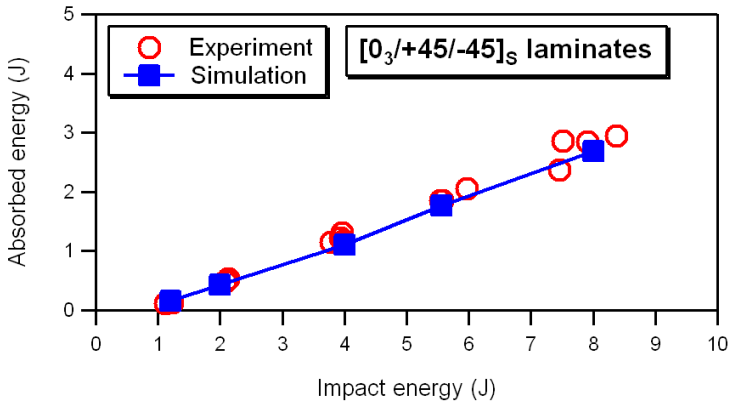

(b)

Figure 10-3: Comparison between experimental and predicted peak forces (a) and absorbed energies (b) for laminate panels.

10.1.2 Internal Damage

Figure 10-4 reports experimental and computed projected damage areas at different impact energy levels. The comparison shows that the model is able to reproduce the geometry of the projected damage area and its principal orientation along the 0° direction. A detailed examination of the damage distribution through the thickness of the composite laminates shows that predicted shapes and depth locations of damage areas qualitatively agree with the experimental observations, as obtained by X-ray analyses. The model is not only capable of reproducing the two-lobe geometry and the main orientation of individual damage areas at selected depths (**Figure 10-4**) but also able to predict with reasonable accuracy the damage sizes under various impact energies as shown in **Figure 10-5**.

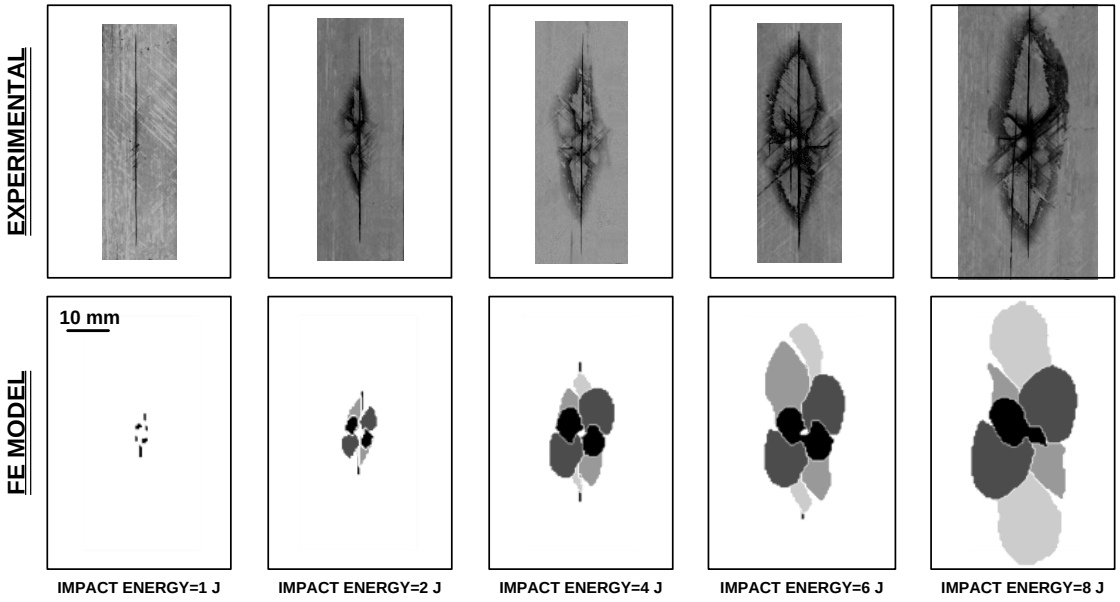

Figure 10-4: Comparison between projected damage areas as obtained by X-ray and predicted by FE model (different gray levels in plots indicate different damage depths).

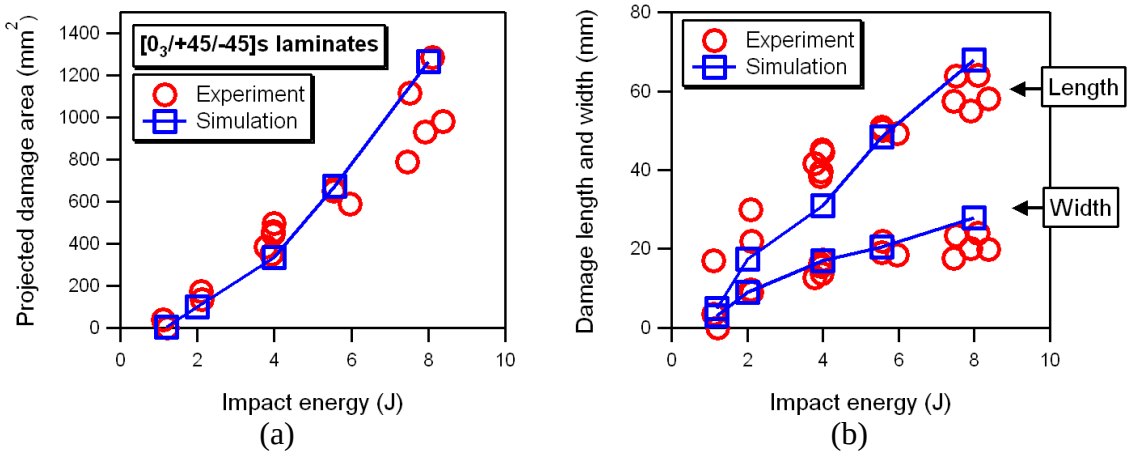

Figure 10-5: Comparison between predicted and measured projected delamination area (a) and damage length and width (b) for laminate panels.

As a final example, details of the various damage modes predicted by the FE model for an impact of 8 J are illustrated in **Figure 10-6**. It is seen that the FE model not only correctly predicts delaminations at individual interfaces, but, in agreement with

experimental observations, also simulates other peculiar features of internal damage, such as the major bending matrix crack in the lower 0° layers, diffuse in-ply matrix damage in ±45° layers, and localized fibre fracture at the contact area in the top 0° layers.

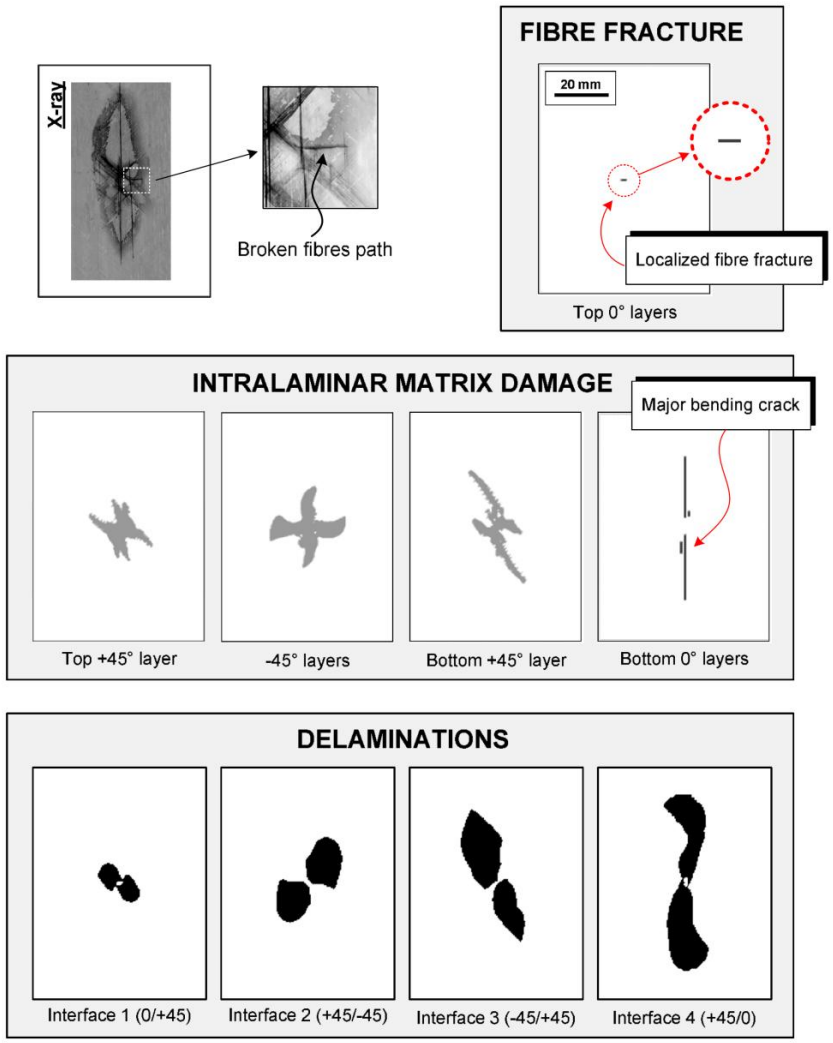

Figure 10-6: Interlaminar and intralaminar damage mechanisms predicted by the full FE model for impact energy of 8J.

10.2 Effect of Implementing In-ply Damage Modes on Prediction Accuracy

In order to assess the importance of modelling in-ply damage modes for an accurate simulation of impact events, numerical analyses were carried out using both the *full* FE model (which incorporates the simulation of both interlaminar and intralaminar damage modes) and a *reduced* FE model, where only delaminations –but not intralaminar damage mechanisms- were implemented in the calculations.

The impact force histories obtained by experimental tests and those predicted by the FE models both with and without simulation of intralaminar damage are compared in the graphs of **Figure 10-7** for three impact energies. Good agreement is observed between numerical results and experiments for simulations carried out with the full FE model, whereas peak loads somewhat higher than those measured experimentally are predicted by the reduced FE model.

The plots of **Figure 10-8** show experimental and numerically predicted force-displacement curves for the same energy levels examined in the graphs of **Figure 10-7**. We note that the force displacement curves simulated by the full FE model show a reasonably good match with the experimental observations in both the loading and unloading stages. The full FE model correctly reproduces peculiar features of the impact response of the laminates, such as the decrease in stiffness observed during the experiments at a load level of about 2 kN and the sudden drop in force (associated to growth of fibre fracture) recorded at a peak load of 4.6 kN during the 8 J impact test. In comparison to the full FE model, the simulations of the reduced FE model still capture the general shape of the force-displacement curve, even though both the slope of the

curve and the load level at which the curve exhibits a significant stiffness drop appear slightly higher than those predicted by the full FE model.

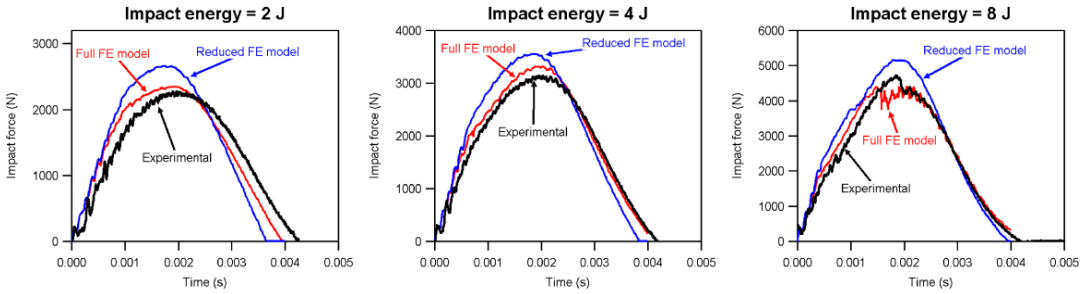

Figure 10-7: Comparison between experimental and numerically predicted force-time histories.

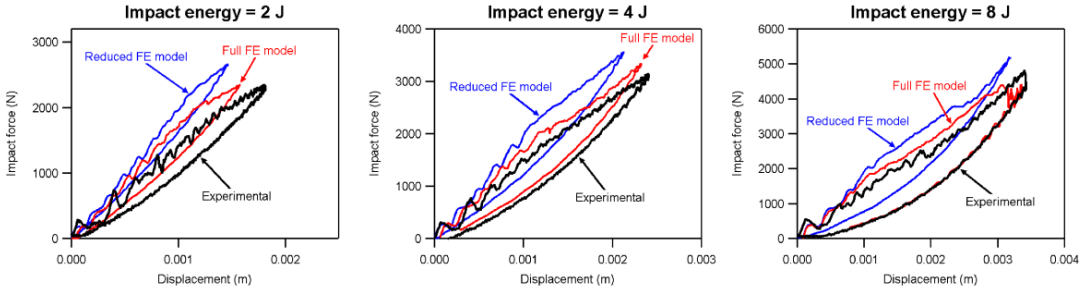

Figure 10-8: Comparison between experimental and numerically predicted force-displacement curves.

The impact energy-time relationship is represented in **Figure 10-9**. Following the initial contact, the kinetic energy of the impactor is transferred to the laminate in two forms: one is stored as elastic energy in the material and the other is dissipated as irreversible damage phenomena, including intralaminar and interlaminar damage, and material nonlinearities. The kinetic energy of the impactor is totally transformed to the laminate when its velocity reduces to zero; afterwards, the elastic energy stored in the laminate is transferred back to the impact, causing its upward rebound. The difference between the kinetic energy of the impactor immediately before the impact and that

measured at the rebound represents the total energy dissipated during the impact event. As indicated by the experimental tests illustrated in **Figure 10-9**, the absorbed energy is about 0.49 J for an impact of about 2 J, while the full and reduced FE models predict absorbed energies of 0.44 J and 0.28 J, respectively. It is thus evident that better accuracy can be achieved on the prediction of energy dissipation when the intralaminar damage is taken into account by FE model. Similar conclusions can be drawn for higher energy levels, as shown by **Figure 10-9** for 4 J and 8 J impacts.

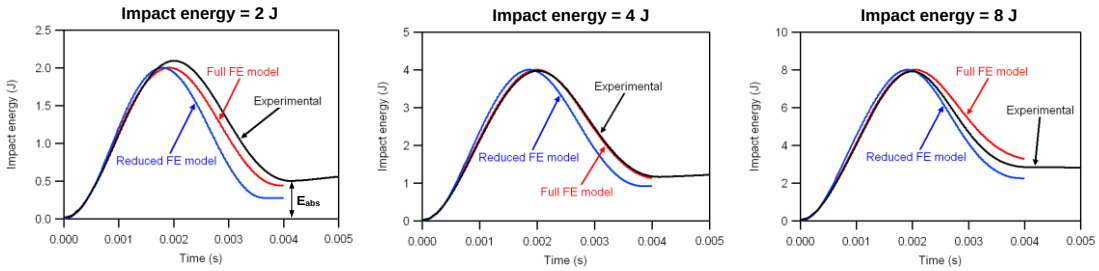

Figure 10-9: Comparison between experimental and numerically predicted histories of energy absorbed by the laminate panel.

Figure 10-10 shows comparisons of peak contact forces and absorbed energies obtained by experimental tests and calculated by the FE models over the entire range of impact energies investigated. The plots show that a general good agreement is achieved between the experiments and the simulated impact behaviour, whether predicted by the full FE model or by the reduced FE model, with only a slight tendency of the reduced FE model to overpredict peak force values and underpredict dissipated energies, especially at the highest impact energy levels. It may be worth remarking that the stiffer laminate response and smaller energy dissipation predicted by the reduced FE model as compared to the full FE model are not unexpected, since intralaminar damage mechanisms and their effect on the laminate behaviour are only taken into account in the full FE model analyses.

As an example, fibre fracture energy dissipation of almost 20% of the total absorbed energy is estimated using the full FE model for an impact energy of 8 J.

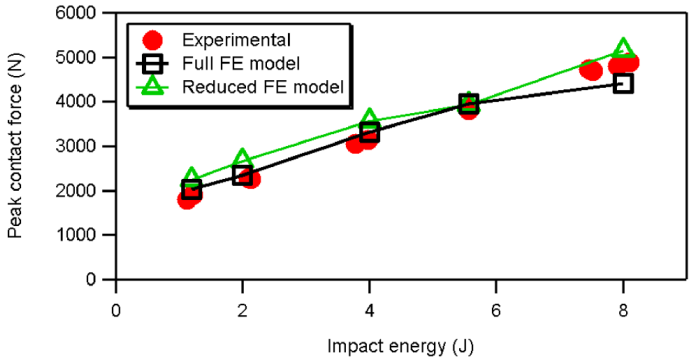

(a)

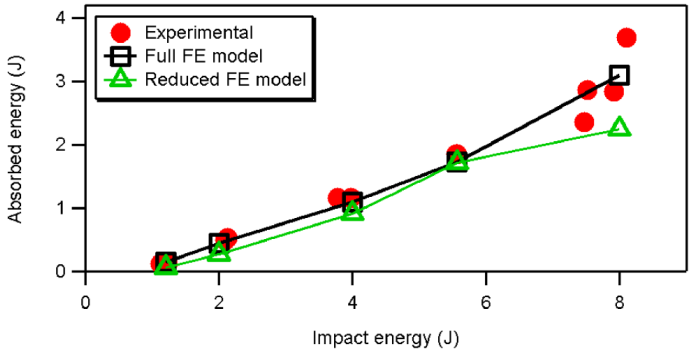

(b)

Figure 10-10: Comparison between experimental and predicted peak contact forces (a) and absorbed energies (b).

Comparisons between experiments and simulations in terms of damage developing in the laminated plates at different impact energies are illustrated in **Figure 10-11**-**Figure 10-14**.

Figure 10-11 shows images of projected impact damage as obtained by X-radiography and as predicted by FE calculations. Both the full and the reduced FE models are capable of capturing the elongated shape of the projected damage area, with its major axis oriented along the 0° direction. More quantitative comparisons between simulated

and experimental results are presented in the graphs of **Figure 10-12**, where projected damage areas, as well as width and height of the damaged area are plotted as a function of impact energy. It is seen that the two FE models are able to capture with reasonable accuracy the length and the width of the damaged area (**Figure 10-12**b), while the size of the projected damage area, which is correctly predicted by the full FE model, is clearly overestimated by the reduced FE model for impact energies above 4 J (**Figure 10-12**a).

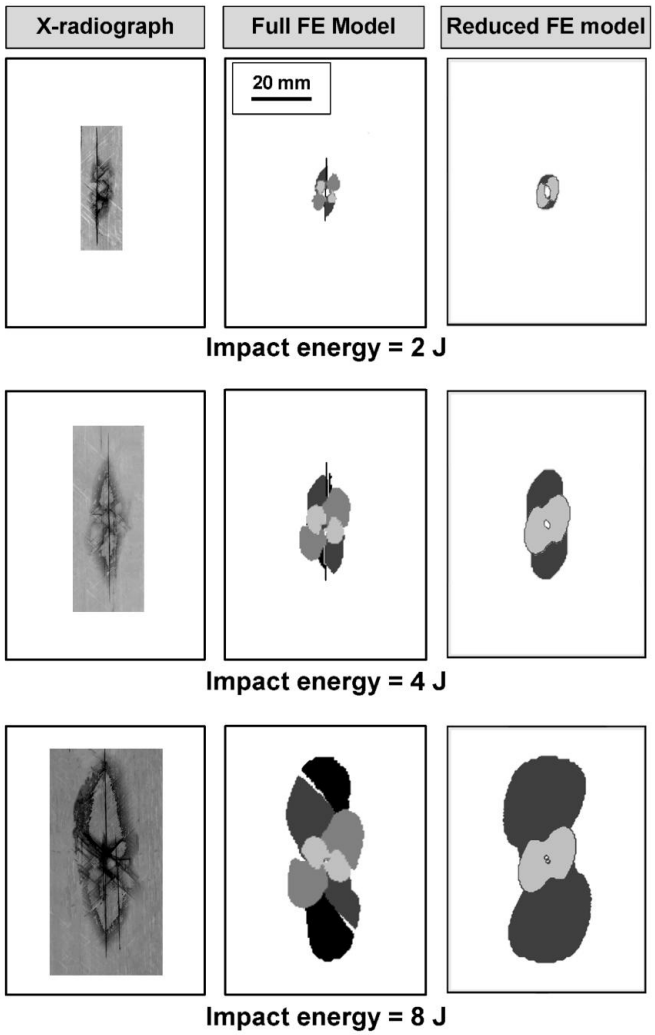

Figure 10-11: Comparison between projected damage areas as obtained by X-ray and FE models at various impact energies; different levels in numerically predicted damage areas correspond to different damage depths.

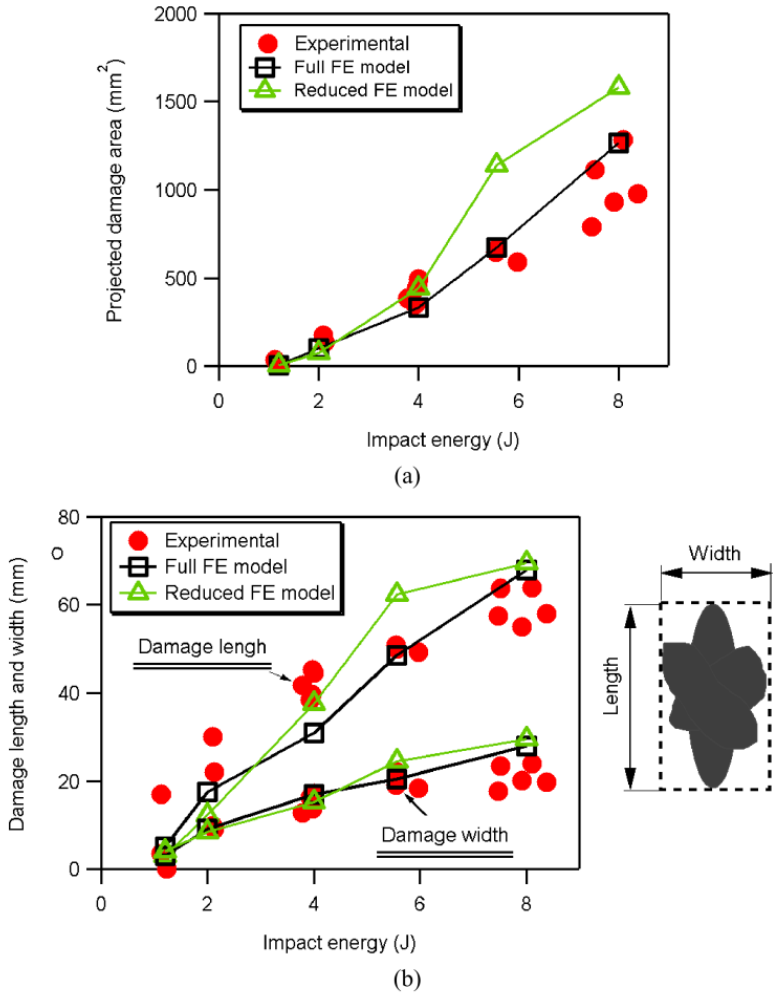

Figure 10-12: Comparison between experimental and predicted projected damage area (a) and damage length and width (b).

To evaluate in more detail the predictive capabilities of the two FE models, the experimental delamination patterns, as reconstructed three-dimensionally by combining information acquired through stereoscopic X-radiography and micrographic analyses, were compared to those simulated by the models at different impact energies. As an example, the illustration of **Figure 10-13** shows experimental and numerically predicted delamination maps at different depths for an impact energy

of 5.6 J. We may see that while the full FE model correctly captures the main features of individual delaminations (characterized by a typical two-lobe geometry, with the main axis oriented along the fibre direction of the lower layer) at all four damage-prone interfaces, the reduced FE model only predicts the development of delaminations at the 1st (0°/+45°) and 3rd (-45°/+45°) interfaces from the impact side.

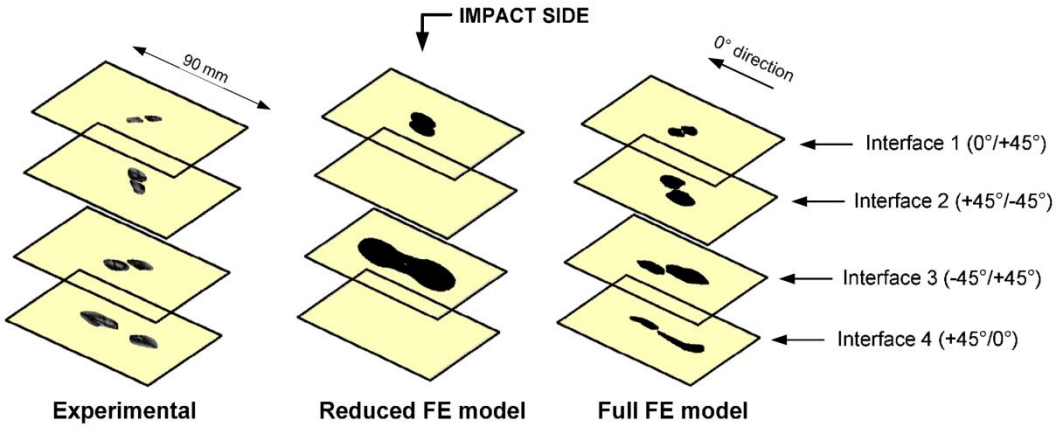

Figure 10-13: Through-thickness distribution of delaminated areas as reconstructed by stereoscopic X-radiography and predicted by FE models for impact energy of 5.6J.

Further comparisons between experimental and simulated delaminated areas at each interface are presented in the plot of **Figure 10-14** for the complete range of impact energies. We may observe that while the full FE model provides a reasonable estimation of the growth of the four delaminated areas under increasing impact energies, the reduced FE model fails –as anticipated above- to predict the onset and development of delaminations at the 2nd and 4th interfaces, and largely overpredicts delamination sizes at the 1st and 3rd interfaces. The results of the calculations suggest, therefore, that even if the structural impact response may be predicted with acceptable accuracy without including intralaminar damage models in the FE code,

implementation of intralaminar damage mechanisms in the FE analyses may be required for a correct simulation of extent and through-thickness location of individual delaminations induced by impact.

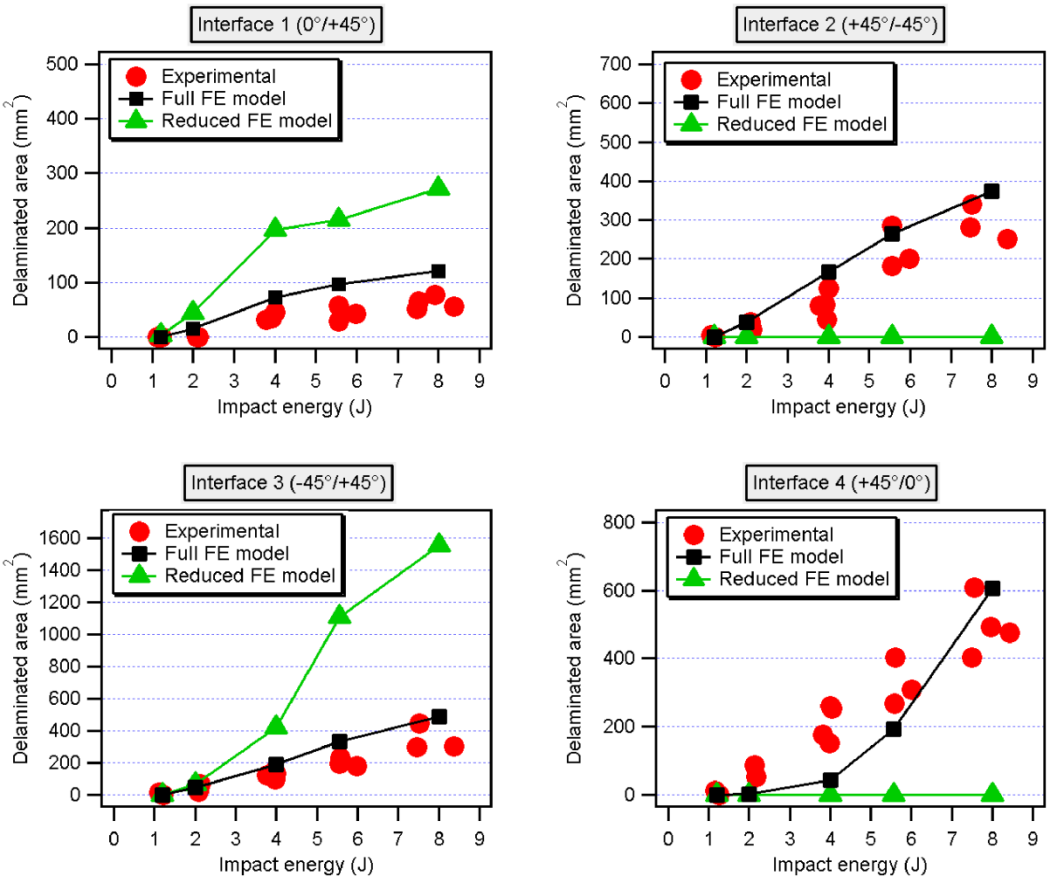

Figure 10-14: Comparison between experimental and predicted delamination areas at different interfaces.

10.3 Concluding Remarks

The developed failure models were applied to model the low-velocity impact response of multidirectional laminated plates over a wide range of impact energies.

Rather good agreement was observed between experiments and predictions in terms of structural response, extent and shape of the global projected damage area.

Additional numerical analyses were carried out to investigate the importance of modelling in-ply damage modes for accurate simulation of impact events. It was found that although the reduced FE model (where only interlaminar damage was included in the calculations) could predict with acceptable accuracy the structural impact response of the laminates, it was not capable of properly capturing the through-thickness distribution of delaminations, thus suggesting that implementation of in-ply damage modes, even if significantly increasing the computational complexity of the model, may be required for accurate prediction of impact damage pattern in multidirectional laminates.

CHAPTER 11

CONCLUSIONS

Sandwich composites, consisting of two thin fibre-reinforced laminate facesheets separated by a thick core material of low density, are being increasing used in aerospace, marine, automotive, wind energy and many other applications, because of their high bending stiffness, superior buckling resistance as well as good static and fatigue strength properties. As an example, composite sandwich configurations are nowadays commonly adopted in wing shells and internal stiffeners of modern wind turbine blades, and are under consideration for potential use in other primary structural elements of the blade, such as the load carrying flange of the main spar or the spar-caps of the wing shells.

One of the main limitations of sandwich composites is their relatively high susceptibility to damage caused by foreign object impact events, which can be reasonably expected during the whole life (including manufacturing, transport, installation and service) of most engineering structures. Typical impact damage occurring in sandwich composites involves the combination of different failure mechanisms, such as delaminations, matrix cracking, fibre fracture, face-core debonding and core crushing, which may be difficult to detect by simple visual inspection (BVID). Damage induced by impact, notably delaminations, may induce significant reductions in stiffness and strength of the composites and result in a local, or even global, collapse of the structure.

While the presence of damage has often been taken into account at the design stage by imposing large safety margins, more advanced damage tolerance concepts are being gradually introduced in the design process of critical load bearing sandwich structures so as to take full advantage of the weight-saving potentiality offered by sandwich materials. Design schemes based on a damage tolerance approach require a detailed knowledge of the nature and extent of damage induced by impact events for a safe estimation of residual strength and expected life of the damaged structure. There is thus a strong need for reliable numerical tools capable of providing reasonably accurate predictions of impact damage potentially developing during operation lifetime in primary sandwich structures.

Even though various impact test procedures and destructive or nondestructive inspection techniques are available to assess the impact damage resistance of sandwich composites, experimental testing is extremely time-consuming and cost-intensive, given the wide range of possible structural configurations and loading conditions to be characterized. While the complexity of physical phenomena involved in an impact event restricts the applicability of analytical models to the investigation of simple geometries and loading cases, numerical finite element (FE) tools based on appropriate fracture models may provide an efficient alternative, at least at a preliminary or intermediate design stage, to costly experimental tests for prediction of the impact response of composite sandwich structures.

The work of this thesis is to develop a reliable numerical tool to investigate the structural and damage response of foam-based sandwich composites.

A Finite Element (FE) tool implementing energy-based CDM models and cohesive interface elements was developed and implemented into ABAQUS/Explicit through user-defined subroutines VUMAT. The model accounts for the initiation and propagation of the typical damage modes occurring in the laminate skins (fibre fracture, matrix cracking and delaminations) by means of progressive failure models for intralaminar damage and interfacial cohesive laws for interlaminar damage, and describes the nonlinear behaviour of the foam core by a crushable foam plasticity model natively implemented in ABAQUS.

A series of impact tests was conducted on sandwich panels with various configurations using an instrumented drop-weight testing machine; impact-induced damage was assessed by penetrant-enhanced X-radiography for all specimens. In a limited number of selected samples, the through-thickness distribution of impact-inflicted delaminations was further assessed by stereoscopic X-radiography and validated by ultrasonic C-scans or optical microscopy of polished cross-sections.

Analyses of experimental findings show that structural and damage resistance to impact of sandwich composites is clearly affected by the density of the core material, while the thickness of the core has little influence, in the examined range.

Full 3D finite element models were constructed in ABAQUS/Explicit and applied to simulate low-velocity impacts on sandwich panels with either cross-ply laminate facesheets (stacking sequence: $[0/90_3/0]$) or multidirectional laminate skins (stacking sequence: $[0_3/+45/-45]_S$) bonded to a 10 mm PVC foam core with three different foam

densities: 65 kg/m^3 (HP60), 100 kg/m^3 (HP100) and 160 kg/m^3 (HP160). Numerical predictions were compared with experimental results in terms of both structural response and internal damage for impact energies ranging approximately from 1 J to 8 J.

Good agreement is obtained between numerical simulations and experiments, for sandwich panels with both cross-ply and multidirectional laminate skins, not only in terms of structural response (force histories, force-displacement curves and absorbed energies), but also in terms of internal damage (temporal sequence of major damage events; projected damage shapes, sizes and detailed through-thickness distributions). Both numerical results and experimental observations support the assumption that the stiffness reduction exhibited by the force-displacement curve at the knee load is mainly induced by localized cell buckling of the foam material, rather than by damage of the impacted composite skin.

The developed failure models were further applied to impact cases with different configurations: different foam core thickness, different in-plane panel size and boundary condition. It is proved that the failure models are applicable to a wide range and show reasonably good prediction accuracy.

The developed FE tool was finally applied to model the low-velocity impact response of composite laminates. Rather good agreement was again observed between experiments and predictions in terms of structural response, extent and shape of the global projected damage area.

Moreover, additional numerical analyses were conducted to investigate how the implementation of intralaminar damage mechanism in the model affects the whole

prediction accuracy of the model. It was found that although the reduced FE model (where only interlaminar damage was included in the calculations) could predict with acceptable accuracy the structural impact response of the laminate, it was not capable of properly capturing the through-thickness distribution of delaminations, thus suggesting that implementation of in-ply damage modes, even if significantly increasing the computational complexity of the model, may be required for accurate prediction of impact damage pattern.

PUBLICATIONS

D. Feng, F. Aymerich. *Damage prediction in composite sandwich panels subjected to low-velocity impact*. Composites Part A: Applied Science and Manufacturing. Vol. 52 (2013) pp. 12–22. (ISSN: 1359-835X)

Dianshi Feng, Francesco Aymerich. *Simulation of Impact Damage in Foam-based Sandwich Composites*. Key Engineering Materials Vols. 569-570 (2013) pp. 25-32. (ISSN: 1013-9826)

D. Feng, F. Aymerich. *Finite element modelling of damage induced by low-velocity impact on composite laminates*. Composite Structures. Vol.108 (2014) pp. 161–171. (ISSN: 0263-8223)

F. Aymerich, A. Cerioni, D. Feng. (2011) *Prediction of Impact Induced Delamination in Composite Plates Using Cohesive Elements: A Comparison of 3D Solid and Shell FE Models*. 32nd Risø International Symposium on Materials Science. Risø DTU, Denmark, pp. 213-220. (ISBN: 978-87-550-3925-4; ISSN: 0907-0079)

Dianshi Feng, Francesco Aymerich. (2012) *A FE model for prediction of impact-induced damage in composite sandwich structures*. EWEA2012 - European Wind Energy Association, Annual Event, Copenhagen, Denmark.

Dianshi Feng, Agostino Cerioni, Francesco Aymerich. (2012) *Simulation of impact damage in laminated composites by progressive damage models*. ECCM15 - 15th European Conference on Composite Materials, Venice, Italy. (ISBN: 978-88-88785-33-2)

J.T. Ruan, D. Feng, F. Aymerich, J.W. Tong, P.Priolo. (2012) *Application of CARRIER-ESPI for measurement of out of plane displacements in unstitched and stitched laminates subjected to compression-after-impact*. ECCM15 - 15th European Conference on Composite Materials, Venice, Italy. (ISBN: 978-88-88785-33-2)

D. Feng, A. Cerioni, F. Aymerich. (2014) *Structural response and damage resistance of sandwich composites subjected to low velocity impact*. ECCM16 - 16th European Conference on Composite Materials, Seville, Spain. Accepted.

BIBLIOGRAPHY

Abaqus 6.10 Analysis User's manual . vol. II: Analysis. RI: Dassault Systemes, 2010.

Abaqus 6.10 Analysis User's manual. Section 18.3.5: "CRUSHABLE FOAM PLASTICITY MODELS". RI: Dassault Systemes Simulia Corp., 2010.

Abrate, S. Impact on composite structures. Cambridge: Cambridge University Press, 1998.

Abrate, S. "Impact on Laminated Composite Materials." Applied Mechanics Reviews 4 (1991): 155-190.

Abrate, S. "Localized impact on sandwich structures with laminated facings." Applied Mechanics Reviews 50 (1997): 69-97.

Adams, D.F., and L.G. Adams. "A Tensile Impact Apparatus for Composite Materials." Experimental Mechanics 29, no. 4 (1989): 466-473.

Akil, H M, and W J Cantwell. "The low impact response of foam-based sandwich structures." Composites Part B 33 (2002): 192–204.

Alfano, G. "On the influence of the shape of the interface law on the application of cohesive-zone models." Compos Sci Technol 66 (2006): 723–730.

Allgaier, M.W, and S Ness. Volume 8: Visual and Optical Testing. Nondestructive Testing Handbook, Columbus, Ohio: American Society for Nondestructive Testing, 1993.

Allix, O, P Ladeveze, and A Corigliano. "Damage analysis of interlaminar fracture specimens." Composite Structures 31, no. 1 (1995): 61-74.

Amaro, A.M., J.B. Santos, and J.S. Cirne. "Delamination depth in composites laminates with interface elements and ultrasound analysis." Strain 47, no. 2 (2011): 138-145.

Aoki, Y, H Suemasu, and T Ishikawa. "Damage propagation in CFRP laminates subjected to low velocity impact and static indentation." Adv Compos Mater 16, no. 1 (2007): 45–61.

Ashby, M F. Materials Selection in Mechanical Design. Oxford, UK: Pergamon, 1992.

ASTM-D3039/D3039M-08. Standard test method for tensile properties of polymer matrix composite materials. West Conshohocken (PA): ASTM International, 2008.

ASTM-D3410/D3410M-03. Standard Test method for compressive properties of polymer matrix composite materials with unsupported gage section by shear loading. West Conshohocken (PA): ASTM International, 2008.

ASTM-D7136-07. Measuring the Damage Resistance of a Fiber-Reinforced Polymer Matrix Composite to a Drop-Weight Impact Event. W. Conshohocken, Pa.: ASTM International, 2007.

ASTM-D7137-07. Compressive Residual Strength Properties of Damaged Polymer Matrix Composite Plates. W. Conshohocken, Pa.: ASTM International, 2007.

Aymerich, F, and S Meili. "Ultrasonic evaluation of matrix damage in impacted composite laminates." Composites Part B: Engineering 31, no. 1 (2000): 1-6.

Aymerich, F, F Dore, and P Priolo. "Prediction of impact- induced delamination in cross -ply composite laminates using cohesive interface elements." Composites science and technology 68, no. 12 (2008): 2383- 2390.

Aymerich, F, F Dore, and P Priolo. "Simulation of multiple delaminations in impacted cross-ply laminates using a finite element model based on cohesive interface elements." Composites Science and Technology 69 (2009): 1699–1709.

Belingardi, G, M P Cavatorta, and R Duella. "Material characterization of a composite–foam sandwich for the front structure of a high speed train." Composite Structures 61 (2003): 13–25.

Berggreen, C, K Branner, J.F Jensen, and J.P Schultz. "Application and analysis of sandwich elements in the primary structure of large wind turbine blades." Journal of Sandwich Structures and Materials 9, no. 6 (2007): 525-552.

Berry, J.P. "Determination of fracture energies by the cleavage technique." J. Appl. Phys. 34 (1963): 62–68.

Besant, T, G A O Davies, and D Hitchings. "Finite element modelling of low velocity impact of composite sandwich panels." Composites part A 32 (2001): 1189-1196.

Bland, P.W, and S Michelle. "A discussion on the role played by velocity in impact mechanics." Proceedings of the 19th Conference of Mechanical Engineering Network of Thailand. Phuket, Thailand, 2005. 19–21.

Borg, R, L Nilsson, and K Simonsson. "Simulation of low velocity impact on fiber laminates using a cohesive zone based delamination model." Compos Sci Technol 64 (2004): 279–88.

Bouvet, C, B Castanié, M Bizeul, and J.J. Barrau. "Low velocity impact modelling in laminate composite panels with discrete interface elements." International Journal of Solids and Structures 46 (2009): 2809–2821.

Brøndsted, Povl, Hans Lilholt, and Aage Lystrup. "COMPOSITE MATERIALS FOR WIND POWER TURBINE BLADES." Annual Review of Materials Research 35 (2005): 505-538.

Brooks, R, K A Brown, N A Warrior, and P P Kulandaivel. "Predictive modeling of the impact response of thermoplastic composite sandwich structures." Journal of Sandwich Structures and Materials 12 (2010): 449-476.

Burton, T, N Jenkins, D Sharpe, and E Bossanyi. Wind Energy Handbook. 2nd Ed. John Wiley & Sons, Ltd, 2011.

Camanho, P P, and C G Dávila. "Mixed-Mode Decohesion Finite Elements for the Simulation of Delamination in Composite Materials." NASA/TM-2002-211737, 2002.

Camanho, P.P, C.G Davila, and M.F De Moura. "Numerical simulation of mixed-mode progressive delamination in composite materials." Journal of Composite Materials 37, no. 16 (2003): 1415–1438.

Cantwell, W.J., and J Morton. "The Impact Resistance of Composite Materials - A Review." Composites 22 (1991): 347-362.

Caprino, G, V Lopresto, M Riccio, and C Leone. "Effect of a Thin Soft Core on the Impact Behaviour of CFRP Laminates." Applied Composite Materials 19, no. 2 (2012): 127-139.

Carlsson, L A, D F Adams, and P P Byron. Experimental characterization of advanced composite materials. Boca Raton: CRC Press, 2003.

Carlsson, L.A, J.W Gillespie, and B.R Trethewey. "Mode II interlaminar fracture of graphite/epoxy and graphite/PEEK." J. Reinf. Plast. Compos. 5 (1986): 170–187.

Castanié, B, C Bouvet, Y Aminanda, J.J Barrau, and P. Thévenet. "Modelling of low-energy/low-velocity impact on Nomex honeycomb sandwich structures with metallic skins." International Journal of Impact Engineering 35, no. 7 (2008): 620-634.

Chai, G.B, and S Zhu. "A review of low-velocity impact on sandwich structures." Proceedings of the Institution of Mechanical Engineers, Part L: Journal of Materials Design and Applications, 2011: 207-230.

Challenger, K.D. "The damage tolerance of carbon fiber composites. A workshop summary." Composite Structures 6 (1986): 295-318.

Chang, F K, and K Y Chang. "A Progressive Damage Model for Laminated Composites Containing Stress Concentrations." Journal of Composite Materials 21, no. 9 (1987): 834-855.

Chester, R.J, and G Clark. "Modelling of impact damage features in graphite/epoxy laminates." In Damage detection in composite materials, by J.E Masters, 200–212. Philadelphia: American Society for Testing and Materials: ASTM STP 1128, 1992.

Choi, H.Y, and F.K Chang. "A model for predicting damage in graphite/expoxy laminated composites resulting from low-velocity point impact." Journal of Composite Materials 26, no. 14 (1992): 2134–2169.

Christensen, M, and J Deteresa. "Delamination failure investigation for out-of-plane loading in laminates." J Compos Mater 38 (2004): 2231–2238.

Cui, W, and M.R Wisnom. "A combined stress-based and fracture-mechanics-based model for predicting delamination in composites." Composites 24, no. 6 (1993): 467—474.

Cui, W, M.R Wisnom, and M.I Jones. "Effect of through thickness tensile and compressive stresses on delamination propagation fracture energy." J Compos Technol Res 16 (1994): 329–335.

Cvitkovich, M.K, and W.C Jackson. "Compressive Failure Mechanisms in Composite Sandwich Structures." Journal of American Helicopter Society 44, no. 4 (1999): 260-268.

Da´vila, C.G, P.P Camanho, and C.A Rose. "Failure criteria for FRP laminates." J. Compos. Mater 39 (2005): 323–345.

Daniel, I.M. "Impact Response and Damage Tolerance of Composite Sandwich Structures." In Dynamic Failure of Materials and Structures, by A Shukla, G Ravichandran and Y Rajapakse, 191-233. New York: Springer, 2010.

de Borst, R, J.J.C Remmers, and A Needleman. "Mesh-independent discrete numerical representations of cohesive-zone models." Engineering Fracture Mechanics 73, no. 2 (2006): 160-177.

De Moura, MFSF, and JPM Gonçalves. "Modelling the interaction between matrix cracking and delamination in carbon–epoxy laminates under low velocity impact." Composites Science and Technology 64, no. 7 (2004): 1021-1027.

Demuts, E. "Damage tolerance of composites." Proc. of the American Soc.for Composites, 4th Technical Conf. Blacksburg, VA: Virginia Polytechnic Institute and State University, 1990. 425-433.

Deshpande, V.S., and N.A. Fleck. "Isotropic constitutive models for metallic foams." Journal of the Mechanics and Physics of Solids 48 (2000): 1253-1283.

Deteresa, J, C Freeman, and E Groves. "The effects of through-thickness compression on the interlaminar shear response of laminated fiber composites." J Compos Mater 38 (2004): 681–697.

DIAB. Technical manual. Divinycell HP, 2006.

DNV. Design And Manufacture of Wind Turbine Blades - Offshore And Onshore Wind Turbines. DNV-OS-J102, 2006.

DNV. Guidelines for Design of Wind Turbine. 2nd edition. Det Norske Veritas and Risø National Laboratory, 2002.

Donadon, M V, L Iannucci, BG Falzon, JM Hodgkinson, and SFM de Almeida. "A progressive failure model for composite laminates subjected to low velocity impact damage." Computers and Structures 86 (2008): 1232-1252.

Drzal, LT, MJ Rich, and PF Lloyd. "Adhesion of graphite fibers to epoxy matrices: I. the role of fiber surface treatment." The Journal of Adhesion 16, no. 1 (1983): 1-30.

Elder, D.J., R.S. Thomson, M.W. Nguyen, and M.L. Scott. "Review of delamination predictive methods for low speed impact of composite laminates." Composite structures 66 (2004): 677- 683.

EWEA. Green growth: The impact of wind energy on jobs and the economy. 2012.

Faggiani, A, and BG Falzon. "Predicting low-velocity impact damage on a stiffened composite panel." Composites: Part A 41 (2010): 737–749.

Falzon, BG, and P Apruzzese. "Numerical analysis of intralaminar failure mechanisms in composite structures. Part I: FE implementation." Composite Structures 93 (2011): 1039–1046.

Falzon, BG, and P Apruzzese. "Numerical analysis of intralaminar failure mechanisms in composite structures. Part II: Applications." Composite Structures 93 (2011): 1047–1053.

Feng, D, and F Aymerich. "Damage prediction in composite sandwich panels subjected to low velocity impact." Composites: Part A 52 (2013): 12–22.

Feng, D, and F Aymerich. "Finite element modelling of damage induced by low-velocity impact on composite laminates." Composite Structures 104 (2014): 161–171.

Feng, D, and F Aymerich. "Simulation of Impact Damage in Foam-based Sandwich Composites." Key Engieering Materials 569-570 (2013): 25-32.

Feraboli, P. "Some recommendations for characterization of composite panels by means of drop tower impact testing." Journal of aircraft 43, no. 6 (2006): 1710-1718.

Foo, CC, GB Chai, and LK Seah. "A model to predict low-velocity impact response and damage in sandwich composites." Composites Science and Technology 68 (2008): 1348–1356.

Garnich, M R, and V M K Akula. "Review of degradation models for progressive failure analysis of fiber reinforced polymer composites." Applied Mechanics Reviews 62 (2009): 1-33.

Gibson, L J, and M F Ashby. Cellular solids: structure and properties. Cambridge: Cambridge University Press, 1999.

González, EV, P Maimí, PP Camanho, A Turon, and JA Mayugo. "Simulation of drop-weight impact and compression after impact tests on composite laminates." Composite Structures 94, no. 11 (2012): 3364-3378.

Hart-Smith, L.J. "Predictions of the original and truncated maximumstrain failure models for certain fibrous composite laminates." Compos Sci Technol 58 (1998): 1151.

Hart-Smith, L.J. "Should fibrous composite failure modes be interacted or superimposed?" Composites 24 (1993): 53–55.

Hayman, B. "Approaches to Damage Assessment and Damage Tolerance for FRP Sandwich Structures." Journal of Sandwich Structures and Materials 9, no. 6 (2007): 571-596.

Hayman, B, J Wedel-Heinen, and P Brøndsted. "Materials Challenges in Present and Future Wind Energy." MRS Bulletin 33 (2008): 343-353.

Hinton, M.J, S.K Kaddour, and P.D Soden. "A comparison of the predictive capabilities of current failure theories for composite laminates, judged against experimental evidence." Compos Sci Technol 62 (2002): 1725–1797.

Hirai, Y, H Hamada, and J.K Kim. "Impact response of glass woven fabric laminates. Pt I: effect of silane coupling agents." Composites Science and Technology 58 (1998): 91–104.

Hou, J.P, N Petrinic, and C Ruiz. "A delamination criterion for laminated composites under low-velocity impact." Composites Science and Technology 61 (2001): 2069-2074.

Iannucci, L. "Progressive failure modelling of woven carbon composite under impact." International Journal of Impact Engineering 32, no. 6 (2006): 1013–43.

Iannucci, L, and ML Willows. "An energy based damage mechanics approach to modeling impact onto woven composite materials-Part I: Numerical models." Composites part A 37 (2006): 2041–2056.

Iannucci, L, and ML Willows. "An energy based damage mechanics approach to modelling impact onto woven composite materials: Part II. Experimental and numerical

results." Composites Part A: Applied Science and Manufacturing 38, no. 2 (2007): 540-554.

Iannucci, L, R Dechaene, M Willows, and J Degrieck. "A failure model for the analysis of thin woven glass composite structures under impact loadings." Computers and Structures 79, no. 8 (2001): 785–99.

Icardi, U, and L Ferrero. "Impact analysis of sandwich composites based on a refined plate element with strain energy updating." Composite Structures 89 (2009): 35–51.

IEA, International Energy Agency. Technology Roadmap - Wind energy. 2013. www.iea.org.

Ivanez, I, C Santiuste, and S Sanchez-Saez. "FEM analysis of dynamic flexural behaviour of composite sandwich beams with foam core." Composite Structures 92, no. 9 (2010): 2285–91.

Jang, Bor Z. Advanced polymer composites: Principles and Applications. OH,USA: ASM International, 1994.

Johnson, A F. "Modelling fabric reinforced composites under impact loads." Composites 32 (2001): 1197–1206.

Joshi, S.P., and C.T. Sun. "Impact-Induced Fracture Initiation and Detailed Dynamic Stress Field in the Vicinity of the Impact." American Society for Composites Second Technical Conference, 1987: 177-185.

Kachanov, LM. Introduction to continuum damage mechanics. Boston: Martinus Nijhoff Publsihers, 1987.

Kaw, A K. Mechanics of composite materials. Boca Raton, Fla.: CRC Press, 2006.

Kim, J.K. "Recent developments in impact damage assessment of fibre composites." In Impact behaviour of fibre-reinforced composite materials and structures, by S.R. Reid and G Zhou, 33-74. Boca Raton FL: Woodhead Publishing Ltd and CRC Press LLC, 2000.

Kim, JS, SJ Lee, and KB Shin. "Manufacturing and structural safety evaluation of a composite train carbody." Composite Structures 78 (2007): 468–476.

Klaus, M, H G Reimerdes, and N K Gupta. "Experimental and numerical investigations of residual strength after impact of sandwich panels." International Journal of Impact Engineering 44 (2012): 50-58.

Leijten, J, HEN Bersee, OK Bergsma, and A Beukers. "Experimental study of the low-velocity impact behaviour of primary sandwich structures in aircraft." Composites Part A 40 (2009): 164–175.

Lemaitre, J, and JL Chaboche. Mechanics of solid materials. Cambridge: Cambridge University Press, 1990.

Li, S, M.D Thouless, A.M Waas, J.A Schroeder, and P.D Zavattieri. "Mixed mode cohesive zone models for fracture of an adhesively bonded polymer-matrix composite." Eng Fract Mech 73 (2006): 64–78.

Li, X, S.R Hallett, and M.R Wisnom. "Predicting the effect of through-thickness compressive stress on delamination using interface elements." Composites: Part A 39 (2008): 218–230.

Liu, D, and L.E. Malvern. "Matrix Cracking in Impacted Glass/Epoxy Plates." Journal of Composite Materials 7 (1987): 594-609.

Lopes, CS, PP Camanho, Z Gürdal, P Maimi, and EV González. "Low-velocity impact damage on dispersed stacking sequence laminates. Part II: Numerical simulations." Composites Science and Technology 69 (2009): 937–947.

Lovatt, A, and H Shercliff. Material selection and processing. 2002.

Maimí, P, JA Mayugo, and PP Camanho. "A Three-dimensional damage model for transversely isotropic composite laminates." Journal of Composite Materials 42, no. 25 (2008): 2717-2745.

Maimí, P, PP Camanho, JA Mayugo, and CG Dávila. "A continuum damage model for composite laminates: Part I – Constitutive model." Mechanics of Materials 39 (2007): 897–908.

Meo, M, R Vignjevic, and G Marengo. "The response of honeycombsandwich panels under low-velocity impact loading." International Journal of Mechanical Sciences 47 (2005): 1301–1325.

Mi, Y, M.A Crisfield, G.A.O Davies, and H.B Hellweg. "Progressive delamination using interface elements." Journal of Composite Materials 32, no. 14 (1998): 1246–1272.

MIL-HDBK-17-3E. Polymer matrix composites. Materials usage, design and analysis. Department of defense handbook. Vol. 3. Department of Defense of United States of America, 1997.

Mines, RAW, CM Worrall, and AG Gibson. "Low velocity perforation behaviour of polymer composite sandwich panels." International Journal of Impact Engineering 21 (1998): 855–79.

Nguyen, M Q, S S Jacombs, and R S Thomson. "Simulation of impact on sandwich structures." Composite Structures 67, no. 2 (2005): 217–227.

Olsson, R. "Mass criterion for wave controlled impact response of composite plates." Composites, Part A 31 (2000): 879–887.

Orifici, A.C, I Herszberg, and R.S Thomson. "Review of methodologies for composite material modelling incorporating failure." Compos Struct 86 (2008): 194–210.

Ortiz, M, and A Pandol. "Finite-deformation irreversible cohesive elements for three-dimensional crack-propagation analysis." International Journal for Numerical Methods in Engineering 44 (1999): 1267-1282.

Palazotto, A, GE Maddux, and B Horban. "The use of stereo X-ray and deply techniques for evaluating instability of composite cylindrical panels with delaminations." Experimental Mechanics 29, no. 2 (1989): 144-151.

Philipp, S.L, F Afsar, and A Gudmundsson. "Effects of mechanical layering on hydrofracture emplacement and fluid transport in reservoirs." Frontiers in Earth Science, December 2013.

Pinho, S T, L Iannucci, and P Robinson. "Physically based failure models and criteria for laminated fibre-reinforced composites with emphasis on fibre kinking. Part II: FE implementation." Composites: Part A 37 (2006): 766–777.

Pinho, ST, CG Davila, PP Camanho, L Iannucci, and P Robinson. "Failure models and criteria for FRP under in-plane or three-dimensional stress states including shear non-linearity." NASA/TM-2005-213530, 2005.

Puck, A, and H Schürmann. "Failure analysis of FRP laminates by means of physically based phenomenological models." Composites Science and Technology 62 (2002): 1633–1662.

Puck, A, and H Schürmann. "FAILURE ANALYSIS OF FRP LAMINATES BY MEANS OF PHYSICALLY BASED PHENOMENOLOGICAL MODELS." Composites Science and Technology 58 (1998): 1045-1067.

RDS01001. "Data Sheet of Advanced Matrix Prepreg TEXIPREG ET223." 2004.

RIAC. "Blueprints for Product Reliability Part 5 - Measuring Product Reliability." RIAC (Reliability Information Analysis Center) Desk Reference. www.theriac.org/DeskReference/viewDocument.php?id=284&Scope=blueprints&Deskref=blueprint5.

Richardson, M.O.W., and M.J. Wisheart. "Review of low-velocity impact properties of composite materials." Composites Part A 27A (1996): 1123-1131.

Robinson, P, and GAO Davies. "Impactor mass and specimen geometry effects in low velocity impact of laminated composites." Int J Impact Eng 12, no. 2 (1992): 189–207.

Romary, Juillet. Ultrasonic unspection principle of a material. July 2006. http://en.wikipedia.org/wiki/File:UT_principe.svg.

Rosen, B W. Fibre Composite Materials. Metals Park, OH, USA: ASM, 1965.

Rotem, A. "Prediction of laminate failure with the Rotem failure criterion." Compos Sci Technol 58 (1998): 1083.

Schoeppner, G.A, and S Abrate. "Delamination threshold loads for low velocity impact on composite laminates." Composites Part A: applied science and manufacturing 9 (2000): 903-915.

Schubel, P M, J J Luo, and I M Daniel. "Low velocity impact behavior of composite sandwich panels." Composites Part A 36 (2005): 1389–1396.

Sethi, S, and BC Ray. "Evaluation of structural integrity and mechanical behavior of advanced FRP composites." International Journal of Structural Integrity 2, no. 2 (2011): 214-222.

Shet, C, and N Chandra. "Analysis of energy balance when using cohesive zone models to simulate fracture processes." J Eng Mater Technol 124 (2002): 440–450.

Shi, Y, T Swait, and C Soutis. "Modelling damage evolution in composite laminates subjected to low velocity impact." Composite Structures 94, no. 9 (2012): 2902-2913.

Shivakumar, K.N., W. Elber, and M Illg. "Prediction of Low-Velocity Impact Damage in Thin Circular Composite Laminates." AIAA Journal 23, no. 3 (1985): 442-449.

Sierakowski, R.L. "Impact damage-tolerant composite structural design." In Impact Behavior of Fiber-Reinforced Composite Materials and Structures, by SR Reid and G Zhou, 106-132. Cambridge, England: Woodhead Publishing Limited, 2000.

Sjöblom, P.O., J.T. Hartness, and T.M. Cordell. "On low-velocity impact testing of composite materials." Journal of Composite Materials 22 (1988): 30-52.

Soden, P.D, M.J Hinton, and A.S Kaddour. "A comparison of the predictive capabilities of current failure theories for composite laminates." Compos. Sci. Technol 58, no. 7 (1998): 1225-1254.

Srinivasan, K, W.C Jackson, B.T Smith, and J.A Hinkley. "Characterization of damage modes in impacted thermoset and thermoplastic composites." Journal of Reinforced Thermoplastic and Composites 11 (1992): 1111-1126.

Steeves, CA, and NA Fleck. "Collapse mechanism of sandwich beams with composite faces and a foam core, loaded in three-point bending. Part II: experimental investigation and numerical modeling." International Journal of Mechanical Science 46 (2004): 585–608.

Stronge, W.J. Impact mechanics. Cambridge: Cambridge University Press, 2000.

Sun, C.T, and J.X Tao. "Prediction of failure envelopes and stress/strain behaviour of composite laminates." Compos Sci Technol 58 (1998): 1125.

Swain, R E, K L Reifsnider, K Jayaraman, and M Elzein. "Interface/Interphase Concepts in Composite Material Systems." J. Thermoplastic Compos. Mater. 3, no. 1 (1990): 13-23.

Tay, T.E., G Liu, V.B.C Tan, X.S. Sun, and D.C. Pham. "Progressive failure analysis of composites." Journal of Composite Materials 42, no. 18 (2008): 1921-1964.

Tay, TE. "Characterization and analysis of delamination fracture in composites: an overview of developments from 1990 to 2001." Applied Mechanics Reviews 56, no. 1 (2003): 1-32.

Thomsen, O T. "Sandwich Materials for Wind Turbine Blades - Present and Future." Journal of Sandwich Structures and Materials 11 (2009): 7-26.

Turon, A, C.G. Davila, P.P. Camanho, and J. Costa. "An engineering solution for mesh size effects in the simulation of delamination using cohesive zone models." Engineering Fracture Mechanics 74, no. 10 (2007): 1665–1682.

UpWind. Design Limits and Solutions for Very Large Wind Turbines. Brussels: EWEA, 2011.

Williams, J.G, and H Hadavinia. "Analytical solutions for cohesive zone models." J Mech Phys Solids 50, no. 4 (2002): 809–825.

Wisnom, M.R. "Modelling discrete failures in composites with interface elements." Composites Part A: Applied Science and Manufacturing 41, no. 7 (2010): 795-805.

www.luxresearchinc.com. 2011.

Zenkert, D, A Shipsha, P Bull, and B Hayman. "Damage tolerance assessment of composite sandwich panels with localised damage." Composites Science and Technology 65, no. 15 (2005): 2597-2611.

Zhang, Y, P Zhu, and X Lai. "Finite element analysis of low-velocity impact damage in composite laminated plates." Materials & Design 27, no. 6 (2006): 513-519.

Zhou, D.W, and W.J Stronge. "Low velocity impact denting of HSSA lightweight sandwich panel." International Journal of Mechanical Sciences 48 (2006): 1031–1045.

Zhou, J, M.Z. Hassan, Z Guan, and W.J. Cantwell. "The low velocity impact response of foam-based sandwich panels." Composites Science and Technology 72 (2012): 1781–1790.